PB2002-101928

NUMERICAL MODELING OF GEOSYNTHETIC REINFORCED FLEXIBLE PAVEMENTS

FHWA/MT-01-003/99160-2

Final Report

prepared for
THE STATE OF MONTANA
DEPARTMENT OF TRANSPORTATION

in cooperation with
THE U.S. DEPARTMENT OF TRANSPORTATION
FEDERAL HIGHWAY ADMINISTRATION
and the
Idaho, Kansas, Minnesota, New York, Texas, Wisconsin
and Wyoming Departments of Transportation and the
Western Transportation Institute at Montana State University

November 2001

prepared by
Dr. Steven W. Perkins
Montana State University

RESEARCH PROGRAM

REPRODUCED BY: NTIS
U.S. Department of Commerce
National Technical Information Service
Springfield, Virginia 22161

NUMERICAL MODELING OF GEOSYNTHETIC REINFORCED FLEXIBLE PAVEMENTS

FHWA/MT–01–003/99160–2

Final Report

Prepared for the
STATE OF MONTANA
DEPARTMENT OF TRANSPORTATION
RESEARCH, DEVELOPMENT AND TECHNOLOGY TRANSFER PROGRAM
in cooperation with the
U.S. DEPARTMENT OF TRANSPORTATION
FEDERAL HIGHWAY ADMINISTRATION
and the
Idaho, Kansas, Minnesota, New York, Texas, Wisconsin and Wyoming
Departments of Transportation
and the
Western Transportation Institute at Montana State University

October 1, 2001

Prepared by

Dr. Steven W. Perkins
Associate Professor
Department of Civil Engineering
Western Transportation Institute
Montana State University – Bozeman
Bozeman, Montana 59717
Office Telephone: 406-994-6119
Fax: 406-994-6105
E-Mail: stevep@ce.montana.edu

TECHNICAL REPORT STANDARD PAGE

1. Report No. **FHWA/MT–01–003/99160–2**	2. Government Accession No.	3. Recipient's Catalog No.
4. Title and Subtitle **Numerical Modeling of Geosynthetic Reinforced Flexible Pavements**	5. Report Date **October 1, 2001** 6. Performing Organization Code **MSU G&C #428573**	
7. Author **Steven W. Perkins, Ph.D., P.E.**	8. Performing Organization Report No.	
9. Performing Organization Name and Address **Department of Civil Engineering** **205 Cobleigh Hall** **Montana State University** **Bozeman, Montana 59717**	10. Work Unit No. 11. Contract or Grant No. **99160**	
12. Sponsoring Agency Name and Address **Montana Department of Transportation** **Research Section** **2701 Prospect Avenue** **P.O. Box 201001** **Helena, Montana 59620-1001**	13. Type of Report and Period Covered **Final: October 1, 1998 – October 1, 2001** 14. Sponsoring Agency Code **5401**	

15. Supplementary Notes
Preparation in cooperation with the U.S. Department of Transportation, Federal Highway Administration

16. Abstract

Experimental studies conducted over the course of the past 20 years have demonstrated both general and specific benefits of using geosynthetics as reinforcement materials in flexible pavements. Existing design solutions are largely empirically based and appear to be unable to account for many of the variables that influence the benefit derived from the reinforcement. Advanced numerical modeling techniques present an opportunity for providing insight into the mechanics of these systems and can assist with the formulation of simplified numerical methods that incorporate essential features needed to predict the behavior of these systems.

Previous experimental work involving the construction of geosynthetic reinforced test sections has shown several difficulties and uncertainties associated with the definition of reinforcement benefit for a single cycle of load application. Even though many reinforcement mechanisms are apparent and often times striking during the application of the first load cycle, the distinction between reinforced test sections is not nearly so clear as that which is seen when examining long term performance, where long term performance is defined in terms of permanent surface deformation after many load cycles have been applied.

This indicates the need for an advanced numerical model that is capable of describing the repeated load behavior of reinforced pavements. In particular, models for the various pavement layers are needed to allow for a description of the accumulation of permanent strain under repeated loads. To meet these needs, a finite element model of unreinforced and geosynthetic reinforced pavements was created. The material model for the asphalt concrete layer consisted of an elastic-perfectly plastic model where material property direction dependency could be added. This model allowed for the asphalt concrete layer to deform with the underlying base aggregate and subgrade layers as repeated pavement loads were applied.

A bounding surface plasticity model was used for the base aggregate and subgrade layers. The model is well suited for the prediction of accumulated permanent strains under repeated loading and is most suitable for fine-grained materials. A material model containing components of elasticity, plasticity, creep and direction dependency was formulated for the geosynthetic and calibrated against a series of in-air tension tests. A Coulomb friction model was used to describe shear interaction between the base aggregate and the geosynthetic. The model is essentially an elastic-perfectly plastic model, allowing for specification of the shear interface stiffness and ultimate strength. This model was calibrated from a series of pull out tests.

Finite element models were created to match the conditions in pavement test sections reported by Perkins (1999a). Membrane elements were used for the geosynthetic and a contact interface was used between the geosynthetic and the base course aggregate. Models of unreinforced and reinforced pavement sections were created and compared to test section results.

The results showed the model's ability to describe an accumulation of permanent strain and deformation in the system. The models were also capable of qualitatively showing mechanisms of reinforcement observed from pavement test sections. Exact predictions of pavement system response were difficult to achieve because of several deficiencies in the material models used and because of the run times needed for the models. The overriding model deficiency appears to be related to the model for the base course aggregate, which did not appear to be sufficiently sensitive to effects of restraint of the lateral motion of the material. The observation of certain reinforcement effects on response measures from the pavement system, such as vertical strain in the top of the subgrade and mean stress in the base

course layer, indicate the model's suitability for use within the context of a mechanistic-empirical modeling approach. This approach requires that the model be used for one load cycle application with certain stress and strain response measures being used outside the model within empirical damage models to predict long-term pavement performance. This approach is taken in a companion report for this project (Perkins, 2001) whose focus is on the development of a design model for this application.

17. Key Words	18. Distribution Statement
Pavements, Highways, Geogrid, Geotextile, Geosynthetic, Reinforcement, Base Course, Finite Element Model, Numerical Modeling	**Unrestricted. This document is available through the National Technical Information Service, Springfield, VA 21161.**

19. Security Classif. (of this report)	20. Security Classif. (of this page)	21. No. of Pages	22. Price
Unclassified	**Unclassified**	**97**	

PREFACE

DISCLAIMER

The opinions, findings and conclusions expressed in this publication are those of the authors and not necessarily those of the Montana Department of Transportation or the Federal Highway Administration

ALTERNATE FORMAT STATEMENT

MDT attempts to provide reasonable accommodations for any known disability that may interfere with a person participating in any service, program or activity of the department. Alternative accessible formats of this document will be provided upon request. For further information, call (406) 444-7693 or TTY (406) 444-7696.

NOTICE

The authors, the State of Montana, and the Federal Highway Administration do not endorse products or manufacturers. Trade and manufacturers names appear herein solely because they are considered essential to the object of the report.

PROTECTED UNDER INTERNATIONAL COPYRIGHT
ALL RIGHTS RESERVED
NATIONAL TECHNICAL INFORMATION SERVICE
U.S. DEPARTMENT OF COMMERCE

Reproduced from
best available copy.

ACKNOWLEDGMENTS

The author gratefully recognizes the generous financial and technical support of the Montana, Idaho, Kansas, Minnesota, New York, Texas, Wisconsin and Wyoming Departments of Transportation and the Western Transportation Institute at Montana State University. The technical contribution of Mr. Yan Wang and Dr. Mike Edens is gratefully recognized. The Amoco Fabrics and Fibers Company and Tensar Earth Technologies, Incorporated graciously donated geosynthetic materials for preceding projects leading up to this work. Dr. Muralee Muraleetharan of the University of Oklahoma and Dr. Kim Mish of Lawrence Livermore National Laboratory generously provided source code and support for development of a user defined material model.

TABLE OF CONTENTS

LIST OF TABLES viii
LIST OF FIGURES ix
CONVERSION FACTORS xii
EXECUTIVE SUMMARY xiii
1.0 INTRODUCTION 1
2.0 LITERATURE REVIEW 2
2.1 Numerical Modeling of Flexible Pavements 2
2.2 Numerical Modeling of Geosynthetic Reinforced Pavements 5
2.3 Tension Testing and Material Modeling of Geosynthetics 10
2.4 Soil-Geosynthetic Interface Interaction Testing and Modeling 12
3.0 PRIOR TEST SECTION WORK 13
3.1 Test Sections Constructed 14
3.1.1 Test Box and Loading Apparatus 15
3.1.2 Pavement Layer Materials 16
3.1.3 Instrumentation 19
3.1.4 As-Constructed Pavement Layer Properties 20
3.2 Summary of Results 22
4.0 PAVEMENT LAYER MATERIAL MODELS AND CALIBRATION TESTS 26
4.1 Asphalt Concrete 26
4.2 Base Aggregate and Subgrade 29
4.3 Geosynthetics 33
4.3.1 Uniaxial Tension Tests 34
4.3.1.1 Fast Monotonic Tension 36
4.3.1.2 Creep Tension 36
4.3.1.3 Slow Monotonic Tension 37
4.3.1.4 Cyclic Tension: Series I 37
4.3.1.5 Cyclic Tension: Series II 37
4.3.2 Constitutive Model Formulation 37
4.3.2.1 Elasticity 39
4.3.2.2 Plasticity 40
4.3.2.3 Creep 42
4.3.3 Results 43
4.3.3.1 Fast Monotonic Tension 43
4.3.3.2 Creep Tension 45
4.3.3.3 Slow Monotonic Tension 45
4.3.3.4 Cyclic Tension: Series I 48
4.3.3.5 Cyclic Tension: Series II 48
4.4 Soil-Geosynthetic Interaction 50
4.4.1 Pull Out Tests 51
4.4.2 Determination of Interaction Parameters via Simplified Numerical Solution 53
4.4.3 Geosynthetic/Aggregate Interaction Model (GAIM) 55
4.4.4 Calibration of GAIM Via Finite Element Model Simulation of Pull Out Tests 57

5.0 PAVEMENT TEST FACILITY FINITE ELEMENT MODEL 68
5.1 Unreinforced FE Model 68
5.2 Perfect Reinforced FE Model 70
5.3 Reinforced FE Model 70
6.0 FINITE ELEMENT MODELING RESULTS 71
6.1 Unreinforced Pavements 71
6.2 Reinforced Pavements 78
7.0 CONCLUSIONS 87
8.0 REFERENCES 89
APPENDIX A: NOTATION 94

LIST OF TABLES

Table 2.2.1	Summary of finite element studies of geosynthetic reinforced pavements.	6
Table 3.1.1	Comparison test section variables.	14
Table 3.1.2	Geosynthetic material index properties.	18
Table 3.1.3	As-constructed asphalt concrete properties.	21
Table 3.1.4	As-constructed base course properties.	21
Table 3.1.5	As-constructed subgrade properties.	22
Table 3.1.6	Test section loading conditions.	22
Table 4.1.1	Indirect tension resilient modulus test results.	28
Table 4.2.1	Listing of bounding surface model material constants.	32
Table 4.2.2	Material model parameters for base aggregate and subgrade soils.	33
Table 4.3.1	Orthotropic elastic material properties.	40
Table 4.3.2	Anisotropic yield stress ratios.	42
Table 4.3.3	Creep material properties.	42
Table 4.3.4	Anisotropic creep ratios.	43
Table 4.4.1	GAIM material parameters.	60
Table 6.1.1	Material parameter values used for the AC of unreinforced test sections.	71

LIST OF FIGURES

Figure 2.1.1	Cyclic behavior of unbound aggregate a) conventional plasticity models, b) idealized actual behavior and kinematic hardening models.	4
Figure 2.3.1	Illustration of a) elastic-plastic, b) thermo-visco, c) anisotropic and d) ratcheting stress-strain behavior.	10
Figure 3.1.1	Schematic diagram of the pavement test facility.	15
Figure 3.1.2	Input load pulse and corresponding load cell measurement.	16
Figure 3.1.3	Grain size distribution of hot-mix aggregate, base course aggregate and silty sand subgrade.	17
Figure 3.1.4	CBR versus compaction moisture content for the clay subgrade.	19
Figure 3.2.1	Permanent surface deformation versus load cycle (CS2, 5, 6, 7, 8, 11).	23
Figure 3.2.2	Permanent surface deformation versus load cycle (CS9, 10).	24
Figure 3.2.3	Permanent surface deformation versus load cycle (SSS1, 2, 3, 4).	24
Figure 3.2.4	TBR for sections CS5, 6, 7 and 11 relative to section CS2.	25
Figure 3.2.5	TBR for section CS10 relative to section CS9.	25
Figure 4.2.1	Schematic illustration of the bounding surface plasticity model.	30
Figure 4.3.1	Schematic of uniaxial tension specimen configuration.	35
Figure 4.3.2	Boundary conditions for membrane element used in FE analysis.	38
Figure 4.3.3	Tabular data for isotropic hardening rule for the geosynthetics.	41
Figure 4.3.4	Experiment and prediction for fast monotonic uniaxial tension for the geogrid in the a) machine, b) cross-machine and c) 45° directions.	44
Figure 4.3.5	Experiment and prediction for fast monotonic uniaxial tension for the geotextile in the a) machine and b) cross-machine directions.	45
Figure 4.3.6	Experiment and prediction for creep uniaxial tension for the geogrid in the a) machine, b) cross-machine directions and c) 45° directions.	46
Figure 4.3.7	Experiment and prediction for creep uniaxial tension for the geotextile in the a) machine and b) cross-machine directions.	47
Figure 4.3.8	Experiment and prediction for slow monotonic uniaxial tension for the geogrid in the a) machine and b) cross-machine directions.	47
Figure 4.3.9	Experiment and prediction for slow monotonic uniaxial tension for the geotextile in the a) machine and b) cross-machine directions.	48
Figure 4.3.10	Experiment and prediction for series I cyclic uniaxial tension for the geogrid in the a) machine and b) cross-machine directions.	49
Figure 4.3.11	Experiment and prediction for series I cyclic uniaxial tension for the geotextile in the a) machine and b) cross-machine directions.	49
Figure 4.3.12	Experiment and prediction for series II cyclic uniaxial tension for the geogrid in the a) machine and b) cross-machine directions.	50
Figure 4.3.13	Experiment and prediction for series II cyclic uniaxial tension for the geotextile in the a) machine and b) cross-machine directions.	50
Figure 4.4.1	Schematic drawing of the pull out apparatus.	51
Figure 4.4.2	Sleeves used to form the gap interface at the front of the pull out apparatus.	52
Figure 4.4.3	Plan view of in-soil specimen arrangement.	53
Figure 4.4.4	Shear stress vs shear displacement relationship for the simplified numerical solution of interaction in the pull out test, a) 5 kPa, b) 15 kPa, c) 35 kPa.	55
Figure 4.4.5	Experimental and predicted pull out load-displacement curves for	

a) geogrid A and b) geotextile A. 56
Figure 4.4.6 Geosynthetic/aggregate interaction model. 57
Figure 4.4.7 Finite element model of pull out box. 59
Figure 4.4.8 FEM and pull out test results for Geogrid A, MD, σ = 35 kPa. 61
Figure 4.4.9 FEM and pull out test results for Geogrid A, XMD, σ = 35 kPa. 61
Figure 4.4.10 FEM and pull out test results for Geogrid A, MD, σ = 15 kPa. 62
Figure 4.4.11 FEM and pull out test results for Geogrid A, XMD, σ = 15 kPa. 62
Figure 4.4.12 FEM and pull out test results for Geogrid A, MD, σ = 5 kPa. 63
Figure 4.4.13 FEM and pull out test results for Geogrid A, XMD, σ = 5 kPa. 63
Figure 4.4.14 FEM and pull out test results for Geotextile, MD, σ = 35 kPa. 64
Figure 4.4.15 FEM and pull out test results for Geotextile, XMD, σ = 35 kPa. 64
Figure 4.4.16 FEM and pull out test results for Geotextile, MD, σ = 15 kPa. 65
Figure 4.4.17 FEM and pull out test results for Geotextile, XMD, σ = 15 kPa. 65
Figure 4.4.18 FEM and pull out test results for Geotextile, MD, σ = 5 kPa. 66
Figure 4.4.19 FEM and pull out test results for Geotextile, XMD, σ = 5 kPa. 66
Figure 4.4.20 FEM and pull out test displacement results at various load levels for Geotextile, MD, σ = 35 kPa. 67
Figure 5.1.1 Finite element model of unreinforced pavement test sections. 69
Figure 6.1.1 Permanent surface deformation from FEM and experiments for unreinforced SSS test sections. 72
Figure 6.1.2 Permanent surface deformation from FEM and experiments for unreinforced CS test sections. 72
Figure 6.1.3 Dynamic vertical stress versus depth along the load plate centerline for test section SSS1. 73
Figure 6.1.4 Dynamic vertical stress versus depth along the load plate centerline for test section CS2. 73
Figure 6.1.5 Permanent vertical strain versus radius in the bottom of the base (z = 160 mm) for test section SSS1. 74
Figure 6.1.6 Permanent vertical strain versus radius in the top of the subgrade (z = 350 mm) for test section SSS1. 74
Figure 6.1.7 Permanent vertical strain versus depth along the load plate centerline for test section CS2. 75
Figure 6.1.8 Permanent horizontal strain in the bottom of the base (z = 215 mm) versus radius for test section SSS1. 75
Figure 6.1.9 Permanent horizontal strain in the top of the subgrade (z = 310 mm) versus radius for test section SSS1. 76
Figure 6.1.10 Permanent horizontal strain in the bottom of the base (z = 325 mm) versus radius for test section CS2. 76
Figure 6.1.11 Permanent horizontal strain in the top of the subgrade (z = 415 mm) versus radius for test section CS2. 77
Figure 6.1.12 Dynamic vertical stress versus depth along the load plate centerline for test section CS2 using a revised model. 78

Figure 6.2.1 Lateral permanent strain in the bottom of the base versus lateral distance after 10 cycles of load. 80

Figure 6.2.2 Lateral permanent strain along the load plate centerline versus depth after 10 cycles of load. 80
Figure 6.2.3 Mean stress at peak load along the bottom of the base. 81
Figure 6.2.4 Mean stress at peak load along a line 70 mm above the bottom of the base. 81
Figure 6.2.5 Vertical stress at peak load in the top of the subgrade. 82
Figure 6.2.6 Lateral permanent strain in the top of the subgrade versus lateral distance after 10 cycles of load. 82
Figure 6.2.7 Vertical permanent strain along the load plate centerline versus depth after 10 cycles of load. 83
Figure 6.2.8 Permanent surface deformation versus applied load cycles for reinforced sections. 83
Figure 6.2.9 Relative displacement between the base aggregate and the geosynthetic interface. 84
Figure 6.2.10 Interface shear stress between the base aggregate and the geosynthetic. 84
Figure 6.2.11 Permanent vertical strain in the top of the subgrade for various values of geosynthetic modulus and interface elastic slip (E_{slip}). 86
Figure 6.2.12 Average mean stress in the base aggregate for various values of geosynthetic modulus and interface elastic slip (E_{slip}). 86

CONVERSION FACTORS

The following conversion factors are required for interpretation of results contained in this report.

1 m = 3.28 ft
1 mm = 0.0394 in
1 kN = 225 lb
1 kN/m = 68.6 lb/ft
1 kPa = 0.145 psi
1 $MN/m^3 = 7.94\times10^{-6}$ lb/ft^3

EXECUTIVE SUMMARY

Experimental studies conducted over the course of the past 20 years have demonstrated both general and specific benefits of using geosynthetics as reinforcement materials in flexible pavements. Existing design solutions are largely empirically based and appear to be unable to account for many of the variables that influence the benefit derived from the reinforcement. Advanced numerical modeling techniques present an opportunity for providing insight into the mechanics of these systems and can assist with the formulation of simplified numerical methods that incorporate essential features needed to predict the behavior of these systems.

Previous experimental work involving the construction of geosynthetic reinforced test sections has shown several difficulties and uncertainties associated with the definition of reinforcement benefit for a single cycle of load application. Even though many reinforcement mechanisms are apparent and often times striking during the application of the first load cycle, the distinction between reinforced test sections is not nearly so clear as that which is seen when examining long term performance, where long term performance is defined in terms of permanent surface deformation after many load cycles have been applied.

This indicates the need for an advanced numerical model that is capable of describing the repeated load behavior of reinforced pavements. In particular, models for the various pavement layers are needed to allow for a description of the accumulation of permanent strain under repeated loads. To meet these needs, a finite element model of unreinforced and geosynthetic reinforced pavements was created. The material model for the asphalt concrete layer consisted of an elastic-perfectly plastic model where material property direction dependency could be added. This model allowed for the asphalt concrete layer to deform with the underlying base aggregate and subgrade layers as repeated pavement loads were applied.

A bounding surface plasticity model was used for the base aggregate and subgrade layers. The model is well suited for the prediction of accumulated permanent strains under repeated loading and is most suitable for fine-grained materials. A material model containing components of elasticity, plasticity, creep and direction dependency was formulated for the geosynthetic and calibrated against a series of in-air tension tests. A Coulomb friction model was used to describe shear interaction between the base aggregate and the geosynthetic. The model is essentially an elastic-perfectly plastic model, allowing for specification of the shear interface stiffness and ultimate strength. This model was calibrated from a series of pull out tests.

Finite element models were created to match the conditions in pavement test sections reported by Perkins (1999a). Membrane elements were used for the geosynthetic and a contact interface was used between the geosynthetic and the base course aggregate. Models of unreinforced and reinforced pavement sections were created and compared to test section results.

The results showed the model's ability to describe an accumulation of permanent strain and deformation in the system. The models were also capable of qualitatively showing mechanisms of reinforcement observed from pavement test sections. Exact predictions of pavement system response were difficult to achieve because of several deficiencies in the material models used and because of the run times needed for the models. The overriding model deficiency appears to be related to the model for the base course aggregate, which did not appear to be sufficiently sensitive to effects of restraint of the lateral motion of the material. The observation of certain reinforcement effects on response measures from the pavement system, such as vertical strain in the top of the subgrade and mean stress in the base course layer, indicate the model's suitability for use within the context of a mechanistic-empirical modeling approach. This approach requires

that the model be used for one load cycle application with certain stress and strain response measures being used outside the model within empirical damage models to predict long-term pavement performance. This approach is taken in a companion report for this project (Perkins, 2001) whose focus is on the development of a design model for this application.

1.0 INTRODUCTION

Experimental studies conducted over the course of the past 20 years have demonstrated both general and specific benefits of using geosynthetics as reinforcement materials in flexible pavements (Berg et al. 2000; Perkins and Ismeik, 1997). Existing design solutions are largely empirically based and appear to be unable to account for many of the variables that influence the benefit derived from the reinforcement. Advanced numerical modeling techniques present an opportunity for providing insight into the mechanics of these systems and can assist with the formulation of simplified numerical methods that incorporate essential features needed to predict the behavior of these systems.

Previous experimental work reported by Perkins (1999a) involving the construction of geosynthetic reinforced test sections has shown several difficulties and uncertainties associated with the definition of reinforcement benefit for a single cycle of load application. These results are summarized in Section 3 of this report. Even though many reinforcement mechanisms are apparent and often times striking during the application of the first load cycle, the distinction between reinforced test sections is not nearly so clear as that which is seen when examining long term performance, where long term performance is defined in terms of permanent surface deformation after many load cycles have been applied. For example, an examination of the dynamic surface deformation or the permanent surface deformation during the first load cycle often times does not show a clear distinction between reinforced test sections whose long term performance is dramatically different. In addition, reinforcement benefit, defined in terms of the increase in the number of load cycles that can be applied to a reinforced section as compared to that of an identical unreinforced test section, may increase as permanent surface deformation increases. For this reason, numerical models demonstrating purely elastic response and/or those models incapable of showing an accumulation of permanent surface deformation and strain within the pavement layers will require the use of certain simplifying assumptions regarding the use of empirical damage models relating short term or elastic response to long term behavior.

To allow for the modeling of growth of permanent surface deformation with applied load cycle, material models for the base aggregate, subgrade soils and most likely the geosynthetic need to be capable of exhibiting an accumulation of permanent strain with increased load cycle. The material model for the asphalt concrete needs to contain components allowing it to permanently deform and conform to the deformed upper surface of the base aggregate. In the

absence of this feature, the asphalt layer would attempt to rebound upwards upon the removal of load and would thereby create artificial tensile stresses acting upwards on the top of the base aggregate.

The finite element type chosen for the geosynthetic is a critical feature. Geosynthetics in this application do not offer reinforcement because of a resistance to bending, as would a sheet of material such as steel. Geosynthetics have essentially zero bending resistance. As such, a membrane element is the most appropriate element for the geosynthetic as these elements are formulated to have no in-plane bending resistance. To accurately model the effect of lateral restraint of base aggregate, a contact or interface model governing shear behavior between the geosynthetic and the surrounding soil is required.

The purpose of the research described in this report was to formulate a numerical model (finite element model) that contained these advanced features. Through this work, several critical modeling features have been noted and have been incorporated into a companion report whose focus is the development of a design model for reinforced pavements (Perkins, 2001).

2.0 LITERATURE REVIEW

The purpose of this literature review is to present material pertaining to finite element modeling of flexible pavements, finite element modeling of geosynthetic reinforced flexible pavements, geosynthetic tension testing and material modeling methods, and soil-geosynthetic interface interaction testing and modeling methods. This material is presented such that the modeling needs, as described in Section 1, and direction of this research can be placed within the context of existing work.

2.1 Numerical Modeling of Flexible Pavements

Numerical modeling of flexible pavements through the use of the finite element method has developed as the general finite element method has evolved. Early programs commonly used in practice typically consist of two-dimensional, axisymmetric models with linear or nonlinear elastic material properties for the various pavement layers (asphalt concrete, base, subbase and subgrade). Programs such as ILLI-PAVE, MICH-PAVE and ELSYM5 have been developed within this framework. Models using nonlinear elastic material models generally express the elastic modulus, or resilient modulus, as a function of stress state, whereas linear elastic models

treat the elastic modulus of the materials as a constant for all stress states. These programs typically apply load to the pavement surface uniformly over a circular area. Two-dimensional axisymmetric programs can only model a single wheel load application. Three-dimensional programs are capable of accounting for multiple wheel loads as well as moving wheel loads. Two-dimensional programs, such as KENLAYER, can also account for multiple wheel loads and moving wheel loads, but do so by superposition techniques, which are possible only for elastic material models. Chen et al. (1995) has provided a summary of programs commonly used for pavement modeling.

Programs developed using elastic material models are incapable of showing permanent deformation of the asphalt concrete surface as no permanent strains can develop in any of the material layers upon removal of the traffic load. These programs are typically used to evaluate the tensile strain at the bottom of the asphalt concrete layer and the vertical compressive strain in the top of the subgrade when traffic load is applied. Empirical expressions are then used to relate asphalt concrete tensile strain to fatigue and subgrade vertical compressive strain to permanent surface deformation.

Finite element programs capable of predicting permanent surface deformation due to the development of permanent vertical compressive strain in the base and subgrade layers generally must contain plasticity based constitutive models for these materials. Conventional plasticity models with isotropic hardening rules are well suited for the prediction of permanent strain under a single cycle of load application. Under uniform stress and strain conditions, such as that found in a triaxial test, these models typically show a response illustrated in Figure 2.1.1a where an elastic-plastic response is seen during the application of load and a purely elastic response is seen during unloading. Repeated application of a stress to the same level as that experienced during the initial load cycle results in purely elastic behavior with no accumulation of permanent strain. Actual material behavior under this type of repeated stress would be as shown in Figure 2.1.1b. Plasticity based material models with kinematic hardening rules can be formulated to match this type of material behavior.

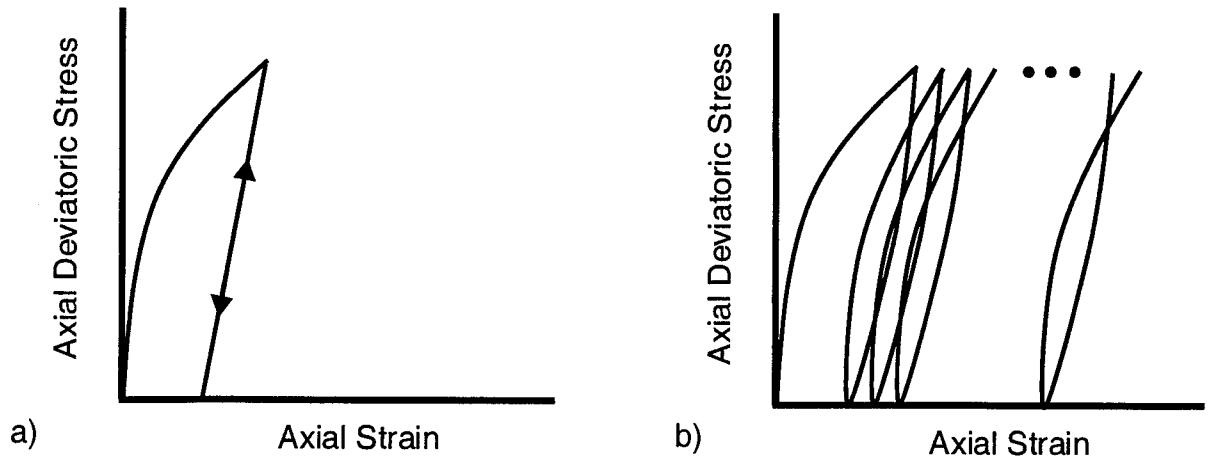

Figure 2.1.1 Cyclic behavior of unbound aggregate a) conventional plasticity models, b) idealized actual behavior and kinematic hardening models.

Finite element programs with plasticity models for the base and subgrade exhibiting the type of behavior illustrated in Figure 2.1.1a are capable of predicting permanent surface deformation after the application of the first traffic load (Bonaquist and Witczak, 1996; Kirkner et al., 1994, 1996) but, then tend to not predict well the accumulation of permanent deformation with increased load cycles. These types of models can show an accumulation of permanent surface deformation, as illustrated by Zaghloul and White (1993) and White et al. (1998), if the asphalt concrete layer is allowed to experience a decrease in thickness by virtue of being loaded, as is possible if a viscoelastic or an elastic-plastic model is used for this layer. Thinning of the asphalt concrete layer under a given load cycle allows the stress transmitted to the base and subgrade materials to be greater during the next load cycle, which then allows for additional plastic strains to develop.

The use of plasticity models with kinematic hardening rules allows for the growth of permanent surface deformation to be better predicted. Plasticity models of this type have been available since the 1970's (Dafalias, 1975) but have only recently been applied to pavement modeling. McVay and Taesiri (1985) described a bounding surface plasticity model that was developed and compared to results from repeated load triaxial tests. Ramsamooj and Piper (1992) described a model that was based on the model originally proposed by Prevost (1978). This model incorporated a kinematic hardening rule along with routines for pore water pressure generation and dissipation. The model was compared to cyclic triaxial tests on sands and clays. The model was used to show the importance of pore water dissipation through drainage on the

development of rut depth in a flexible pavement. Desai et al. (1993) and Wathugala and Desai (1993) have described a hierarchical plasticity model that accounts for cyclic loading. Research efforts at the US Army Corp of Engineers Waterways Experiment Station (Rollings et al., 1998) are focused on the implementation of models such as these in finite element codes for the prediction of permanent deformation of flexible pavements.

2.2 Numerical Modeling of Geosynthetic Reinforced Pavements

A number of studies have been conducted to examine the utility of finite element programs to predict the response of roadways reinforced with geosynthetics. Several of these studies have been performed in conjunction with experimental studies such that comparisons between model predictions and experimental results could be made. For the studies discussed below, Table 2.2.1 has been created to summarize the major features associated with each study's model.

Barksdale et al. (1989) adapted an existing finite element model to predict the response seen in the experimental portion of their study. The prediction of tensile strain in the base material was essential in determining the level of tensile strain developed in the geosynthetic, which in turn determined, in part, the benefit provided by the reinforcement. The cross-anisotropic linear elastic model used for the base was the only model capable of simultaneously predicting the lateral tensile strains in the bottom of the base and the small vertical strains in the bottom and upper part of that layer, as observed in the laboratory experiments.

The finite element model was calibrated and verified by using data from an unreinforced pavement section from a previous study and from the test data generated from one of the experimental test series of their study. The unreinforced pavement section used for calibration was strong in comparison to the sections described for their study. The finite element model was capable of predicting measured variables to within +/- 20 % for the strong unreinforced section. For the weaker sections used in the study described as part of their work, the finite element predictions were not as good. The strain in the geosynthetic was over predicted by about 33 % when the geosynthetic was located in the bottom of the base. It was under predicted by about 14 % when located in the middle of the layer. The vertical stress and vertical strain on the top of the subgrade was under predicted by about 50 %. The lateral strains were also under predicted by about 50 %. The model was not capable of predicting permanent strain or deformation in that all layers were linear elastic.

Table 2.2.1 Summary of Finite Element Studies of Geosynthetic Reinforced Pavements.

	Author						
	Barksdale et al. (1989)	Burd & Houlsby (1986)	Burd & Brocklehurst (1990)	Burd & Brocklehurst (1992)	Dondi (1994)	Miura et al. (1990)	Wathugala et al. (1996)
Analysis Type	Axi-symmetric	Plane strain	Plane strain	Plane strain	Three-dimensional	Axi-symmetric	Axi-symmetric
AC Constitutive Model	Isotropic, non-linear elastic	None	None	None	Isotropic, linear elastic	Isotropic, linear elastic	Isotropic elastoplastic, D-P
AC Thickness (mm)	Variable	None	None	None	120	50	89
Base Constitutive Model	Anisotropic, linear elastic	Isotropic, elastoplastic, Matusoka	Isotropic, elastoplastic, Matusoka	Isotropic, elastoplastic, Matusoka	Isotropic, elastoplastic, D-P	Isotropic, linear elastic	Isotropic, elastoplastic, D-P
Base Thickness (mm)	Variable	75	300	300	300	150	140
Geosynthetic Constitutive Model	Isotropic, linear elastic	Isotropic, linear elastic	Isotropic, linear elastic	Isotropic, linear elastic	Isotropic, linear elastic	Isotropic, linear elastic	Isotropic, elastoplastic, von Mises
Geosynthetic Element Type	Membrane	Membrane	Membrane	Membrane	Membrane	Truss	Solid continuum
Geosynthetic Thickness (mm)	None	None	None	None	None	None	2
Interface Elements & Model	Linear elastic-perfectly plastic	None	None	Elastoplastic, Mohr-Coulomb	Elastoplastic, Mohr-Coulomb	Linear elastic joint element	None
Subbase Constitutive Model	None	None	None	None	None	Isotropic, linear elastic	Isotropic, elastoplastic,HiSS δ_o
Subbase Thickness (mm)	None	None	None	None	None	200	165
Subgrade Constitutive Model	Isotropic, non-linear elastic	Isotropic, elastoplastic, von Mises	Isotropic, elastoplastic, von Mises	Isotropic, elastoplastic, von Mises	Isotropic, elastoplastic, Cam-Clay	Isotropic, linear elastic	Isotropic, elastoplastic, HiSS δ_o
Load Application	Monotonic	Monotonic, footing width = 75 mm	Monotonic, footing width = 500 mm	Monotonic, footing width = 500 mm	Monotonic, two rectangular areas, 240 mm x 180 mm	Monotonic, 200 mm diameter plate	Single cycle, peak pressure = 725 kPa on a 180 mm diameter plate
Remarks on Observed Improvement	Base layer could be reduced in thickness by 4-18 %. Greater improvement seen for sections with weak subgrade	Improvement seen after a penetration of 4 mm. Model overprecited improvement beyond a 4 mm displacement	Improvement seen after a penetration of 12 mm. Improvement increased with increasing geosynthetic stiffness.	Improvement seen after a penetration of 25 mm.	15-20 % reduction in vertical displacement, fatigue life of section increased by a factor of 2-2.5	5 % reduction in vertical displacement. Improvement level did not match experimental results.	20 % Reduction in Permanent Displacement

D-P: Drucker-Prager

A parametric study was conducted with the finite element model to calculate the lateral tensile strain at the bottom of the AC layer and the vertical strain at the top of the subgrade for a single load application. This was used for evaluations of fatigue resistance and to indicate the degree of rutting that would occur, which in turn was used to evaluate improvement in pavement performance for unreinforced and reinforced sections. Reinforcement improvement was quantified as the reduction in aggregate base thickness for a reinforced roadway giving the same tensile strain (fatigue) and vertical strain (reflecting permanent deformation) as that for the unreinforced section. Improvement was seen to increase with increasing geosynthetic stiffness, and to decrease with increasing subgrade stiffness and asphalt thickness. Optimal improvement was seen when the geosynthetic was placed between the bottom of the base and 1/3 up into the base layer.

Barksdale et al. (1989) used the 1972 AASHTO design method to determine design thickness for the sections with subgrade CBR strengths ranging from 3 to 10 and for two different traffic loading conditions. Using the more stiff geosynthetic, reductions in base course thickness ranged between 4 to 16 % when improvement was based on equal lateral strain in the bottom of the AC layer, and 6 to 18 % when improvement was based on equal vertical strain at the top of the subgrade. In general, more improvement was observed for sections with a weak subgrade and a thinner AC layer. The magnitude of the benefits defined in this study are less than those for a preponderance of experimental studies as summarized by Berg et al. (2000). Barksdale et al. (1989) felt that the mechanisms modeled were more suited for geotextiles and that additional research was needed to define the mechanisms of improvement associated with geogrids and to develop suitable models.

Burd and Houlsby (1986) developed a large strain finite element model for the purpose of examining experimental results of reinforced unpaved roads, but could be extended to include material elements representing an asphalt layer. A large strain formulation was included to account for the extensive rutting that can take place in unpaved roads. Interface elements were not included in the formulation, which implies perfect fixidity between the soil layers and the geosynthetic. The model was used to predict the response of a footing resting on a base layer with a geosynthetic layer placed between the base and the underlying subgrade. The model predictions were compared to experimental results and were shown to match reasonably well. The experimental results showed a slight improvement in the load-displacement curve for the

reinforced footing for footing penetrations less than 4 mm, while the model did not show improvements of this kind until the footing penetration exceeded 4 mm. Beyond a penetration of 4 mm, the improvement exhibited by the reinforced footing became significant for both the model and the experimental results, with the model over predicting the experimental results at larger displacements and with this over prediction becoming more significant as the footing displacement increased.

Burd and Brocklehurst (1990) applied this same model to a larger footing. Similar to the results of Burd and Houlsby (1986) the model did not show improvements in the load-displacement curve until a settlement of 12 mm was reached. The model was used in a parametric study to demonstrate the importance of the geosynthetic stiffness on improvement levels.

Burd and Brocklehurst (1992) extended this model to include interface elements. The model was used to predict the response of a footing placed on a base material over top a subgrade with reinforcement between the base and subgrade. The finite element analyses predicted negligible improvement in the load versus displacement response until a displacement of over 25 mm was reached. In general, the model with interface elements tended to show less improvement than the earlier version without these elements. In light of the results of Burd and Houlsby (1986), where model results were compared to experimental results, it appears that interface elements were needed only when large footing displacements were present.

Dondi (1994) used the commercial program ABAQUS to model a geosynthetic reinforced pavement. Load was applied to the pavement surface by two rectangular areas measuring 240 mm by 180 mm and representing a single pair of dual wheels. The wheels were separated by a distance of 120 mm. Each rectangular area experienced a peak loading pressure of 1500 kPa. Due to the loading geometry, a three-dimensional finite element analysis was performed. A cohesion of 60 kPa was assigned to the base course soil to avoid numerical instabilities. Different friction coefficients were used between the geosynthetic and the base and subgrade soils. Sections were analyzed with and without the geosynthetic layer and for two geosynthetics of differing elastic modulus.

The evaluation of stress and strain measures for elements in the base and in the subgrade indicated that the base layer experienced moderate increases in load carrying capacity for the reinforced cases while the strain in the subgrade was seen to decrease substantially for the

reinforced cases. The model indicated that the geosynthetic layer reduced the shear stresses and strains experienced by the subgrade. Vertical displacement of the loaded area was reduced by 15 to 20 % by the inclusion of the geosynthetic. The displacement of the unreinforced section was not indicated. An empirical power expression involving tensile strain in the AC layer was used to evaluate the fatigue life of the sections, showing that the life of the reinforced sections could be increased by a factor of 2 to 2.5 as compared to the unreinforced section.

Miura et al. (1990) performed a finite element analysis of a reinforced paved road in support of a laboratory and field experimental program. The section layer thicknesses were chosen to match the laboratory test sections. The results from the analysis of reinforced and unreinforced sections showed general agreement with results from the laboratory test sections where surface displacement and strain in the geosynthetic were plotted against distance from the centerline of the load. The improvement in the surface displacement for the reinforced section as compared to the unreinforced section was greatly underestimated by the finite element model as compared to the experimental results. The finite element model showed a reduction in displacement of 5 % while the experiment showed a 35 % reduction. The monotonic loading results from the finite element analysis were compared to the experimental results at 10,000 cycles of applied load. In this light, the finite element model was not intended to be an exact representation of the experiments but were intended more to shed light on the mechanisms involved in reinforcement.

Wathugala et al. (1996) used the commercial program ABAQUS to formulate a finite element model of a geogrid reinforced pavement. The base aggregate and subgrade soils were modeled using the hierarchical constitutive model developed by Desai et al. (1986) and Wathugala and Desai (1993). This model can account for non-linear behavior during non-virgin loading, which is particularly appropriate for cyclic loading applications. This feature was not used, however, with non-virgin loading modeled by a linear elastic response. No special interface models were used between the geogrid and the surrounding soil. The geosynthetic was given a thickness of 2.5 mm. The pavement section was analyzed with and without the geogrid layer. The addition of the geogrid was shown to reduce the permanent rut depth by approximately 20 % for a single cycle of load. This level of improvement was most likely due to the flexural rigidity of the geosynthetic, which is an artificial feature arising from the material and element model used for the geosynthetic.

2.3 Tension Testing and Material Modeling of Geosynthetics

Geosynthetic materials are known to exhibit thermo-visco-elastic-plastic, direction-dependent, and in some cases, normal stress dependent behavior. Elastic-plastic stress-strain behavior is illustrated schematically in Figure 2.3.1a where a non-linear response is seen during loading. A stiffer response is observed during unloading and is often approximated by a linear response indicative of the elastic behavior of the material. Otherwise, kinematic hardening concepts can be used to account for hysteretic behavior observed during unloading-reloading cycles. Thermo and visco behavior are illustrated in Figure 2.3.1b where decreasing temperature (T) or increasing strain rate result in a stiffer stress-strain response. Direction-dependent or anisotropic behavior implies a difference in stress-strain response depending on the direction that load is applied (Figure 2.3.1c). Ratcheting is often observed when constant load amplitude cyclic tension tests are performed (Figure 2.3.1d), where ratcheting refers to the accumulation of permanent strain with applied load cycle. Ratcheting is typically described by the incorporation of kinematic hardening concepts that allow the elastic region to grow, contract and shift with loading and unloading. Ratcheting may also be viewed as a viscous process where creep strains develop during each load cycle. Creep and stress relaxation are also material responses that are commonly associated with geosynthetic materials.

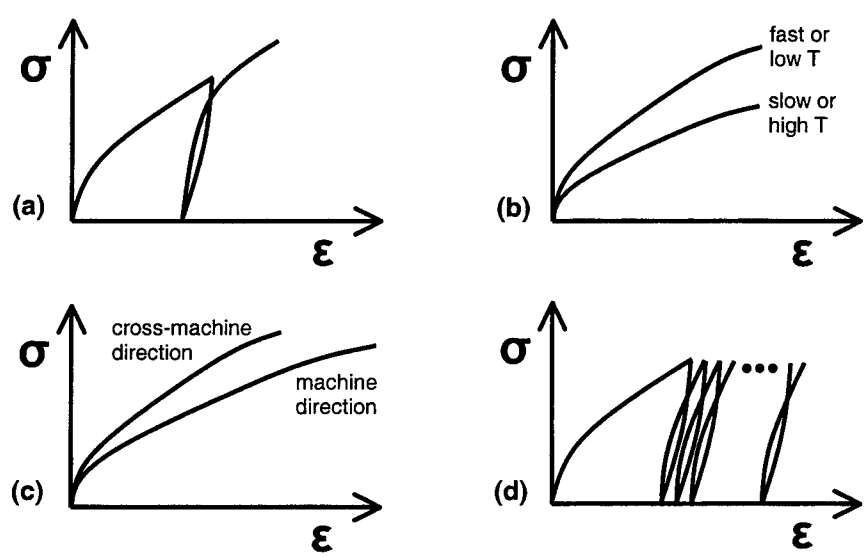

Figure 2.3.1 Illustration of a) elastic-plastic, b) thermo-visco, c) anisotropic and d) ratcheting stress-strain behavior.

A number of studies are available that show the characteristics described above. Monotonic and cyclic tensile tests performed on geogrids (Bathurst and Cai, 1994; Ling et al., 1998; Moraci and Montanelli, 1997) have shown that tensile stress-strain behavior is non-linear and that significant plastic strains develop. Constant load amplitude cyclic tests have shown that permanent strains accumulate with applied load cycle. Bathurst and Cai (1994) have shown that tensile stress-strain behavior is strain rate dependent. Ashmawy and Bourdeau (1996) have shown that for a nonwoven geotextile, stress-strain behavior is highly non-linear and that significant ratcheting occurs with cyclic loads. In contrast, a woven geotextile was shown to exhibit essentially linear elastic behavior during loading and unloading once the initial crimp is removed from the material. Additionally, ratcheting was seen to be relatively minor. A number of studies have shown that geosynthetics exhibit time-dependent creep behavior. Leshchinsky et al. (1997) have shown both creep and stress-relaxation behavior for geogrids, with stress-relaxation being observed to be as great as 50 % of the initial load for a polyethylene geogrid.

The above characteristics are complicated by the fact that most geosynthetics exhibit significant direction-dependent properties. Ingold (1983) has shown that strength anisotropy exists for a geonet product while many manufacturers commonly report different values for strength and tensile modulus in the machine and cross-machine directions of a given product. McGown et al. (1982) has shown that normal stress confinement of certain geosynthetics has an influence on load-strain behavior. In general, effects of confinement are significant for nonwoven geotextiles, much less significant for woven geotextiles and non-existent for geogrids.

The finite element method has been used for modeling the response of roadways and reinforced walls where in the course of this modeling, constitutive models for the geosynthetic have been implemented. As discussed in Section 2.2, for reinforced roadways, Barksdale et al. (1989), Miura et al. (1990), Burd and Brocklehurst (1992) and Dondi (1994) have used isotropic, linear elastic models for the geosynthetic, while Wathugala et al. (1996) used an isotropic, elastic-perfectly plastic model where plasticity corresponded to a von Mises strength criterion. For the dynamic analysis of reinforced walls, Yogendrakumar and Bathurst (1992) used a non-linear hyperbolic model that was capable of describing hysteretic behavior seen during unloading-reloading cycles. For the static analysis of reinforced walls, Karpurappu and Bathurst (1995) used a non-linear equation developed from isochronous load-strain-time test data.

From the laboratory tensile testing data summarized above, it is clear that the stress-strain behavior of geosynthetic materials is complex and that a general purpose material model must contain a number of components to describe this behavior. In Section 4.3, a material model for geosynthetic materials is presented that accounts for elastic, plastic, viscous and anisotropic behavior.

2.4 Soil-Geosynthetic Interface Interaction Testing and Modeling

Soil-geosynthetic interface interaction properties are commonly evaluated by performing direct shear tests (ASTM D 5321) and/or pull-out tests (McGown, 1978; Gourc et al., 1980; Ingold, 1983; Jewell et al. 1984; Bonczkiewicz et al., 1988). Direct shear tests are generally thought to be appropriate for situations where a block of soil moves relative to an essentially stationary geosynthetic and where the normal stresses on the geosynthetic are relatively low. Common applications for direct shear tests include covered side slopes for liners and soil block sliding along a geosynthetic layer for a reinforced slope. These situations correspond to conditions where extensibility of the geosynthetic does not play a significant role. Pull-out tests are appropriate for situations where interface shear resistance is governed by the extensibility of the geosynthetic and where the geosynthetic moves relative to the surrounding soil on both of it's sides. Common applications for pull-out tests include situations where the geosynthetic is anchored into a soil mass as loads are applied to the unanchored end, as in a reinforced wall or slope.

Shear strength parameters are the most common properties determined from these tests since the designs for which these properties are used are focused primarily on the limit state of the structure. An interface friction coefficient or angle is generally calculated from direct shear tests by dividing the ultimate shearing resistance by the normal pressure applied for the test. For pull-out tests, the ultimate shearing resistance is determined by dividing the ultimate pull-out load by two times the surface area of the embedded geosynthetic. The ultimate shearing resistance is then divided by the normal pressure to compute an interface friction coefficient. This approach assumes that the entire length of the geosynthetic is mobilized when ultimate pull out load is reached.

For design solutions providing a description of displacements for service loads less than limit state loads, information describing the shear load – displacement behavior of the interface

is necessary. This information is generally expressed in terms of an interface shear modulus defined as the ratio of mobilized shear resistance to shear displacement. Interface shear modulus can be defined directly from the initial part of the shear stress versus shear displacement curve from direct shear tests. For pull-out tests, the definition of interface shear modulus is more complex. The extensibility of the geosynthetic implies that the distribution of mobilized shear resistance varies along the geosynthetic and with displacement of the geosynthetic's loaded edge. These conditions imply that the pull-out test must be analyzed as a boundary-value problem with appropriate assumptions made regarding the constitutive relationship of the geosynthetic itself and for the interface interaction. Adjustment of parameters contained within the material model for the interface and subsequent comparison of the analysis to the pull-out results allows for the determination of the interface shear modulus.

For pavement system base reinforcement applications, it is not entirely clear which test is more appropriate for defining interface shear properties. On the one hand, the lateral movement of base aggregate atop the geosynthetic appears to be a condition of direct sliding as approximated by direct shear tests. On the other hand, strains in the geosynthetic can become appreciable after many cycles of load, meaning that extensibility of the geosynthetic becomes important and results from pull-out tests may be more appropriate. It is clear that an adequate description of the small displacement shear stress – displacement relationship is necessary to describe interaction, particularly for the early part of pavement loading.

Material models have been presented to describe ultimate shear resistance as a function of normal pressure and geosynthetic grid structure (Koerner et al., 1989; Jewell, 1990; Giroud et al., 1993). Interface shear stress – displacement relationships have been proposed for the purpose of evaluating pull-out test results (Juran and Chen, 1988; Yuan and Chua, 1991; Bergado and Chai, 1994; Abramento and Whittle, 1995; Ochiai et al., 1996; Sobhi and Wu, 1996; Alobaidi et al., 1997; Madhav et al., 1998; Gurung and Iwao, 1999; Perkins and Cuelho, 1999). Several finite element models have been developed to describe pull-out loading of geosynthetics (Wu and Helwany, 1987; Wilson-Fahmy and Koerner, 1993; Yogarajah and Yeo, 1994).

3.0 PRIOR TEST SECTION WORK

Previous work supported by the Montana Department of Transportation focused on the construction and evaluation of geosynthetic reinforced pavement test sections constructed in a

facility located at MSU. Test sections were constructed for the purpose of providing data to evaluate the mechanisms by which geosynthetics serve to reinforce flexible pavements and to provide data to which the numerical model, developed as part of this work, could be compared. Perkins (1999a,b) provides detailed information describing the pavement test facility, the construction process, instrumentation used and results obtained. Other papers related to this test section work are given in Perkins et al. (1998a,b, 1999). The purpose of Section 3 is to briefly describe the pavement test facility, the materials used, and to summarize the results from this previous study that are used for comparison to the numerical model.

3.1 Test Sections Constructed

The test sections used for comparison of the numerical model are given in Table 3.1.1. Of these test sections, 5 are control sections with no reinforcement and 7 are test sections with either a geogrid or geotextile reinforcement. The geosynthetic products used are described in Section 3.1.2. Two types of subgrade were used for the test sections listed in Table 3.1.1. A clay subgrade represents a weak subgrade with a CBR of approximately 1.5. The silty sand subgrade is a more competent material with a CBR of approximately 15. Additional details for these and the other pavement layer materials are given below.

Table 3.1.1 Comparison test section variables.

Section [a]	Nominal Base Thickness (mm)	Subgrade Type	Geosynthetic	Position
CS2	300	Clay	Unreinforced	Unreinforced
CS5	300	Clay	Geogrid B	Base/subgrade interface
CS6	300	Clay	Geotextile	Base/subgrade interface
CS7	300	Clay	Geogrid A	100 mm above base/subgrade interface
CS8	300	Clay	Unreinforced	Unreinforced
CS9	375	Clay	Unreinforced	Unreinforced
CS10	375	Clay	Geogrid A	Base/subgrade interface
CS11	300	Clay	Geogrid A	Base/subgrade interface
SSS1	200	Silty-sand	Unreinforced	Unreinforced
SSS2	200	Silty-sand	Geogrid A	40 mm above base/subgrade interface
SSS3	200	Silty-sand	Geotextile	40 mm above base/subgrade interface
SSS4	200	Silty-sand	Unreinforced	Unreinforced

[a] Nominal AC thickness = 75 mm for all sections.

3.1.1 Test Box and Loading Apparatus

A test box was constructed having inside dimensions of 2 m in width and length and 1.5 m in height and was constructed of reinforced concrete. Figure 3.1.1 shows a schematic of the pavement test facility. A load frame was constructed to rest and ride on I-beams set into the concrete walls. A load actuator, consisting of a pneumatic cylinder with a 305 mm diameter bore and a stroke of 75 mm, is used to apply a cyclic load to the pavement. A 50 mm diameter steel rod 300 mm in length extends from the piston of the actuator. The rod is rounded at its tip and fits into a cup welded on top of the load plate that rests on the pavement surface.

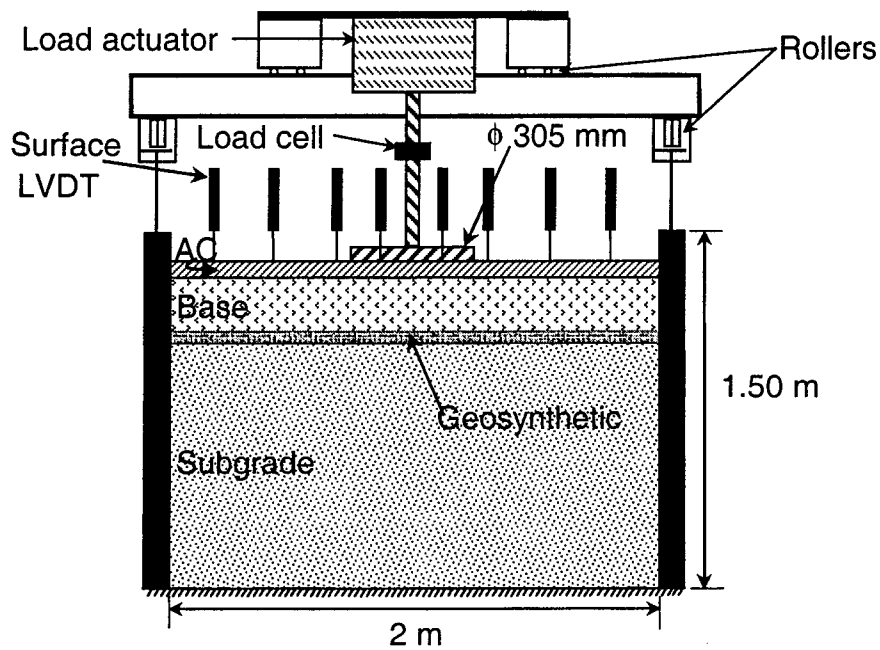

Figure 3.1.1 Schematic diagram of the pavement test facility.

The load plate consists of a 305 mm diameter steel plate with a thickness of 25 mm. A 4 mm thick, waffled butyl-rubber pad was placed beneath the load plate in order to provide a uniform pressure and avoid stress concentrations along the plate's perimeter.

A binary solenoid regulator attached to a computer controlled the load-time history applied to the plate. The software controlling the load pulse was set up to provide the load, or plate pressure pulse shown in Figure 3.1.2. This pulse has a linear load increase from zero to 40 kN over a 0.3 second rise time, followed by a 0.2 second period where the load is held constant, followed by a load decrease to zero over a 0.3 second period and finally followed by a 0.7

second period of zero load before the load cycle is repeated, resulting in a load pulse frequency of 0.67 Hz.

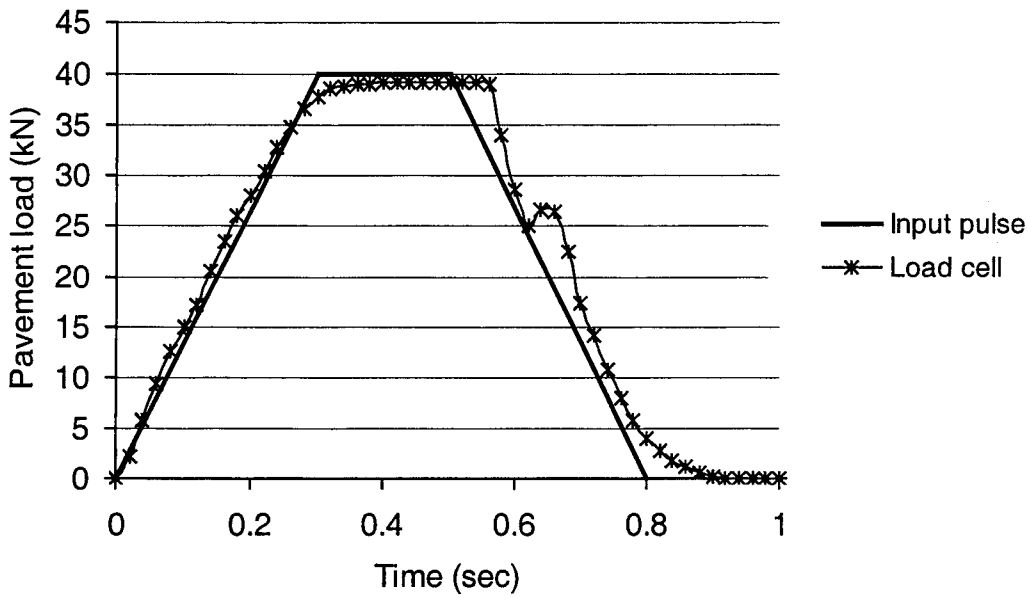

Figure 3.1.2 Input load pulse and corresponding load cell measurement.

The prescribed maximum applied load of 40 kN resulted in a pavement pressure of 550 kPa. This load represents one-half of an 80 kN axle load from an equivalent single axle load (ESAL) and hence represents one ESAL. The load frequency was selected to allow the data acquisition system time to store data before the next load pulse was applied. The average peak plate pressure and standard deviation over the course of pavement loading is given in Section 3.1.4 for each test section reported. The pavement load typically did not return to zero following the application of each load cycle. The average minimum load over the course of pavement loading is also given in Section 3.1.4 for each test section. Also shown in Figure 3.1.2 is the corresponding output from the load cell for a typical load application. The hump seen on the descending branch of the curve is due to back venting of air pressure into the solenoid and was characteristic of all load pulses.

3.1.2 Pavement Layer Materials

Hot-mix asphalt concrete was used for the test sections listed in Table 3.1.1. The aggregate gradation meets the Montana Department of Transportation specifications for a Grade A mix

design. Asphalt cement used was PG-58/28 and asphalt content was approximately six percent. A grain size distribution for the hot-mix aggregate is shown in Figure 3.1.3. As-constructed properties of the AC for each test section are given in Section 3.1.4. Results from indirect tension resilient modulus tests are presented in Section 4.1.

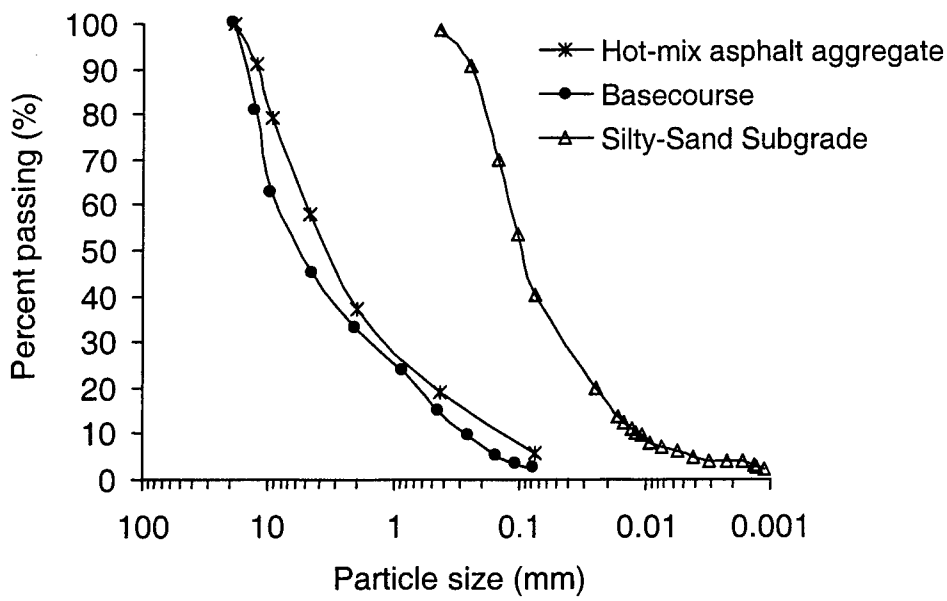

Figure 3.1.3 Grain size distribution of hot-mix aggregate, base course aggregate and silty sand subgrade.

The geosynthetics used for the test sections shown in Table 3.1.1 and their index properties as reported by the manufacturers are listed in Table 3.1.2. A series of tension tests were performed on these two materials and are reported in Section 4.3.1. Pull out tests were also performed on these two materials with the surrounding soil being the base aggregate used in these test sections with results presented in Section 4.4.1.

A crushed-stone base course was used for all experimental test sections. The base course grain size distribution is shown in Figure 3.1.3, where it is seen that 100 % passes the 19 mm sieve. The material is classified as an A-1-a or a GW. Specific gravity of the material is 2.63. Modified Proctor tests resulted in a maximum dry unit weight of 21.5 kN/m^3 at an optimum moisture content of 7.2 %. This material was typically compacted at a moisture content of 6.3 % and to a dry unit weight of 21 kN/m^3. As-constructed properties of the base course for each test section are given in Section 3.1.4. A series of triaxial tests were performed on this material and

are presented in Section 4.2 when the constitutive model for this material is described and calibrated. The triaxial tests yielded a drained friction angle of approximately 48 degrees.

Table 3.1.2 Geosynthetic material index properties.

	Geogrid A: Tensar BX-1100	Geogrid B: Tensar BX-1200	Geotextile: Amoco 2006
Material	Polypropylene	Polypropylene	Polypropylene
Structure	Punched Drawn, Biaxial	Punched Drawn, Biaxial	Woven
Mass/Unit Area (g/m^2)	215[1]	309[1]	250[3]
Aperature Size (mm)			
Machine Direction	25[1]	25[1]	None
Cross-Machine Direction	33[1]	33[1]	
Wide-Width Tensile Strength at 2 % Strain (kN/m)			
Machine Direction	5.06[2]	7.32[2]	4.25[4]
Cross-Machine Direction	8.50[2]	11.9[2]	13.6[4]
Wide-Width Tensile Strength at 5 % Strain (kN/m)			
Machine Direction	9.71[2]	13.4[2]	11.9[4]
Cross-Machine Direction	16.5[1]	22.9[2]	26.4[4]
Ultimate Wide-Width Tensile Strength (kN/m)			
Machine Direction	13.8[2]	21.1[2]	40.2[4]
Cross-Machine Direction	21.2[2]	31.3[2]	42.9[4]

[1] IFAI, 1994; [2] Tensar, 2001; [3] AMOCO, 1996; [4] AMOCO, 2001

To provide information on the influence of subgrade strength on reinforcement benefits, two subgrade materials were used in this study. A highly plastic clay subgrade was used to represent a soft subgrade while a silty-sand was used to represent a hard subgrade. The soft subgrade consisted of a CH or A7-(6) clay, having a liquid limit of 100 % and a plastic limit of 40 %. One hundred percent of the clay material passes the #200 sieve. Specific gravity of the clay is 2.70. Modified Proctor compaction tests resulted in a maximum dry density of 16.0 kN/m^3 occurring at an optimum moisture content of 20.0 %. The clay was compacted at a moisture content of approximately 45 % in order to obtain a California bearing ratio (CBR) of approximately 1.5.

The target moisture content of 45 % was established by conducting laboratory, unsoaked CBR tests. Figure 3.1.4 shows the variation of CBR with compaction moisture content. On this

figure, it is noted that only a relatively small change in CBR results between a moisture content range of 43 to 46 %.

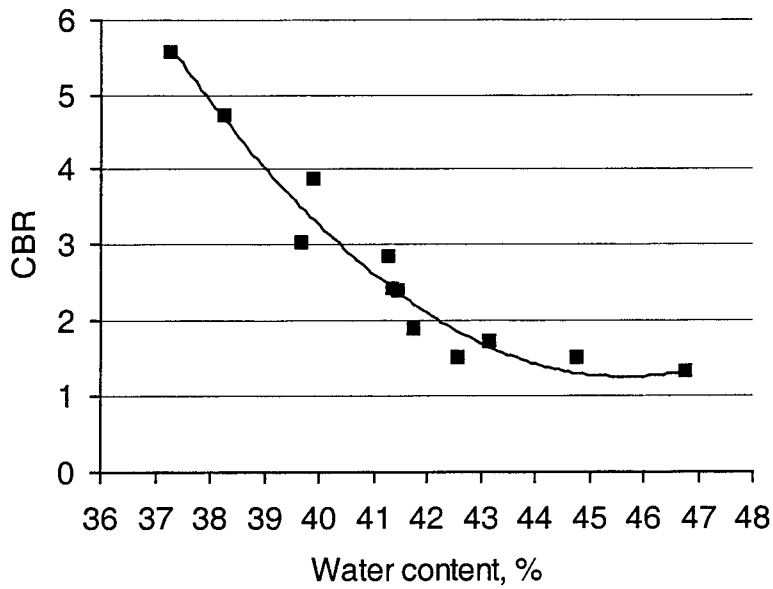

Figure 3.1.4 CBR versus compaction moisture content for the clay subgrade.

The hard subgrade (approximate CBR=15 at a moisture content of 14%) consisted of fines trapped from the baghouse of a local batch hot-mix plant. The material is classified as a SM or A-4, with 40 % non-plastic fines and a liquid limit of 18 %. Specific gravity of the silty-sand is 2.68. Modified Proctor tests resulted in a maximum dry density of 18.2 kN/m^3 occurring at a moisture content of 11.5 %. This material was typically compacted at a moisture content of 14.8 % and a dry unit weight of 17.5 kN/m^3.

As constructed properties of the compacted clay and silty sand subgrade in the test sections are given in Section 3.1.4. Shelby tubes were pushed into the subgrade during excavation of the sections for each test section. Undisturbed samples were used to conduct triaxial tests, with results presented in Section 4.2 where the constitutive model for the subgrade materials is presented and calibrated.

3.1.3 Instrumentation

An extensive array of instrumentation was used in the test sections to quantify the mechanical response of the pavement materials to pavement loading. This data has allowed for the description of reinforcement mechanisms and has provided data to which the numerical model

has been compared, as described in Section 5. The test sections contained instruments to measure applied pavement load, surface deflection, and stress and strain in the various pavement layers. Instrumentation has been categorized into sensors measuring applied pavement load, asphalt surface deflection, tensile strain in the asphalt concrete, stress and strain in the base course and subgrade, and strain on the geosynthetic. Data acquisition software was configured to record information on the full time-history of response for prescribed load cycles and maximum and minimum sensor response for other load cycles. A full description of the type of sensors used, installation techniques and the data acquisition used is given in Perkins (1999a).

3.1.4 As-Constructed Pavement Layer Properties

Perkins (1999a) has described the construction techniques used for the test sections and the quality control measures taken to collect data during and after construction. Quality control measures were taken to provide information on the consistency of the pavement layer materials between test sections. These measures included measurement of in situ water content and dry density in the subgrade and base course layers during construction and during excavation, DCP tests on the compacted subgrade during construction and during excavation, measurement of in-place density of the compacted AC, and measurement of in-place density of the AC from 100 mm and 150 mm diameter AC drill cores. Additional tests were performed on both bulk AC samples and the 100 mm diameter cores. These tests included determination of asphalt cement content, air voids, rice specific gravity, Marshall stability, penetration and kinematic viscosity. A statistical analysis of these measures was provided and discussed by Perkins (1999a) and illustrated which sections could be directly compared. The purpose of this section is to summarize those properties which impact input parameters to the numerical model presented in Section 5.

As-constructed asphalt concrete properties for the test sections are given in Table 3.1.3. Test section temperature is determined from average room temperature over the course of the test. Thickness, density and air voids were determined from direct measurements on 100 mm and 150 mm diameter cores taken from the test sections. Asphalt content was determined from bulk samples. Marshall stability and flow were determined from 100 mm cores taken from the test sections.

Table 3.1.3 As-constructed asphalt concrete properties.

Section	Test Section Temperature (°C)	Thickness (mm)	Density (kN/m^3)	Air Voids (%)	Asphalt Cement (%)	Marshalls	
						Stability (lb)	Flow
CS2	17	78	23.1	3.3	6.8	2013	26
CS5	19	76	22.6	5.6	6.1	2292	13
CS6	21	75	23.3	3.1	6.6	2471	18
CS7	24	75	22.9	4.3	6.6	1979	16
CS8	24	76	23.1	3.3	6.1	2527	15
CS9	26	79	22.7	5.2	6.3	2167	14
CS10	18	75	22.9	4.3	6.5	2190	13
CS11	18	77	23.4	1.9	6.0	2480	20
SSS1	21	78	23.0	4.1	5.4	2956	17
SSS2	26	79	22.6	6.3	5.7	2043	18
SSS3	16	77	22.4	6.7	6.2	1372	17
SSS4	16	78	22.8	4.4	6.1	2125	17

As-constructed measurements of the base aggregate and subgrade are listed in Table 3.1.4 and Table 3.1.5, respectively. Table 3.1.6 provides information on loading conditions for each test section.

Table 3.1.4 As-constructed base course properties.

Section	Thickness (mm)	Dry Density (kN/m^3)
CS2	300	20.6
CS5	300	20.6
CS6	300	21.0
CS7	300	20.6
CS8	300	20.7
CS9	375	20.9
CS10	375	20.5
CS11	300	20.5
SSS1	210	20.6
SSS2	205	20.7
SSS3	200	20.8
SSS4	200	21.1

Table 3.1.5 As-constructed subgrade properties.

Section	Thickness (mm)	Moisture Content (%)	Dry Density (kN/m^3)
CS2	1045	44.8	11.4
CS5	1045	44.9	11.4
CS6	1045	44.4	11.1
CS7	1045	44.2	11.4
CS8	1045	44.8	11.5
CS9	970	44.9	11.4
CS10	970	44.9	11.3
CS11	1045	45.1	11.4
SSS1	1128	14.7	17.0
SSS2	1131	14.9	17.0
SSS3	1147	14.8	17.1
SSS4	1145	14.8	17.1

Table 3.1.6 Test section loading conditions.

Section	Average Peak Load (kN)	Peak Load Standard Deviation (kN)	Average Minimum Load (kN)
CS2	40.1	0.27	1.0
CS5	40.1	0.34	1.2
CS6	39.9	0.37	1.3
CS7	40.0	0.22	1.3
CS8	40.1	0.21	1.2
CS9	39.9	0.26	1.6
CS10	40.1	0.32	1.2
CS11	40.0	0.44	1.0
SSS1	40.1	0.89	2.2
SSS2	40.3	0.34	1.2
SSS3	40.2	0.73	1.3
SSS4	40.5	0.47	1.0

3.2 Summary of Results

Presented in Figures 3.2.1, 3.2.2 and 3.2.3 are results of permanent surface deformation versus load cycle applied to each of the test sections. Sections CS2 and CS8 are duplicate unreinforced test sections with identical pavement layers. Test sections CS5, 6, 7 and 11 can be compared to CS2 and 8 to evaluate TBR. Similarly, test section CS10 can be compared to CS9 for evaluation of TBR. Test sections SSS1 and 4 are duplicate unreinforced test sections. These test sections showed a better performance, as defined in terms of permanent surface deformation, in comparison to the two reinforced test sections (SSS2 and SSS3). As described in Perkins

(1999a), the principal reason for this observation was the higher air voids of the asphalt concrete in test sections SSS2 and 3 as compared to SSS1 and 4 and the resulting reduced stiffness of this layer. Had the asphalt concrete been more comparable between these sections, it is believed that little differences in pavement performance would have been seen between reinforced and unreinforced sections, meaning that reinforcement had little impact for sections with this structural section and subgrade strength.

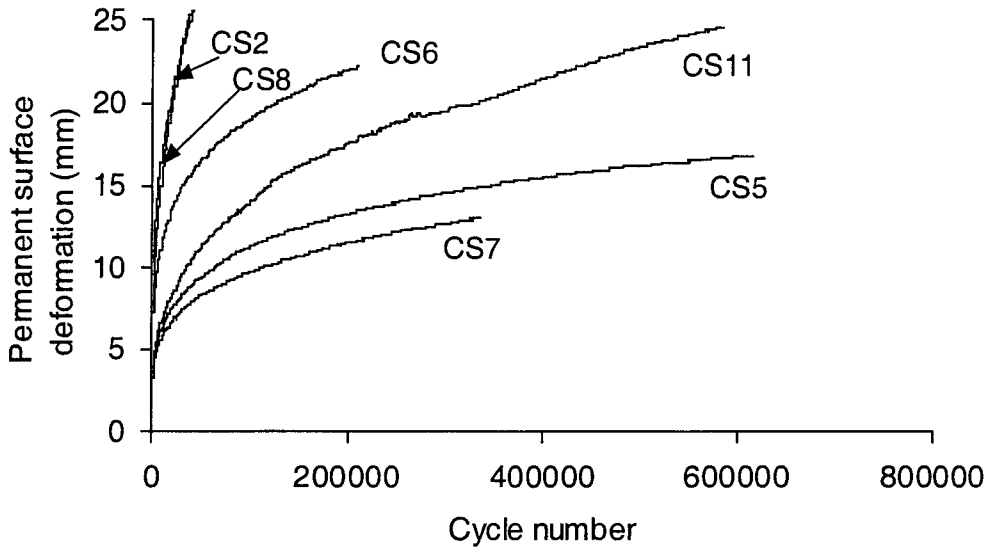

Figure 3.2.1 Permanent surface deformation versus load cycle (CS2, 5, 6, 7, 8, 11)

Figures 3.2.4 and 3.2.5 provide values of TBR computed at permanent surface deformation values ranging from 1 mm to 25 mm. In Figure 3.2.4, sections CS5, 6, 7 and 11 were compared to section CS2 to calculate TBR values. In Figure 3.2.5, section CS10 was compared to CS9. Perkins (1999a) provides further results from the instrumentation contained in these sections. These results are shown as needed in Section 5.3 when predictions from the model are compared to test section results.

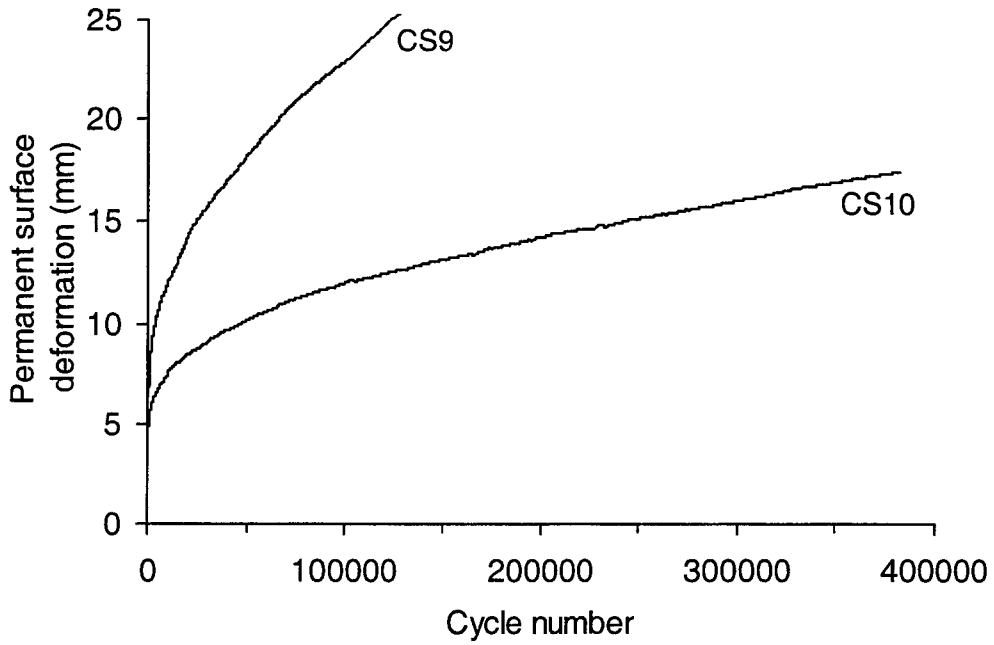

Figure 3.2.2 Permanent surface deformation versus load cycle (CS9, 10)

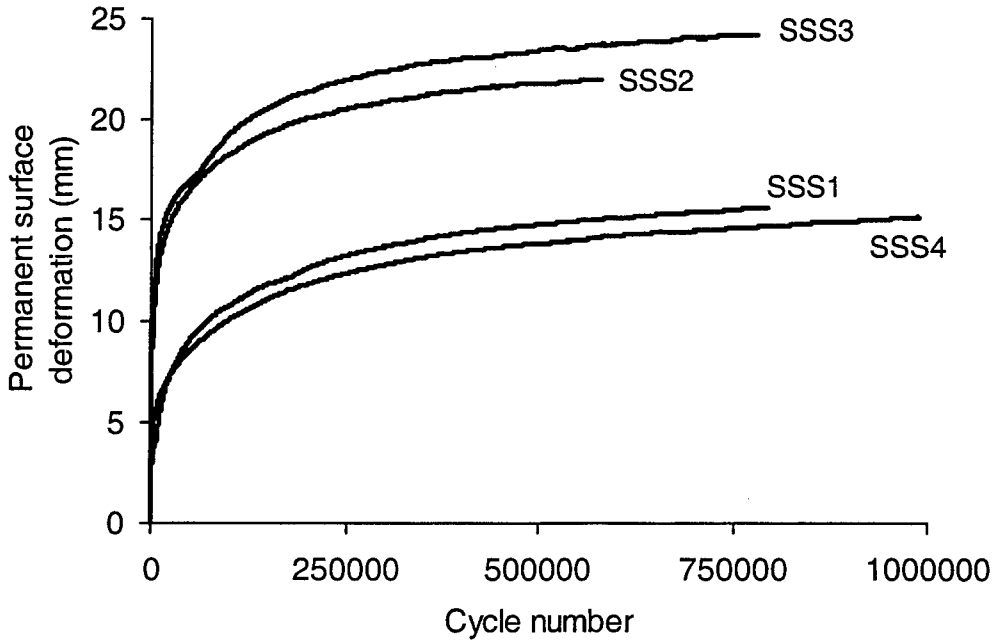

Figure 3.2.3 Permanent surface deformation versus load cycle (SSS1, 2, 3, 4).

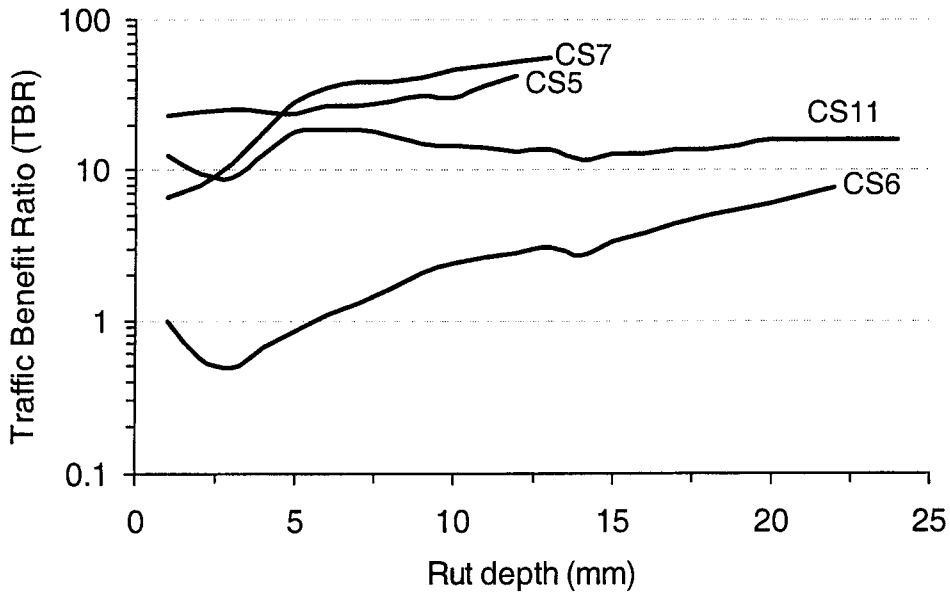

Figure 3.2.4 TBR for sections CS5, 6, 7 and 11 relative to section CS2.

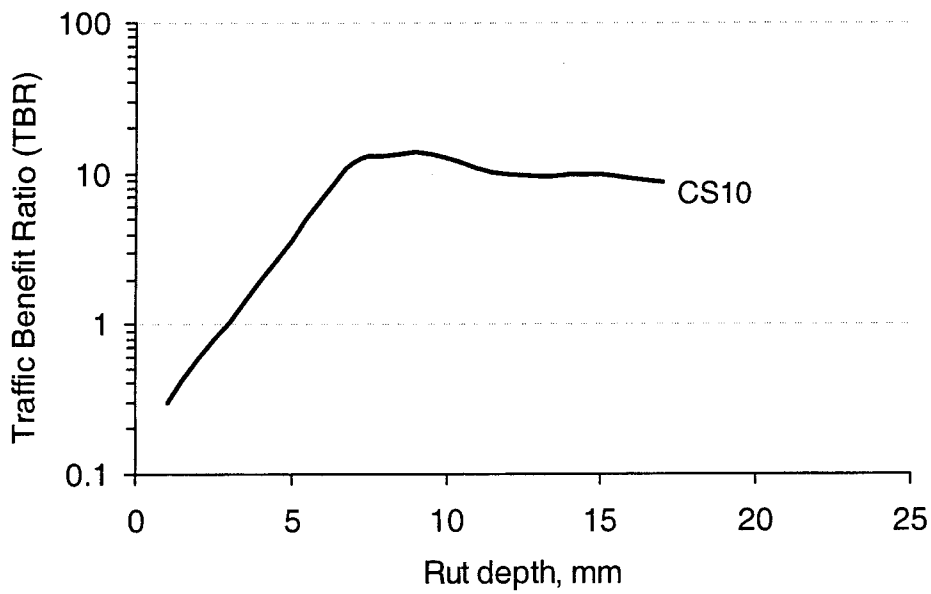

Figure 3.2.5 TBR for section CS10 relative to section CS9.

4.0 PAVEMENT LAYER MATERIAL MODELS AND CALIBRATION TESTS

The numerical finite element model developed as part of this work was designed to match stress, strain and displacement measurements in test sections described in Section 3. These measurements describe the dynamic stress response, the accumulation of permanent strain in the pavement layers and the development of permanent surface deformation for unreinforced and reinforced flexible pavements. To accomplish these objectives, material models that allow for the development and accumulation of permanent strain with applied load cycle were required. In addition, a contact or interface model was required to describe shear behavior between the geosynthetic and the surrounding soil. This section describes the various material models used to satisfy these objectives.

4.1 Asphalt Concrete

Measurements from test sections described in Section 3 indicated that less than 15 % of the permanent surface deformation at the end of a test was due to permanent vertical compression of the asphalt concrete (AC) below the load plate. Given that asphalt concrete is a viscous material and that it exhibits permanent strain, ideally a visco-plastic material model would be used. A number of factors precluded the use of a model of this type. These factors include the relatively small contribution to permanent deformation due to the AC layer, the lack of relevance of properties pertaining to the development of permanent deformation in this material on benefits derived from the reinforcement, the difficulty in determining visco-plastic material parameters through established laboratory tests, the complexity of material models used for the other pavement layers and the desire to increase computational efficiency.

Initially, a simple linearly elastic model was selected. After initial use of this material model in the finite element model, it was observed that the rebound of this elastic layer after the applied load was returned to zero created vertical tensile stresses on the top of the base layer. For this reason, the model was extended to include a plasticity component. The plasticity was introduced by specification of an ultimate yield stress corresponding to a perfect plasticity hardening law.

Incorporation of this material model into the finite element model described in Section 5 showed that vertical stresses in the subgrade close to the centerline of the load plate tended to be under predicted, while vertical stresses at a radius greater than approximately 300 mm tended to

be over predicted. In addition, the predicted deflected shape of the asphalt surface tended to be more flat than that seen from test section results. These findings suggested that the use of isotropic elastic and plastic properties for the asphalt concrete tended to cause this layer to act too much like an elastic slab distributing the stress too broadly. For these reasons, direction dependency, or anisotropy, was added for the elastic and plastic properties. The addition of anisotropy essentially allowed for the reduction of the flexural stiffness of the asphalt layer while maintaining the vertical stiffness in compression.

Direction dependence of elastic properties was prescribed though the use of a linear, orthotropic elastic constitutive matrix. Orthotroic linear elasticity is described by three moduli (E_{ij}), three independent Poisson's ratios (ν_{ij}), and three shear moduli (G_{ij}), resulting in the elastic constitutive matrix (Note: Appendix A contains a listing of all symbols and notation used in the report)

$$\begin{Bmatrix} \varepsilon_x \\ \varepsilon_y \\ \varepsilon_z \\ \gamma_{xy} \\ \gamma_{xz} \\ \gamma_{yz} \end{Bmatrix} = \begin{bmatrix} 1/E_x & -\nu_{yx}/E_y & -\nu_{zx}/E_z & 0 & 0 & 0 \\ -\nu_{xy}/E_x & 1/E_y & -\nu_{zy}/E_z & 0 & 0 & 0 \\ -\nu_{xz}/E_x & -\nu_{yz}/E_y & 1/E_z & 0 & 0 & 0 \\ 0 & 0 & 0 & 1/G_{xy} & 0 & 0 \\ 0 & 0 & 0 & 0 & 1/G_{xz} & 0 \\ 0 & 0 & 0 & 0 & 0 & 1/G_{yz} \end{bmatrix} \begin{Bmatrix} \sigma_x \\ \sigma_y \\ \sigma_z \\ \tau_{xy} \\ \tau_{xz} \\ \tau_{yz} \end{Bmatrix} \tag{4.1.1}$$

where the subscripts x and y denote the in-plane horizontal directions, and z denotes the vertical direction. Plasticity was described in terms of an ultimate yield stress, σ^{o}_{AC}, and six plastic potential ratios, R_{ij}, given in Equation 4.1.2, whose values are typically less than one and describe the reduction in yield stress in each respective direction.

$$\begin{Bmatrix} R_x \\ R_y \\ R_z \\ R_{xy} \\ R_{xz} \\ R_{yz} \end{Bmatrix} = \frac{1}{\sigma^{o}{}_{AC}} \begin{Bmatrix} \bar{\sigma}_x \\ \bar{\sigma}_y \\ \bar{\sigma}_z \\ \sqrt{3}\,\bar{\tau}_{xy} \\ \sqrt{3}\,\bar{\tau}_{xz} \\ \sqrt{3}\,\bar{\tau}_{yz} \end{Bmatrix} \tag{4.1.2}$$

Values of elastic modulus (E_z), Poisson's ratio, and yield stress (σ^{o}_{AC}) in the principal direction of loading (i.e. the z-direction) were determined by conducting indirect tension resilient

modulus tests per ASTM D4123, where these tests were performed at the Asphalt Institute, Lexington, Kentucky. Tests were performed on 150 mm diameter samples cored from the test sections described in Section 3. Four 150 mm diameter cores were typically taken from each test section upon the completion of the tests and were taken from areas outside the footprint of the load plate. An additional six 100 mm cores were also obtained. Percent air voids was determined for each core with the average air voids computed. Resilient modulus was typically determined for two 150 mm cores from most sections. These cores were chosen to bracket as closely as possible the average air voids for the test section. Resilient modulus tests were performed at the average room temperature existing during the time the corresponding test section was loaded and were performed at three frequencies of loading (0.33, 0.5 and 1 Hz) and at two test positions corresponding to a 90 degree rotation. At the end of resilient modulus testing, the samples were loaded to failure to determine the ultimate strength of each core. Values of resilient modulus and Poisson's ratio are reported in Table 4.1.1 and are average values from each test rotation and testing frequency.

Table 4.1.1 Indirect tension resilient modulus test results.

Test Section	IDT Test Temperature (degree C)	Specimen Air Voids (%)	Average Resilient Modulus (MPa)	Average Poisson's Ratio	Ultimate Tensile Strength (kPa)
SSS3-1	15	2.93	4583	0.34	1273
SSS3-3	16	4.17	3748	0.34	1009
SSS3-4	15	5.32	3032	0.30	938
SSS4-1	15	4.25	4519	0.26	1218
SSS4-2	15	3.38	4596	0.31	1288
SSS4-4	16	5.57	2826	0.15	888
CS2-3	17	1.97	3668	0.42	828
CS2-4	17	1.97	4094	0.36	901
CS5-3	24	5.12	1150	0.22	585
CS6-2	21	2.47	1934	0.35	604
CS7-1	24	4.46	1741	0.31	538
CS7-3	24	2.66	2049	0.41	581
CS8-2	24	2.87	1723	0.38	567
CS9-2	26	4.09	1356	0.41	447
CS9-4	26	6.10	1188	0.33	468
CS10-2	18	2.96	2944	0.42	977
CS11-1	25	1.23	1796	0.95	449
CS11-4	25	1.88	1538	0.32	441

The IDT test results show a strong dependency on test specimen temperature and a lesser dependence on specimen air voids. The dependence on air voids appears to become stronger as the test temperature decreases. Given the consistency between certain sets of results from the test sections, it would appear that the difference in actual temperature in the asphalt concrete during the period over which pavement loading occurred between test sections is less than that implied by the values of room temperature reported in Table 3.1.3. For instance, test sections CS2 and CS8 were identical unreinforced test sections that displayed nearly identical pavement loading performance. The difference in room temperature for the two tests was reported as 7 degrees C. The IDT tests performed at this temperature difference resulted in a significant difference in modulus of the AC, which did not appear to be evident from the test section results. It is believed that the difference in actual AC temperature in the test sections was moderated by the presence of the large body of soil upon which AC rested and is less than that implied by room temperature measurements. Values for the AC properties listed in Equations 4.1.1 and 4.1.2 are provided in Section 6 for the models analyzed.

4.2 Base Aggregate and Subgrade

The constitutive model used for both the base aggregate and the subgrade soil is based on the bounding surface concept originally developed by Dafalias (1975) and extended for the description of isotropic cohesive soils by Dafalias and Hermann (1982) and later updated by Dafalias and Hermann (1986). The model is described in terms of two surfaces represented in the stress space shown in Figure 4.2.1. The parameters I and J represent the first stress invariant and the square root of the second deviatoric stress invariant, respectively, and, in general terms, are reflective of mean normal stress and shear stress, respectively. These surfaces are also a function of the lode angle, α, defined in terms of the third deviatoric stress invariant. The lode angle reflects stress paths ranging from triaxial compression to triaxial extension.

The larger surface shown in Figure 4.2.1 represents the bounding surface, which in a conventional plasticity model is equivalent to a yield surface. The second surface shown in Figure 4.2.1 denotes an elastic zone. Stress states within the elastic zone produce purely elastic behavior. Stress states lying between the elastic zone and the bounding surface are capable of producing both elastic and inelastic behavior. As the stress state approaches the bounding surface, the rate of plastic strain increases. In a conventional plasticity model, the surface for the

elastic zone is coincidental with the bounding surface, meaning that stress states lying below the current yield surface always produce purely elastic behavior. This feature of conventional plasticity models limits their use for predicting the accumulation of permanent strain in pavement layers under the application of repeated traffic loads, as explained in Section 2.1.

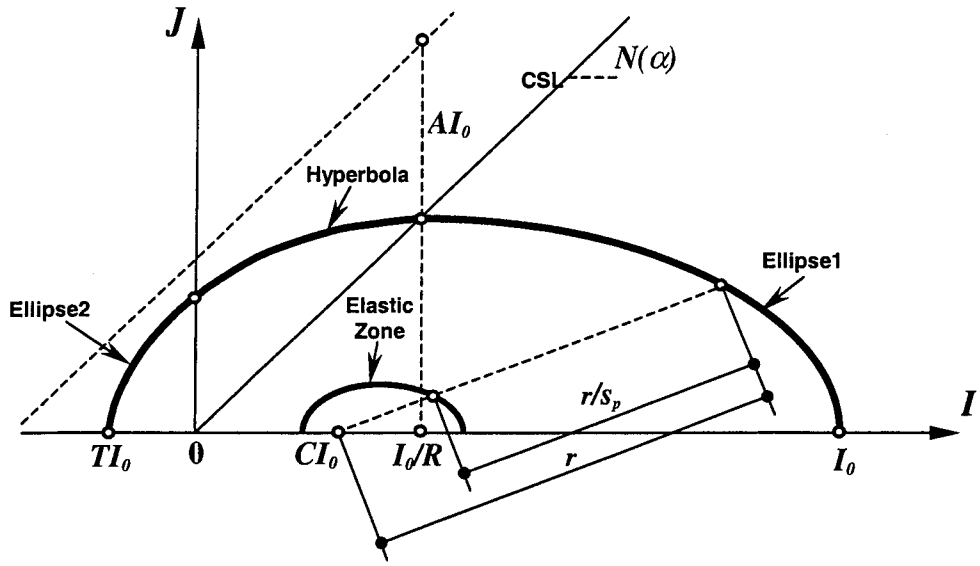

Figure 4.2.1 Schematic illustration of the bounding surface plasticity model.

A radial mapping rule is used to locate a point on the bounding surface corresponding to some state of stress inside or on the bounding surface. This mapping rule is illustrated by the dashed line in Figure 4.2.1 having an origin on the I axis at the value CI_o, where C is a material parameter and I_o is defined below. This mapping rule is necessary to prescribe yielding characteristics determined from the image point on the bounding surface to the current state of stress.

The bounding surface concept is general and permits the inclusion of any type of formulation for a yield surface, which is taken to represent the formulation for the bounding surface. The bounding surface used in the current model consists of three segments, as illustrated in Figure 4.2.1. The adoption of a combined surface allows greater flexibility in assigning behavior within the tension region of the stress space, the importance of which is discussed below. The bounding surface model used for the base aggregate and the subgrade soil uses a yield surface formulation extended from critical state soil mechanics models (Schofield and Wroth, 1968). A critical state line, defining the failure state of the material, is given by a line with a slope of N, where N is a function of the lode angle and is related to the slope of the critical

state line, M, in p-q stress space, and where M is given in terms of the material's drained friction angle as

$$M = \frac{6\sin\phi}{3-\sin\phi} \tag{4.2.1}$$

This formulation specifies the current size of the bounding surface in terms of the parameter I_o, the value of which reflects the amount of preloading or preconsolidation of the material. The value of I_o/R represents the value of I at the intersection of the bounding surface and the critical state line. The parameter R defines the ratio of the major to minor axes of ellipse 1 and is a material constant.

The quantity TI_o defines the intersection of ellipse 2 with the I axis in the tension region and dictates the tensile strength of the material, with the tensile strength changing depending on the value of I_o as dictated by overconsolidation. The parameter T is a material constant and can be set to a low value to model materials with little tensile strength.

The remaining point defining the shape of the bounding surface is the intersection of the surface with the J axis. This intersection point is governed by the material constant A. Small values of A pertain to materials with little cohesion. The parameters R, A and T are known as shape factors. The parameter s_p defines the size of the elastic zone. A value of 1 means that the elastic zone shrinks to a point located at the projection center, CI_o. As s_p increases to infinity, the elastic zone becomes larger and approaches the bounding surface.

The model contains another five material parameters in addition to those listed above. The first two (m and h) are associated with the hardening rule. The next two (λ and κ) are associated with the critical state soil mechanics definition of compression behavior in a void ratio vs. natural logarithm plot and are related to the compression index, C_c, and the swelling index, C_s, as defined from consolidation tests, by Equations 4.2.2 and 4.2.3.

$$\lambda = \frac{C_c}{2.303} \tag{4.2.2}$$

$$\kappa = \frac{C_s}{2.303} \tag{4.2.3}$$

The last parameter is Poison's ratio, ν. The shear modulus, G, and elastic modulus, E, are then determined from Equations 4.2.4 and 4.2.5.

$$G = \frac{3(1-2\nu)(1+e_{in})}{6\kappa(1+\nu)}\left(\langle I - I_L \rangle + I_L\right) \tag{4.2.4}$$

$$E = \frac{3(1-2\nu)(1+e_{in})}{3\kappa}\left(\langle I - I_L \rangle + I_L\right) \tag{4.2.5}$$

where I is the current mean hydrostatic stress, I_L is taken as a constant equal to atmospheric pressure and e_{in} is the initial void ratio of the material. According to these equations, shear modulus and elastic modulus will increase as the mean normal stress increases. The model contains the ability to define separate material constants for M, R, A and h for stress paths in compression and extension. In the absence of data to support a proper selection of these terms, values of these parameters were taken to be equal in extension and compression. A summary of material parameters for the model is given in Table 4.2.1, where all parameters except I_L are dimensionless. Steps required for the calibration of these constants is described by Kaliakin et al. (1987).

Table 4.2.1 Listing of bounding surface model material constants

Parameter	Name	Range of Values
λ	Virgin compression slope	0.1-0.2
κ	Swell/recompression slope	0.02-0.08
M	Slope of critical state line in p-q stress space	0.8-1.4
ν	Poisson's ratio	0.15-0.3
I_L	Atmospheric pressure	101 kPa
R	Shape parameter	2-3
A	Shape parameter	0.02-0.2
T	Shape parameter	0.05-0.15
C	Projection center parameter	0.0-0.5
s_p	Elastic zone parameter	1-2
m	Hardening parameter	0.02
h	Hardening parameter	5-50

The model is not ideally suited for the description of granular soils since it has been formulated in terms of critical state soil mechanics concepts. In particular, the parameters λ and κ often times do not adequately define the compression behavior of granular soils. While the shape parameters describing the cohesion and tensile strength (A and T) can be set low to mimic the lack thereof in granular soils, some finite level of cohesion and tensile strength is always

predicted. In addition numerical instabilities can sometimes result when A and T are given low values. This model, however, was viewed as adequate for the description of the base aggregate for the purposes of this research. Any limitations associated with the use of this model will be explored later in this report.

A series of isotropically consolidated undrained conventional triaxial compression tests were performed on the base aggregate and subgrade materials to calibrate the material properties contained in Table 4.2.1. Additional isotropically consolidated drained conventional triaxial compression tests were performed on the base aggregate material. Data was collected during consolidation for all tests to aid in calibration of the model parameters describing compression behavior. Tests were performed at overconsolidation ratios of 1, 2 and 6 as needed for calibration of material parameters (Kaliakin et al., 1987). These tests resulted in the parameters listed in Table 4.2.2 for the base aggregate and two subgrade soils.

Table 4.2.2 Material model parameters for base aggregate and subgrade soils.

Parameter	Values		
	Clay Subgrade	Silty Sand Subgrade	Base Aggregate
λ	0.236	0.022	0.02
κ	0.15	0.005	0.0018
M	0.65	1.6	1.6
M_E/M_C	1.0	1.0	1.0
ν	0.1	0.2	0.15
I_L (kPa)	101.4	101.4	101.4
R	1.75	1.4	1.5
A	0.03	0.02	0.015
T	0.03	0.01	0.01
C	0.0	0.0	0.0
s_p	1.1	1.1	1.2
m	0.02	0.02	0.02
h	15.0	15	20.0
I_o (kPa)	315	750	3900

4.3 Geosynthetics

In Section 2.3, it was shown that the stress-strain behavior of geosynthetic materials exhibits components of elasticity, plasticity and creep and is direction, time and temperature dependent. Of interest to this project is whether and by how much these material features influence the performance of geosynthetics used for reinforcement in flexible pavement systems. This question

has several levels of consideration. The overall objective of the numerical model is to provide a reasonable match of the results from test sections described in Section 3.0. In light of only this consideration, the model for the geosynthetic would need only to account for conditions present in this test facility. Since temperature was relatively constant for all test sections constructed, incorporation of the dependence of geosynthetic properties on temperature was not necessary and the model for the geosynthetic was calibrated from tension tests conducted around the same temperature as that in the test sections. Measurement of strain on the geosynthetics from the test sections indicated permanent strain as high as 2.5 %. Measurement of dynamic strain indicated an induced load in the material as high as 2.6 kN/m. These results indicate that plastic strains occur in the materials and that these strains accumulate with applied load cycle. The latter observation suggests that ratchetting occurs, as defined in Section 2.3.

These observations suggest that all factors of elasticity, plasticity, creep and direction dependence are potentially important. The philosophy taken in this work was to assume that each of these properties was important and that a material model for the geosynthetic should be formulated to account for each.

Presented in the sections that follow is a constitutive model for geosynthetic materials that accounts for elastic, plastic, viscous and anisotropic behavior. The incorporation of isotropic-hardening plasticity allows for non-linear stress-strain behavior to be modeled. Anisotropy is provided to account for direction dependency of stiffness (elasticity), yield (plasticity) and creep. The inclusion of creep is provided as an attempt to model ratcheting behavior seen during cyclic loading. This model is calibrated from and compared to several types of uniaxial tension experiments described in the following section. Implicit in this approach is the assumption that the geosynthetic can be treated as a continuum. No attempt has been made to account for the discontinuous nature of these materials with respect to the theories and models used to describe stress-strain behavior. As such, this work should be viewed as an examination of the suitability of continuum-based constitutive models to describe observed geosynthetic stress-strain behavior.

4.3.1 Uniaxial Tension Tests

To calibrate the components of the geosynthetic constitutive model, several types of uniaxial tension tests were performed on the geogrid and geotextile described in Section 3. Manufacturer's properties for each of these materials were listed in Table 3.1.2. For all tension

tests performed, samples were prepared to a minimum length to width ratio of 2.5, with specimen length being approximately 750 mm. This configuration is different from commonly used wide-width specimens and was chosen such that a condition of uniaxial tension, rather than plane strain tension, occurred in the interior portion of the sample. Conditions of uniaxial tension were necessary to calibrate material properties contained in the constitutive models used. Specimens were gripped by gluing the ends of the material between two sheet metal plates. Holes were then drilled in the plates and mounted to a load cross-arm. An electric gear motor was used to provide load for constant rate of deformation tests. For load control tests, a pneumatic actuator was used.

Axial and lateral strain was measured on points interior to the sample in order to avoid lateral restraint effects from the gripped ends. Axial displacement of two points each approximately 250 mm from the ends of the specimen was measured using displacement pots fixed to the load frame and attached to the specimen through slightly tensioned, thin wire cables. The gage length between the two axial displacement points was approximately 250 mm. Lateral strain was calculated in a similar way by measuring lateral displacement for two points directly across from each other in the middle of the specimen. Figure 4.3.1 provides a drawing of the specimen configuration and measurement locations.

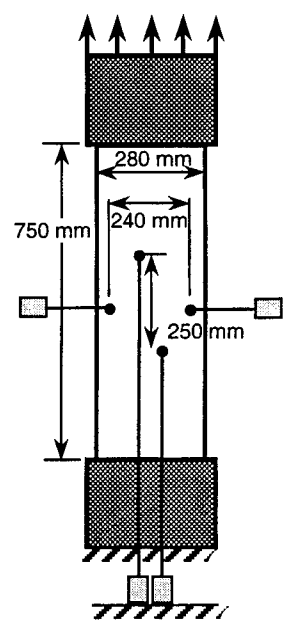

Figure 4.3.1 Schematic of uniaxial tension specimen configuration.

The applied line load on the sample was determined by dividing the uniaxial load by the current width (W_c) of the specimen as determined by

$$W_c = W_i (1 - \varepsilon_l) \tag{4.3.1}$$

where W_i is the initial width of the specimen and ε_l is the lateral strain. The initial width of the geotextile specimens was directly measured, while that for the geogrid was calculated from Equation 4.3.2, which has been derived from ASTM D5262 (1995)

$$W_i = W_m \left(\frac{N}{N-1} \right) \tag{4.3.2}$$

where W_m is the measured width between outside ribs of the sample and N is the number of ribs contained across the sample. Geogrid samples typically contained 8 to 11 ribs depending on whether it was oriented in its machine or cross-machine direction, respectively.

4.3.1.1 Fast Monotonic Tension

The pneumatic actuator was used to apply relatively rapid loads to the geosynthetic specimens oriented in their machine and cross-machine directions. Rate of strain application was on the average of 10 % strain per second. Relatively rapid loads were used to collect load-strain data where creep strains were minor. This data was used to calibrate elastic and plastic material properties, which is more easily done in the absence of creep. Geogrid specimens were taken to rupture. Limitations in the load-transfer mechanism prevented taking the geotextile specimens to rupture. Loads of approximately 75 % of the manufacturer's rated ultimate strength of the geotextile were applied.

4.3.1.2 Creep Tension

Constant load creep tension tests were performed to calibrate creep properties of the geosynthetics. To expedite testing time, tests were performed by applying tensile loads to specimens in stages. Five stages of load were applied to a single specimen with values ranging from 0.16 to 0.8 kN. Relatively light loads were used to calibrate creep parameters for an application where loads in this range were anticipated. Each of the five loads was allowed to remain on the sample for approximately 30 hours prior to the addition of the next load.

4.3.1.3 Slow Monotonic Tension

The electric gear motor was used to apply load at a relatively slow rate of strain. Strain rates of approximately 0.25 % strain per minute were used. Data from these tests was not used for direct calibration of material parameters but was used to assess the ability of the model to account for differences between fast and slow monotonic loading, where modeled differences were due to the development of creep strains during slow loading. Model predictions were made using the actual displacement versus time record from the test being predicted. As with the fast monotonic tension tests, geogrid specimens were taken to rupture while nearly 100 % of the manufacturer's rated ultimate strength was applied to the geotextile.

4.3.1.4 Cyclic Tension: Series I

Cyclic uniaxial tension tests were performed where 12 load cycles were applied at increasing stress amplitudes. The duration of each test ranged from 22 to 27 seconds. Loads for the last load cycle ranged from 60 to 85 % of the manufacturer's rated ultimate strength for the geogrid and 45 % of that for the geotextile. Prediction runs for these tests used the actual load time history from the test being predicted. These tests were performed to allow for the examination of the suitability of the constitutive model for describing one class of cyclic loads.

4.3.1.5 Cyclic Tension: Series II

A second series of cyclic uniaxial tension tests was performed where cycles of load were applied at 12 increasing levels of load amplitude and where multiple cycles were applied at each load amplitude. The number of load cycles applied at each load amplitude ranged from 100 to 700 with the larger number of load cycles applied for the higher levels of load amplitude. Load cycles were applied at a period of approximately 1.8 seconds. For modeling purposes, the actual shape of the load pulse was approximated by a flat-topped triangular shaped pulse and applied at the average pulse frequency observed in the test being predicted. These tests were performed to determine if the addition of creep in the model could predict observed ratcheting behavior.

4.3.2 Constitutive Model Formulation

Components of the constitutive model were formulated within the context of the commercially available finite element (FE) package ABAQUS (Hibbitt et al., 1998) used for the entire

numerical modeling effort. While it is not necessary to formulate and carry out computations within the framework of a finite element model, this was done in order to utilize the constitutive drivers contained within the FE program. Predictions made within the FE program required that an element type and corresponding boundary conditions be selected. A membrane element type (9-node quadratic) with the boundary conditions shown in Figure 4.3.2 was selected. A 4-node quadratic element was also used and shown to produce predictions no different than that with the 9-node element. The 4-noded elements were used later in the analysis of the pavement test facility as these elements were more computationally efficient.

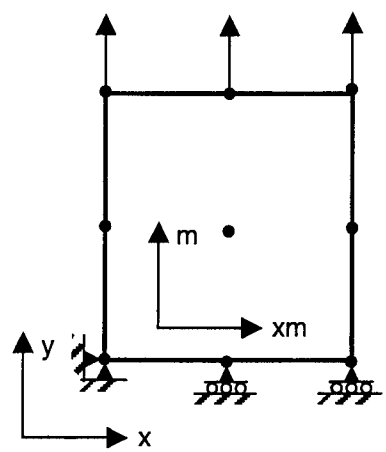

Figure 4.3.2 Boundary conditions for membrane element used in FE analysis.

The membrane element type is formulated to possess in-plane tensile and shear stiffness and strength while containing no resistance to bending or compression. Selection of a membrane element type requires that a thickness of the membrane be selected. A thickness of 1 mm was used for both the geogrid and the geotextile. Experimental values of line load (determined as discussed in Section 4.3.1) were divided by a thickness of 1 mm to obtain experimental values of uniaxial stress for purposes of calibration. Specification of a membrane element also requires input of the membrane section's Poisson's ratio. This Poisson's ratio is used to determine changes in the membrane thickness as load is applied and does not influence in-plane Poisson effects, which are dictated by specified material properties. A default section Poisson's ratio of 0.5 was used, which implies overall incompressible behavior, meaning that the membrane thickness decreased in all cases where uniaxial loads were applied. As described in Section 4.3.3,

results were obtained from FE analyses in such a way as to be comparable to the manner in which results were derived from experiments.

4.3.2.1 Elasticity

Direction dependence of elastic properties were prescribed though the use of a linear, orthotropic elastic constitutive matrix. Orthotroic linear elasticity is described by three moduli (E_{ij}), three independent Poisson's ratios (ν_{ij}), and three shear moduli (G_{ij}), resulting in the elastic constitutive matrix

$$\begin{Bmatrix} \varepsilon_{xm} \\ \varepsilon_{m} \\ \varepsilon_{n} \\ \gamma_{xm-m} \\ \gamma_{xm-n} \\ \gamma_{m-n} \end{Bmatrix} = \begin{bmatrix} 1/E_{xm} & -\nu_{m-xm}/E_m & -\nu_{n-xm}/E_n & 0 & 0 & 0 \\ -\nu_{xm-m}/E_{xm} & 1/E_m & -\nu_{n-m}/E_n & 0 & 0 & 0 \\ -\nu_{xm-n}/E_{xm} & -\nu_{m-n}/E_m & 1/E_n & 0 & 0 & 0 \\ 0 & 0 & 0 & 1/G_{xm-m} & 0 & 0 \\ 0 & 0 & 0 & 0 & 1/G_{xm-n} & 0 \\ 0 & 0 & 0 & 0 & 0 & 1/G_{m-n} \end{bmatrix} \begin{Bmatrix} \sigma_{xm} \\ \sigma_{m} \\ \sigma_{n} \\ \tau_{xm-m} \\ \tau_{xm-n} \\ \tau_{m-n} \end{Bmatrix} \quad (4.3.3)$$

where the subscripts *xm* and *m* denote the in-plane cross-machine and machine directions, and *n* denotes the direction normal to the plane of the geosynthetic. Elastic constants were calibrated from the fast monotonic tension and unloading-reloading portions of the cyclic tension tests. The in-plane elastic parameters (E_{xm}, E_m, $\nu_{xm\text{-}m}$) were determined directly from tests performed in the machine and cross-machine directions of the material. Poisson's ratio in the *m-xm* direction is related to these other constants by the equation

$$\nu_{m-xm} = \nu_{xm-m} \frac{E_m}{E_{xm}} \quad (4.3.4)$$

The in-plane shear modulus ($G_{xm\text{-}m}$) was calibrated from uniaxial tension tests performed on samples of the dimensions shown in Figure 4.3.1 and where the samples were cut in a direction 45° to the machine and cross-machine directions. Measurement of uniaxial tensile stress ($\bar{\sigma}$), uniaxial tensile strain ($\bar{\varepsilon}$), and lateral strain ($\underline{\varepsilon}$) allows for the in-plane shear modulus to be calculated from Equation 4.3.5, which results from a simple stress and strain transformation of the element.

$$G_{xm-m} = \frac{\bar{\sigma}}{2\,(\bar{\varepsilon} - \underline{\varepsilon})} \tag{4.3.5}$$

The measured stresses and strains in Equation 4.3.5 are from the initial portion of the test.

Properties involving the out-of-plane normal direction, n, were selected only to provide for stability of the constitutive matrix and are immaterial with respect to subsequent predictions due to the element type used in the FE analysis for this material. Table 4.3.1 provides a summary of elastic values calibrated for the geogrid and geotextile materials. As can be seen from Table 4.3.1, the geogrid product has significantly greater shear stiffness as compared to the geotextile. The geotextile has an in-plane shear stiffness of essentially zero, however a value of zero is not numerically permissible.

Table 4.3.1 Orthotropic elastic material properties.

Parameter	Geogrid	Geotextile
E_{xm} (kPa)	645,000	960,000
E_m (kPa)	600,000	239,000
E_n (kPa)	1,000,000	1,000,000
$G_{xm\text{-}m} = G_{xm\text{-}n} = G_{m\text{-}n}$ (kPa)	30,000	1.0
$\nu_{xm\text{-}m}$	0.03225	0.5
$\nu_{m\text{-}xm}$	0.03	0.1245
$\nu_{xm\text{-}n} = \nu_{n\text{-}xm} = \nu_{m\text{-}n} = \nu_{n\text{-}m}$	0	0

4.3.2.2 Plasticity

Plasticity was modeled by the use of the Hill yield criterion with isotropic hardening (Lubliner, 1990). The Hill yield criterion allows for the specification of anisotropic yield. An associated flow rule was used. The isotropic hardening rule is specified by providing tabular data of uniaxial yield stress versus plastic strain. Data corresponding to either the machine or cross-machine directions of the geosynthetic can be used. This data was obtained from the fast uniaxial tension tests described in Section 4.3.1, where plastic strain was determined by subtracting elastic strain from the total strain. Figure 4.3.3 illustrates the data used to specify the isotropic hardening rule for the geogrid and geotextile, where this data corresponds to the cross-machine direction of the materials.

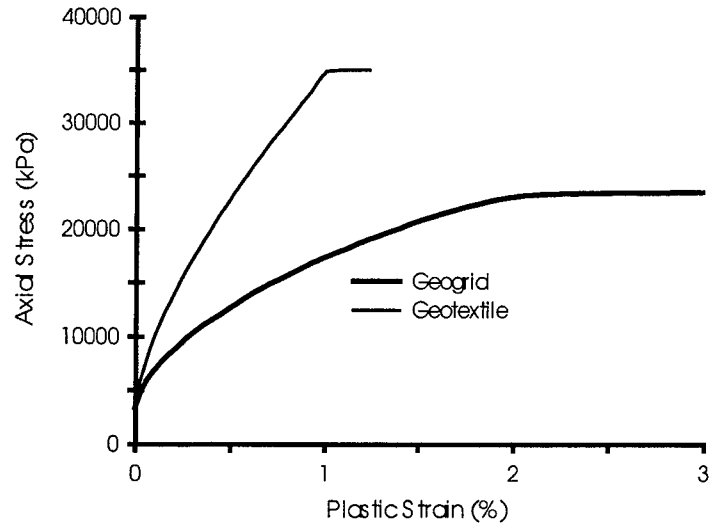

Figure 4.3.3 Tabular data for isotropic hardening rule for the geosynthetics.

Anisotropic yield was specified by the use of Hill's stress function (Hibbitt et al., 1998), which serves to modify the amount of yield that takes place in different directions of the material. These constants are expressed in terms of six yield stress ratios defined as

$$\begin{Bmatrix} R_{xm} \\ R_m \\ R_n \\ R_{xm-m} \\ R_{xm-n} \\ R_{m-n} \end{Bmatrix} = \frac{1}{\sigma^o} \begin{Bmatrix} \bar{\sigma}_{xm} \\ \bar{\sigma}_m \\ \bar{\sigma}_n \\ \sqrt{3}\,\bar{\tau}_{xm-m} \\ \sqrt{3}\,\bar{\tau}_{xm-n} \\ \sqrt{3}\,\bar{\tau}_{m-n} \end{Bmatrix} \tag{4.3.5}$$

where σ^o is a reference yield stress taken to be the tabular data provided for specification of the isotropic hardening rule (which describes yield in the cross-machine direction), and σ_{ij} is the measured yield stress in each respective direction. Table 4.3.2 provides a summary of the yield stress ratios for the geogrid and geotextile products, where it is seen that values of 1 for R_{xm} result from this being the reference direction of the material. Values listed in Table 4.3.2 were

determined by comparing ultimate yield stress values in non-cross machine material directions to that in the cross machine direction from fast monotonic tension tests. As with the elastic properties, yield stress ratios provided for directions involving the out-of-plane direction are immaterial. The values selected for the yield stress ratio $R_{xm\text{-}m}$ reflect the relatively weak in-plane shear strength possessed by both materials, and where this strength for the geotextile is essentially zero. This stress ratio was determined by comparison of results from uniaxial tension tests performed on specimens oriented in a direction 45° to the machine and cross-machine directions to FE results on similarly oriented materials.

Table 4.3.2 Anisotropic yield stress ratios.

Yield Stress Ratio	Geogrid	Geotextile
R_{xm}	1.0	1.0
R_m	0.584	0.74
R_n	0.7	1.0
$R_{xm\text{-}m} = R_{xm\text{-}n} = R_{m\text{-}n}$	0.091	1×10^{-7}

4.3.2.3 Creep

Creep behavior of the geosynthetics was modeled by a strain hardening form of a creep power law (Hibbitt et al., 1998), where the creep strain rate is given by

$$\dot{\varepsilon}^{cr} = \left(A\sigma^n\left[(m+1)\varepsilon^{cr}\right]^m\right)^{\frac{1}{m+1}} \tag{4.3.6}$$

where A, n and m are material constants, σ is the uniaxial tension stress and ε^{cr} is the creep strain in the material. Calibrated values for A, n and m from creep tension tests are listed in Table 4.3.3.

Table 4.3.3 Creep material properties.

Yield Stress Ratio	Geogrid	Geotextile
A	1.0×10^{-8}	1.0×10^{-8}
m	-0.8	-0.8
n	1.22	1.13

Anisotropic creep was specified in a manner similar to that for anisotropic yield. Six creep stress ratios were specified to modify or scale the amount of creep taking place in each material direction. These creep stress ratios are listed in Table 4.3.4.

Table 4.3.4 Anisotropic creep ratios.

Creep Ratio	Geogrid	Geotextile
R_{xm}	1.0	1.0
R_m	0.5	0.55
R_n	0.5	0.5
$R_{xm\text{-}m} = R_{xm\text{-}n} = R_{m\text{-}n}$	0.3	0.3

4.3.3 Results

As noted in the section above, the fast monotonic and creep tests were used for calibration of the model. Predictions of all the tests described in Section 4.3.1 were made using the model described above. In general, displacement or load was applied to the three upper nodes shown in Figure 4.3.2. Figure 4.3.2 shows the material orientation when predictions were made of response in the machine direction of the geosynthetic. The material axes were rotated 90° when predictions were made for the cross-machine direction and rotated 45° when in-plane shear behavior was examined. Predicted axial load was determined by summing the reaction forces for the three bottom nodes and dividing by the current width of the sample. Axial and lateral strain were determined by averaging the three top or three side nodal displacements, respectively, and dividing by the original height and width of the element.

4.3.3.1 Fast Monotonic Tension

Predictions were made of the fast monotonic tension tests with the model containing elastic and plastic material components and not the creep component described by Equation 4.3.6. Since the material was not time-dependent for these analyses, displacement was applied according to an automatic increment scheme. Figures 4.3.4 and 4.3.5 show a comparison of experiments and predictions for the geogrid and geotextile materials oriented in various directions, where both axial (positive strains) and lateral strains (negative strains) are plotted against the applied axial load. For the geogrid, predictions of elastic-plastic response and ultimate strength are well predicted in the machine and cross-machine directions of the material. For response in the 45° direction, the majority of the elastic-plastic response is well predicted. Predictions were forced to produce a greater ultimate strength than that exhibited in the experiments. Ultimate strength in the experiments was accompanied by significant twisting of geogrid ribs that allowed for substantial axial displacements to occur. Given that geogrid materials confined by soil would be

largely prevented from twisting, it was believed that higher ultimate strengths should be modeled in the predictions.

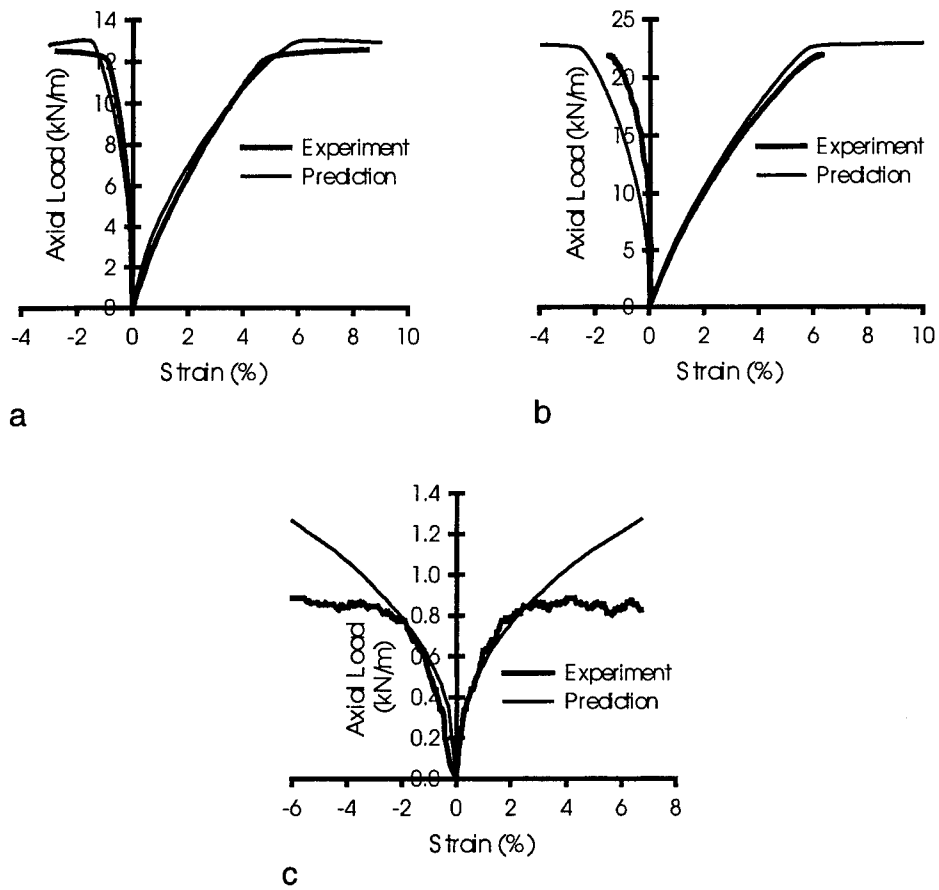

Figure 4.3.4 Experiment and prediction for fast monotonic uniaxial tension for the geogrid in the a) machine, b) cross-machine and c) 45° directions.

For the predictions of the geotextile material shown in Figure 4.3.5, the majority of the load-strain curve for the cross-machine direction is well predicted. Given that experiments were not carried out to failure, ultimate strength in the predictions was selected from manufacturer's data. Load-strain behavior in the machine direction of the geotextile is not predicted particularly well. The experimental curve shows a behavior of increasing secant modulus with increasing strain and is due to removal of the crimp imposed in the material during the manufacturing process. The scaling of the hardening rule as established from results in the cross-machine direction by a anisotropic stress ratio to model behavior in the machine direction prevents exact prediction of this type of behavior. Lateral strain is generally under predicted for the geotextile

material and is due in part to the relatively low Poisson's ratio used. Poisson's ratios as great as 2 were permissible given elasticity stability constraints but produced numerical instabilities in the FE program.

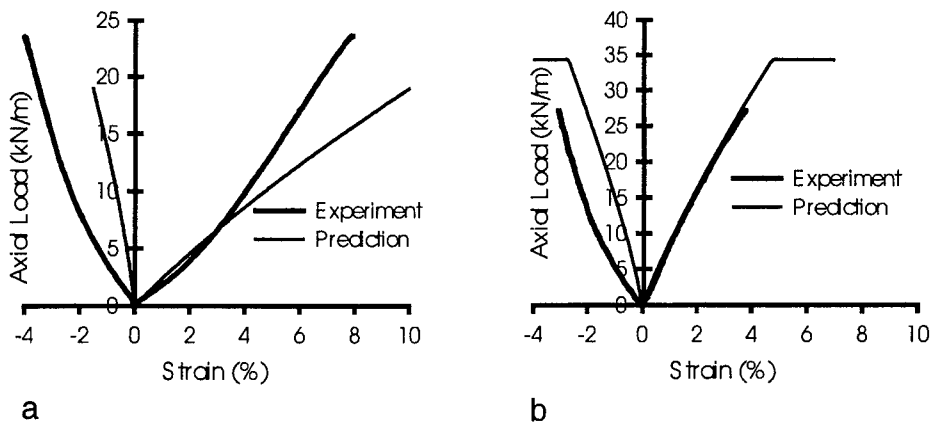

Figure 4.3.5 Experiment and prediction for fast monotonic uniaxial tension for the geotextile in the a) machine and b) cross-machine directions.

4.3.3.2 Creep Tension

Predictions of the creep tension tests are shown in Figures 4.3.6 and 4.3.7 where axial creep strain is plotted against time of the applied load. Creep strain from the experiments was determined by subtracting the instantaneous strain for each load application. Creep strain in the cross-machine direction of the geogrid is very well predicted by the model and is over predicted in the machine direction. Over prediction of creep strain in the machine direction was allowed to better model creep behavior in the slow-monotonic and cyclic tests where results indicated that creep was under predicted, as will be shown later in this section. For the geotextile, predictions are seen to be good for both the machine and cross-machine directions.

4.3.3.3 Slow Monotonic Tension

Figures 4.3.8 and 4.3.9 provide predictions of monotonic tension tests performed at a slow strain rate and where creep was included in the model. Predictions for the geogrid materials are generally very good. For the machine direction, it appears that greater creep strains are needed to model behavior, while from Figure 4.3.6a it is seen that a lower creep rate is required. For the geotextile material in the cross-machine direction, behavior is matched well for low load levels, however strain is under predicted for higher loads. This is in contrast to Figure 4.3.7b where

creep strain is seen to be well-predicted. Response in the machine direction of the geotextile is reasonably well predicted with the exception of lateral strain predictions. The reason for the poor prediction of lateral strain is most likely due to the same reasons for poor predictions of lateral strain seen in the fast-monotonic test series, as described in Section 4.3.3.1.

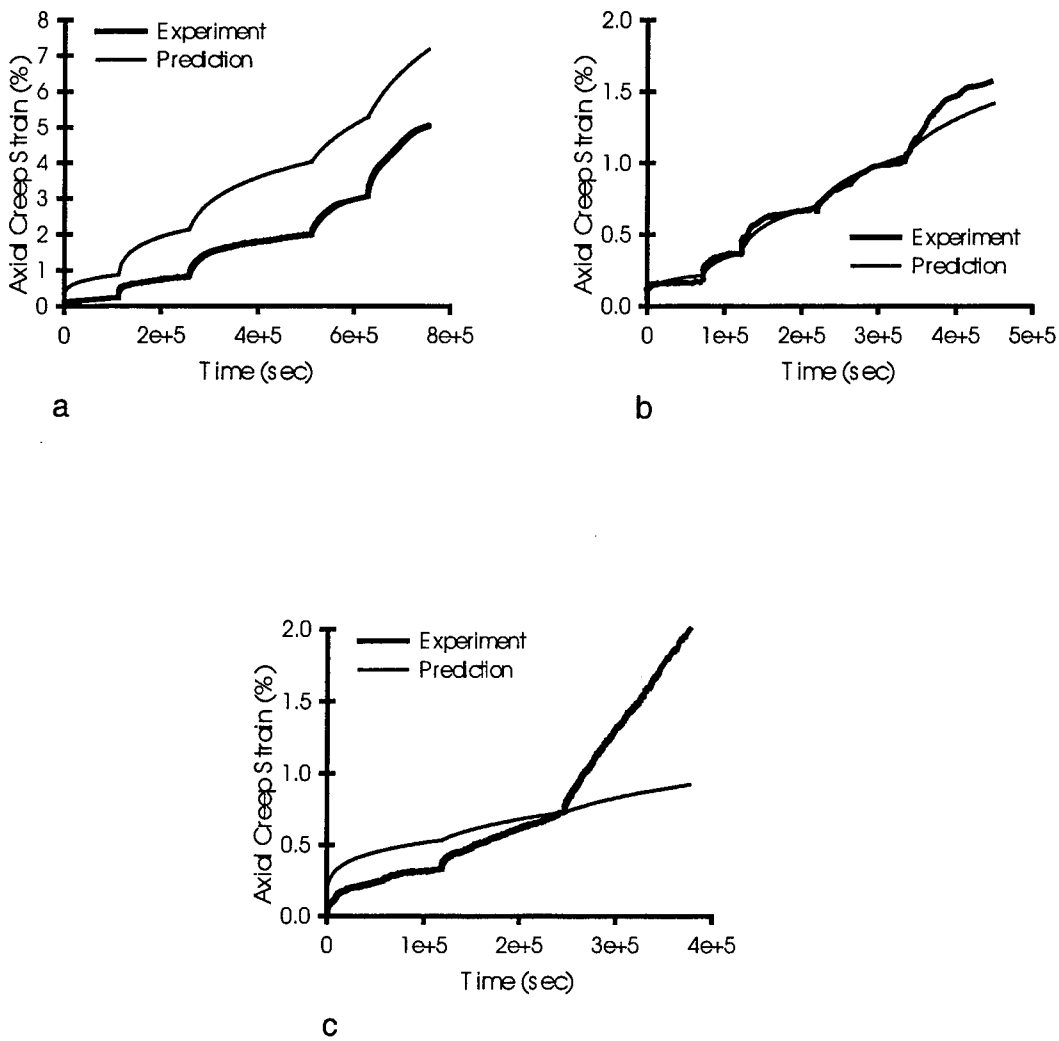

Figure 4.3.6 Experiment and prediction for creep uniaxial tension for the geogrid in the a) machine, b) cross-machine directions and c) 45° directions.

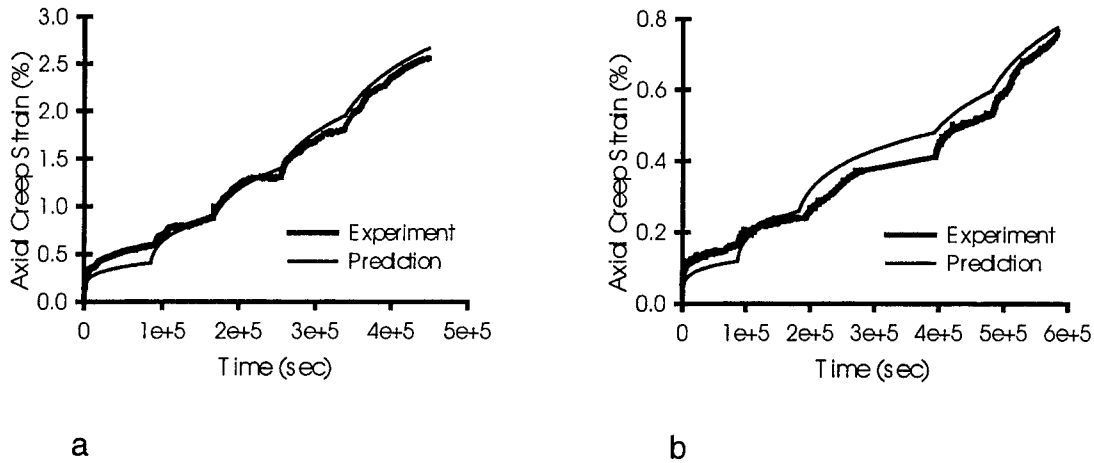

Figure 4.3.7 Experiment and prediction for creep uniaxial tension for the geotextile in the a) machine and b) cross-machine directions.

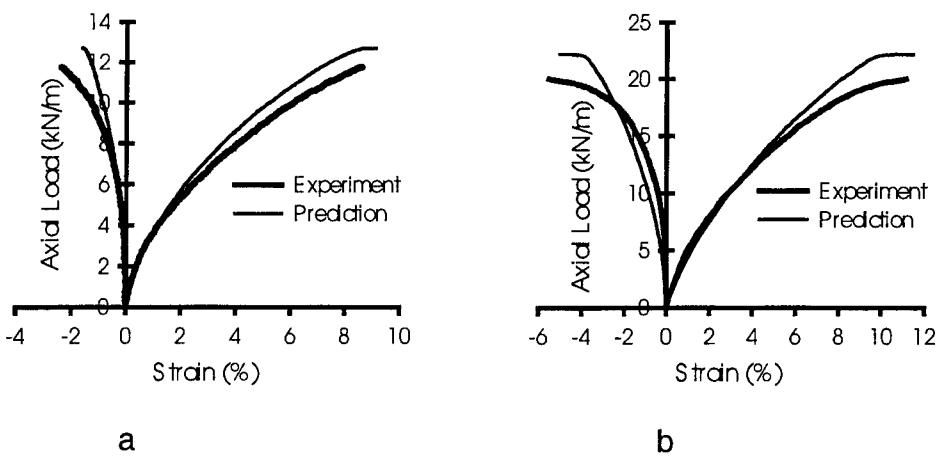

Figure 4.3.8 Experiment and prediction for slow monotonic uniaxial tension for the geogrid in the a) machine and b) cross-machine directions.

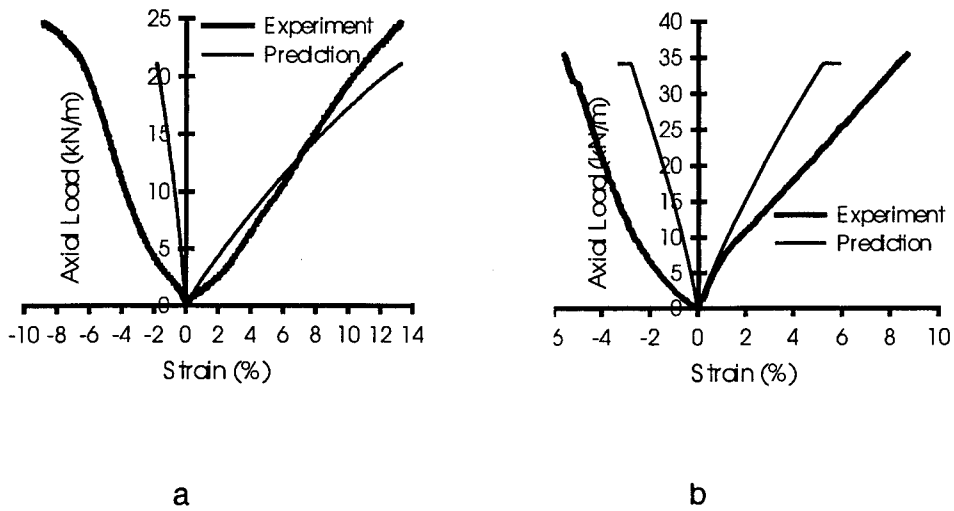

Figure 4.3.9 Experiment and prediction for slow monotonic uniaxial tension for the geotextile in the a) machine and b) cross-machine directions.

4.3.3.4 Cyclic Tension: Series I

Figures 4.3.10 and 4.3.11 illustrate predictions of the series I cyclic tension tests. For the geogrid materials, the loading portion of the curve (the backbone curve) is reasonably well matched. The unloading-reloading behavior does not show, however, the hysteresis seen in the experimental results since the model predicts linear-elastic behavior during unloading and reloading to the previously established yield surface. The relatively stiff, nearly elastic behavior of the geotextile is seen in Figure 4.3.11.

4.3.3.5 Cyclic Tension: Series II

Predictions of multiple cycle tension tests are illustrated in Figures 4.3.12 and 4.3.13. Two sets of curves are provided for each material direction. The upper curves correspond to axial strain at the peak load for the loading cycle plotted, while the bottom two curves correspond to the axial strain at the end of the load cycle when the applied load is zero. Results have been plotted for the first and last load cycle for each load increment. For the geogrid materials, predictions of both maximum and minimum strain are seen to be reasonably good, particularly for the lower load levels. For the geotextile, predictions of maximum strain are reasonably good while minimum

strain is under predicted. An accelerated creep strain rate at higher load levels is most likely needed with the geotextile material in order to provide a better match to the minimum strain response.

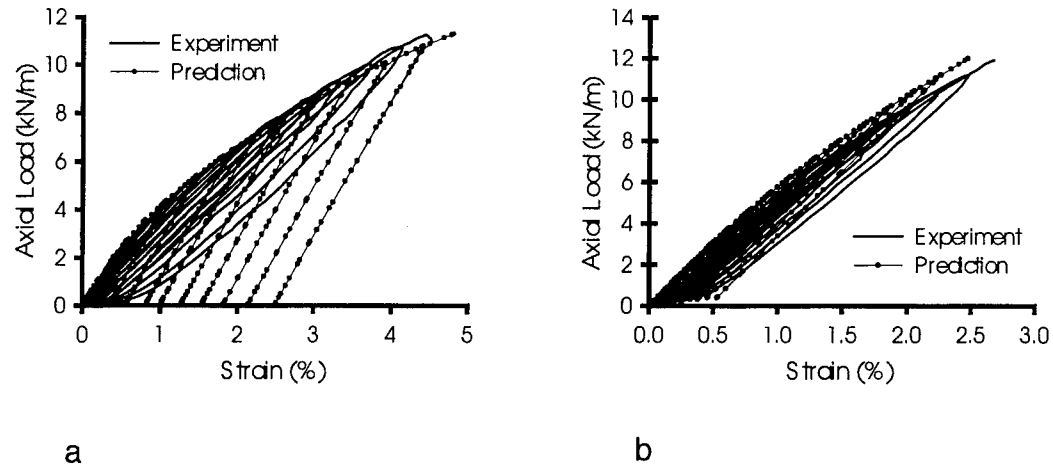

Figure 4.3.10 Experiment and prediction for series I cyclic uniaxial tension for the geogrid in the a) machine and b) cross-machine directions.

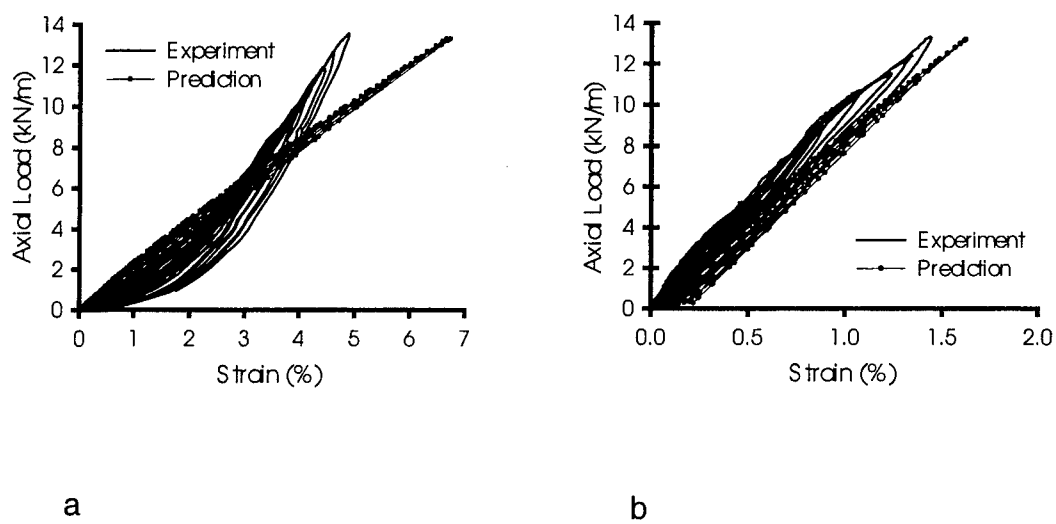

Figure 4.3.11 Experiment and prediction for series I cyclic uniaxial tension for the geotextile in the a) machine and b) cross-machine directions.

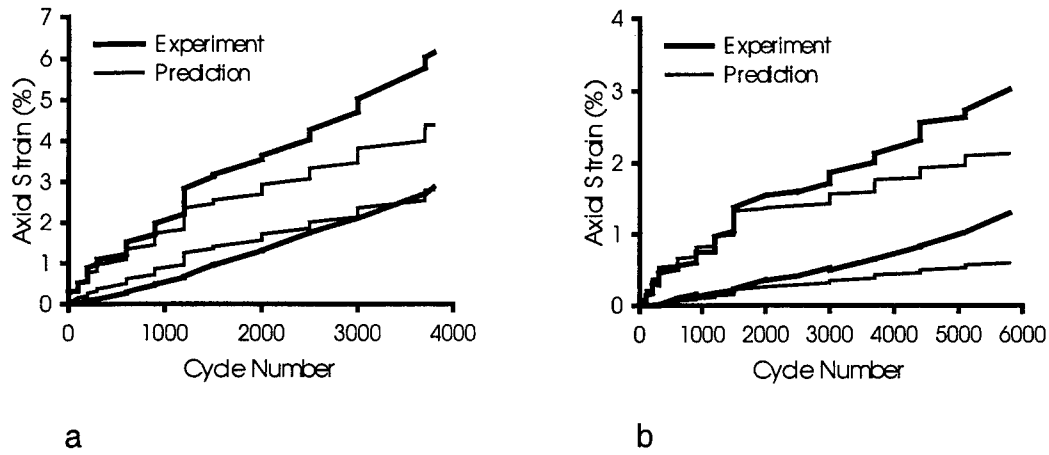

Figure 4.3.12 Experiment and prediction for series II cyclic uniaxial tension for the geogrid in the a) machine and b) cross-machine directions.

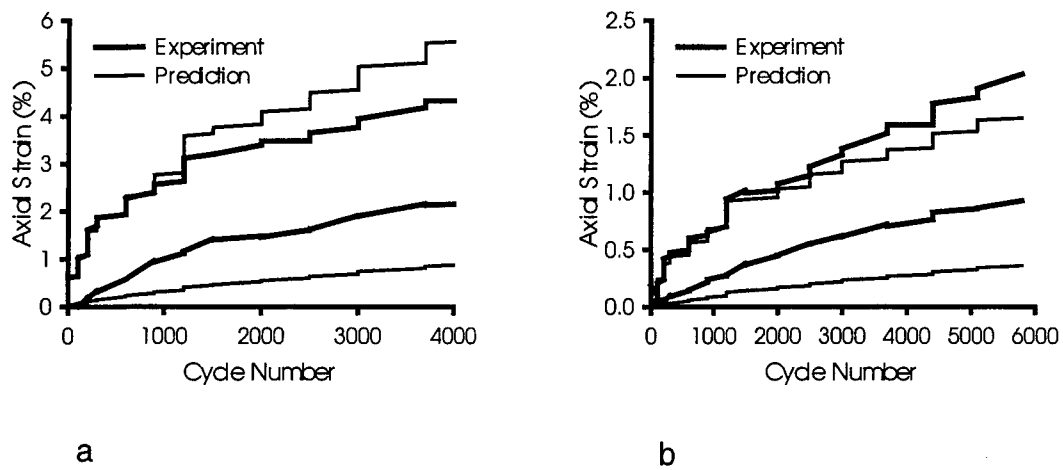

Figure 4.3.13 Experiment and prediction for series II cyclic uniaxial tension for the geotextile in the a) machine and b) cross-machine directions.

4.4 Soil-Geosynthetic Interaction

Pull out tests were conducted to provide a means of calibrating a model used for interaction between the geosynthetics and the base course aggregate. Since the pull out test involves not uniform displacement and strain conditions, the test must be analyzed as a boundary value

problem in order to extract material properties. Two methods were used to analyze the pull out experiment. The first is described in Section 4.4.2 and consists of a simplified numerical solution of the problem. The second involves using the finite element program and material models used in this research for the base aggregate and geosynthetic materials. The first solution provides initial values of parameters that are later updated in the second method.

4.4.1 Pull Out Tests

The pull out apparatus used to generate data to which an interaction model could be compared was built following guidelines established by ASTM (1995). The box is similar in design to that reported by Farrag (1991) and is shown schematically in Figure 4.4.1. The inside dimensions of the box are 1100 mm high, 900 mm wide and 1250 mm long. The box was fabricated from 6.35 mm thick steel plate reinforced by flat steel stiffeners running vertically along the outside of the box's walls.

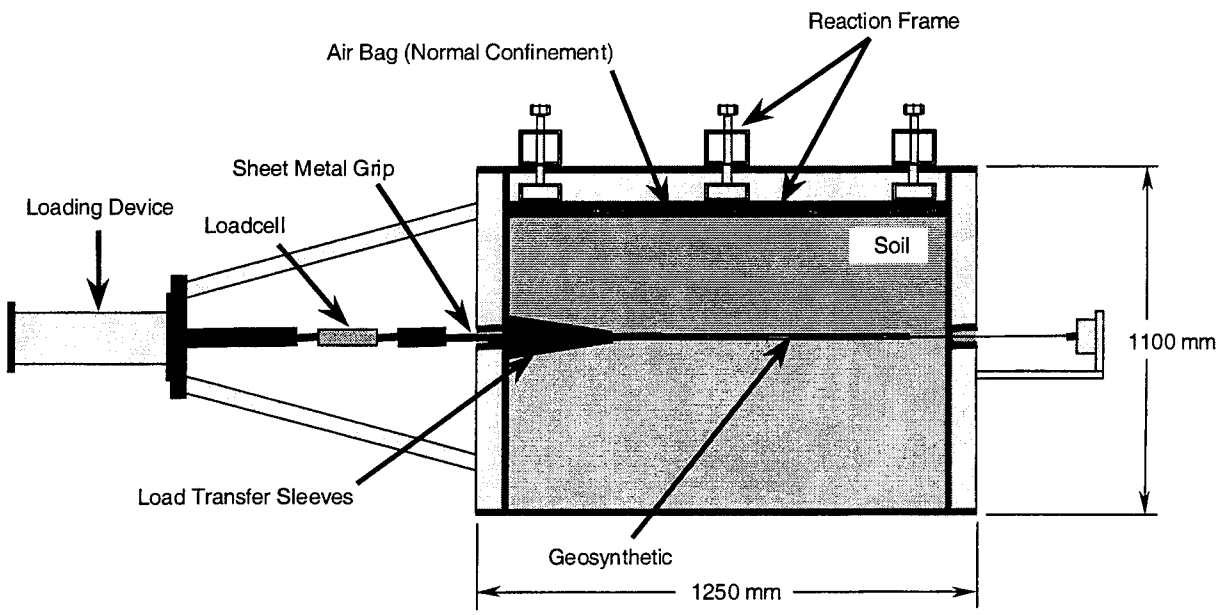

Figure 4.4.1 Schematic drawing of the pull out apparatus.

The gap interface at the front of the box was designed to minimize the development of lateral earth pressure induced by soil movement toward the front wall as geosynthetic pull out progressed. This was accomplished by the use of two sleeves as shown in Figure 4.4.2 that extended into the box. The upper surface of the top sleeve along with the top half of the front wall, the top half of the rear wall and the entire height of the side walls were lined with

lubrication layers to reduce friction as soil moved towards the front wall. A smooth, semi-rigid geomembrane was first attached to these wall surfaces with rivets. Low-adhesion silicone grease was applied on the exposed surface of the geomembrane. A latex rubber membrane was then placed over top of the greased surface prior to soil placement. Vertical normal stress was applied to the top of the soil mass with a flexible bladder fitting the plan area of the pull out box, as seen in Figure 4.4.1. The bladder was controlled by regulated air pressure and could be inflated to a maximum pressure of 200 kPa.

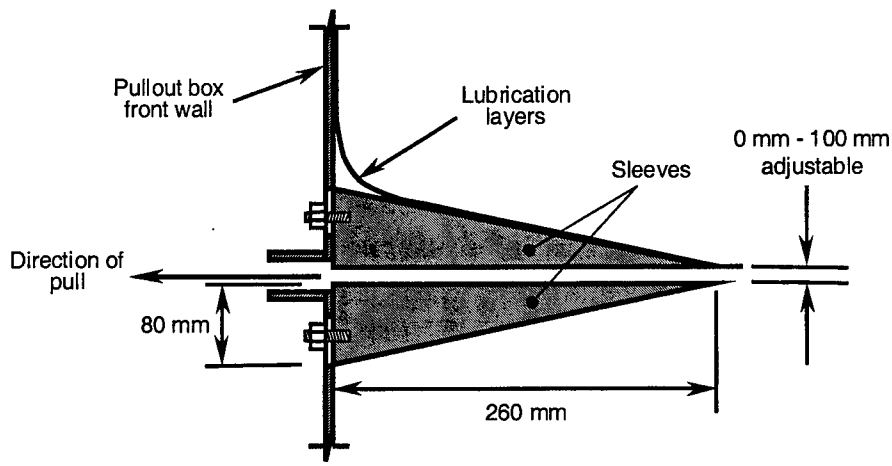

Figure 4.4.2 Sleeves used to form the gap interface at the front of the pull out apparatus.

Figure 4.4.3 shows the arrangement of the geosynthetic sample as placed in the pull out box. The geosynthetic was gripped by gluing it between two sheet metal plates that extended out though the gap in the box. Five extensometers (Celesco Transducer Products, Model PT-101, Canoga Park, CA) were used to monitor displacement along the length of the geosynthetic during pull out. The cables for the extensometers were enclosed in a rigid housing. The ends of the cables were attached to the geogrid at the rib junctions using metal clips. For the geotextile, a low-profile nut and bolt assembly wedged through the weave of the material was used to hold the end of the cable. The length of the geosynthetic samples ranged from 300 mm to 715 mm with the shorter samples being used for the higher confinement pressures.

Pull out force was provided by a screw jack driven by an electric motor that was set at a displacement rate of 1 mm per minute and was measured by a load cell. Prior to conducting a pull out test, the force versus displacement relationship needed to overcome friction between the

sheet metal and the confining soil was determined by conducting pull out tests on the sheet metal alone. These tests were conducted at each of the confining stress levels used in the pull out tests with the results being used to adjust pull out load measurements from tests on the geosynthetics. Pull out tests were conducted at confining stress levels of 5, 15 and 35 kPa.

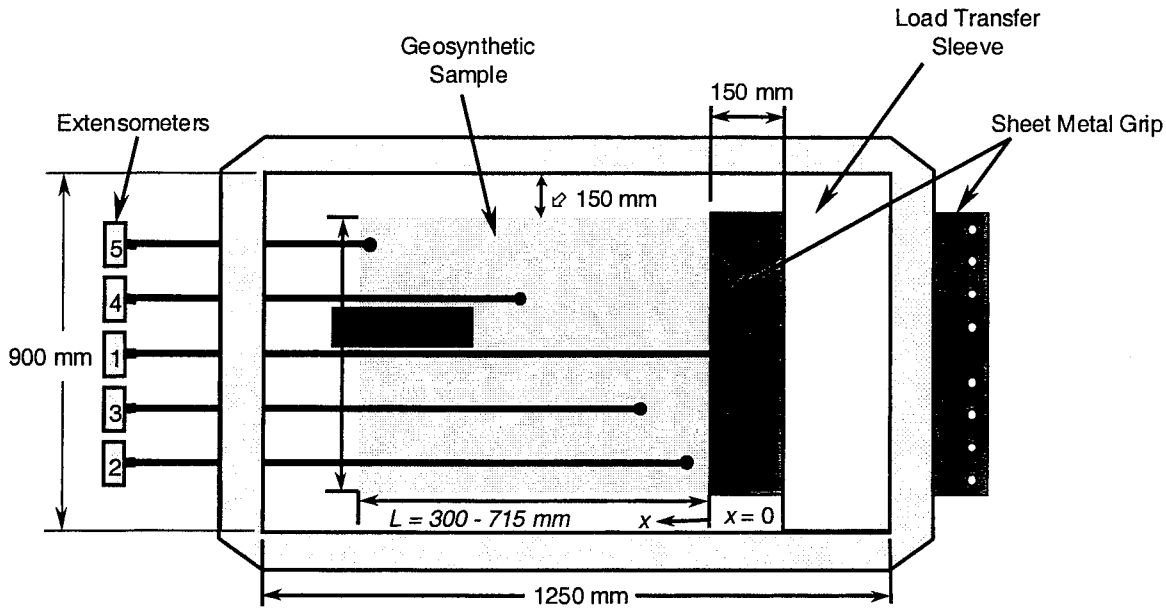

Figure 4.4.3 Plan view of in-soil specimen arrangement.

Geogrid A and Geotextile A were used to conduct the pull out tests. Properties of these materials were summarized in Table 3.1.2. Pull out tests were performed on each material oriented in the machine and cross-machine directions. The base aggregate described in Section 3.1.2 was used as the confining soil. The aggregate was placed in the pull out box at a water content of 5 % and compacted in 30 mm lifts to a dry density of approximately 20.5 kN/m^3, which represented 95 % of the modified Proctor density. A hand-held vibrating plate was used to compact the material. Results from the pull out tests are presented in Section 4.4.2 when compared to the simplified numerical solution.

4.4.2 Determination of Interaction Parameters Via Simplified Numerical Solution

The boundary conditions described for the pull out test preclude the use of a simple calculation for the determination of interaction parameters. A numerical solution was developed to describe the pull out process. Perkins and Cuelho (1999) have described the development of this solution in detail. This solution is a simplified version of that developed through the finite element

method as described in Section 4.4.3 in that a number so simplifying assumptions were made. These assumptions include:

- The surrounding soil was regarded as a stationary rigid body such that absolute movement of the geosynthetic was equivalent to relative movement between the geosynthetic and the soil. This assumption also meant that a material model was not required for the soil.
- A simple, non-linear load-strain relationship was assumed for the geosynthetic. This relationship does not contain the features described in Section 4.3, which are included in the finite element model of the pull out test.

In essence, the simplified model does not contain the complex material descriptions for the soil and geosynthetic described in Sections 4.2 and 4.3.

The expression used to describe the relationship between shear stress (τ) and shear displacement (u) between the geosynthetic and the surrounding soil is given in function form as:

$$\tau = f(u, G_i, \psi_p, \psi_r, \sigma_n) \tag{4.4.1}$$

where G_i is the initial interface shear modulus defined as the initial slope of the shear stress vs. shear displacement curve, ψ_p and ψ_r are the peak and residual friction angles for the interface, and σ_n is the normal stress on the interface. This relationship allows for a non-linear curve of shear stress versus shear displacement to be specified.

This solution was applied for the conditions present in the pull out tests described in Section 4.4.1. The parameters G_i, ψ_p and ψ_r were varied until a reasonable match was achieved between the experiments and the predictions. Figure 4.4.4 shows the shear stress versus shear displacement curves resulting for geogrid A and geotextile A when pulled in their machine and cross-machine directions under normal stress confinements of 5, 15 and 35 kPa. A comparison of the pull out force measured at the front of the geosynthetic versus the pull out displacement at this same point between predictions and experiment is shown in Figure 4.4.5. The values of G_i, ψ_p and ψ_r from this approach were used as starting values for input parameters into the finite element model of the pull out test.

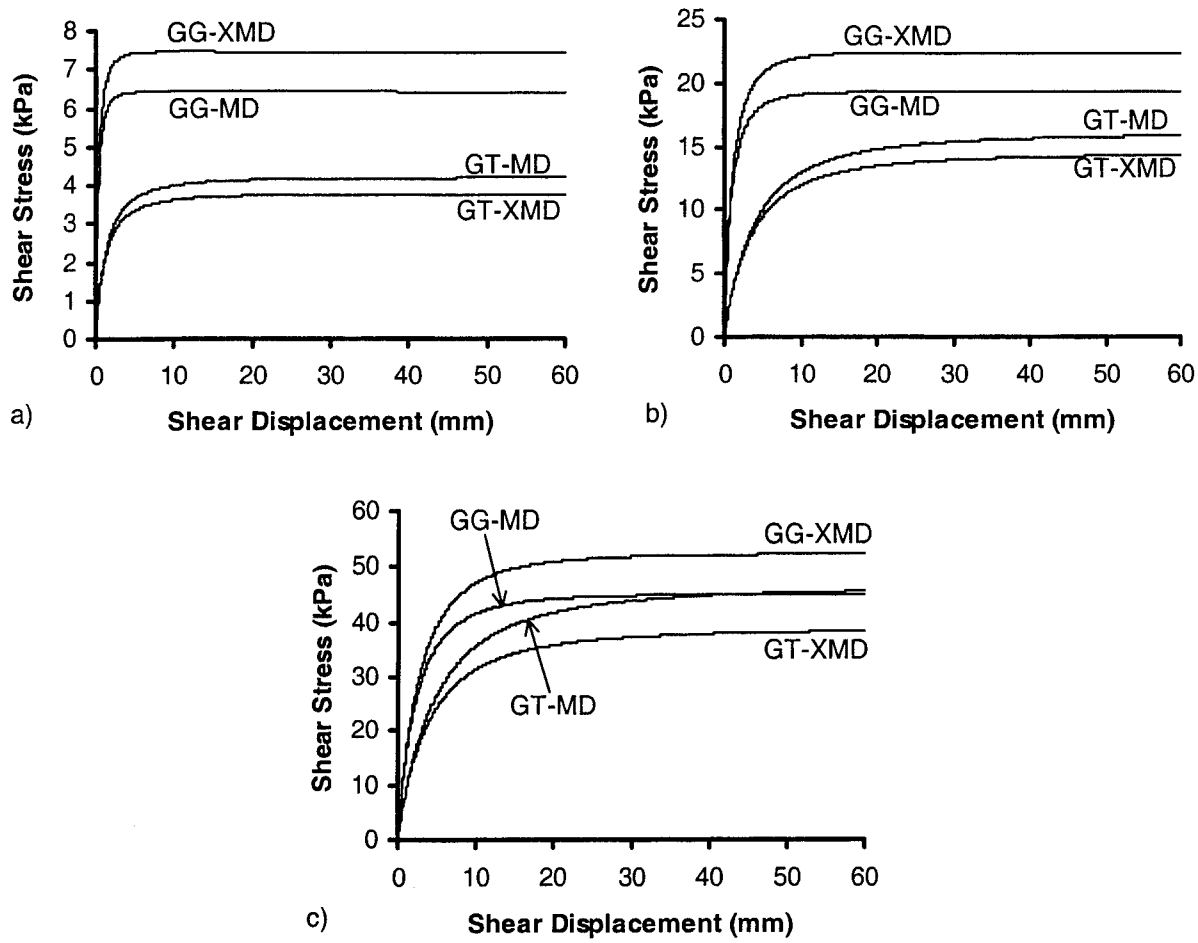

Figure 4.4.4 Shear stress vs. shear displacement relationship for the simplified numerical solution of interaction in the pull out test, a) 5 kPa, b) 15 kPa, c) 35 kPa.

4.4.3 Geosynthetic/Aggregate Interaction Model (GAIM)

The finite element model contained an interaction material model for the interface between the base aggregate layer and the geosynthetic. The model consisted of Coulomb friction model with direction and normal stress dependent friction coefficients (Hibbitt et al. 1998). In its simplest form, the model contains two material properties, a friction coefficient, μ, and a parameter E_{slip}. The model is illustrated with the aid of Figure 4.4.6. Shearing resistance, τ, is a function of the amount of shear displacement, Δ, the latter being the relative displacement between the aggregate layer and the geosynthetic. The initial part of the τ vs. Δ curve is elastic, with the slope of the curve dictated by specification of E_{slip}. Ultimate shearing resistance is reached according to the relationship between τ and σ, which is specified by the friction coefficient, μ. From Figure

4.4.6, it is seen that the shear stiffness of the interface, given by the elastic part of the τ vs. Δ curve, is not constant but increases as normal stress on the interface increases.

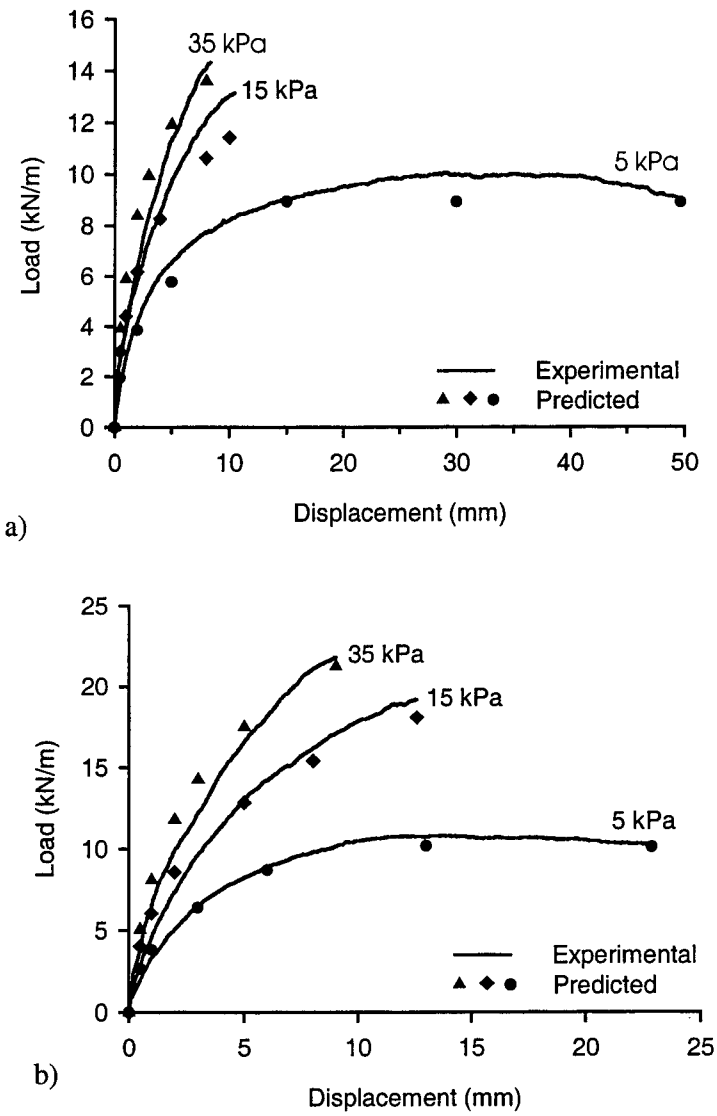

Figure 4.4.5 Experimental and predicted pull out load-displacement curves for a) geogrid A and b) geotextile A.

The friction coefficient can take on different values for the two principal in-plane directions of the contact interface. The friction coefficient can also be specified as a function of normal stress on the interface by listing values of friction coefficient and normal stress

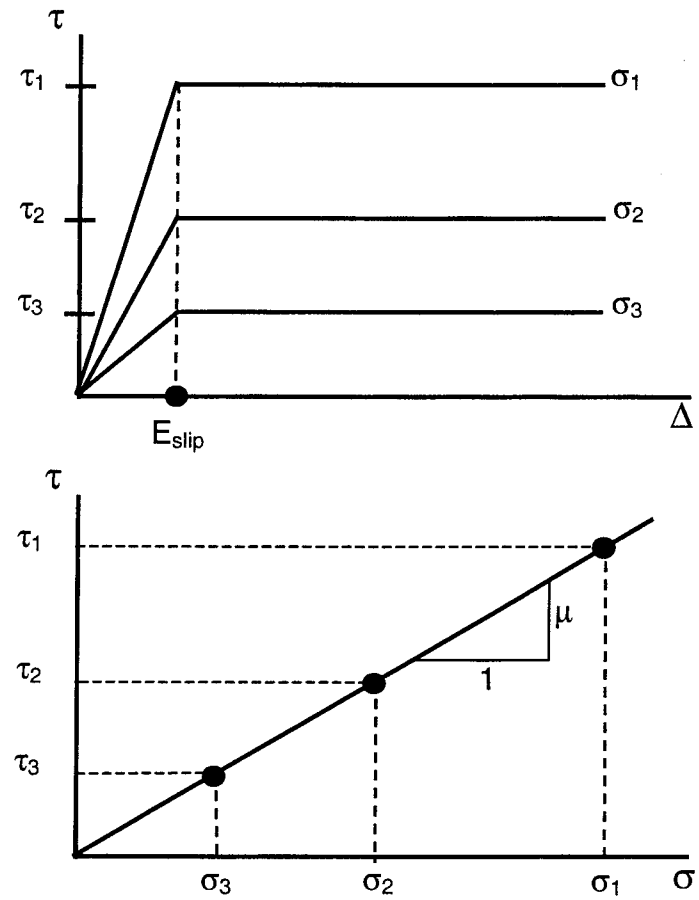

Figure 4.4.6 Geosynthetic/aggregate interaction model.

4.4.4 Calibration of GAIM Via Finite Element Model Simulation of Pull Out Tests

Calibration of the material parameters contained in the Geosynthetic/Aggregate Interaction Model (GAIM) was accomplished by creating a finite element model of the pull out box described in Section 4.4.1. The GAIM described in Section 4.4.3 was used for the contact interfaces between the geosynthetic and the aggregate. Initial values for the material parameters contained in the GAIM were assigned from information obtained from the simplified numerical solution described in Section 4.4.2. Material parameters were then adjusted until predictions from the finite element model matched those from the pull out tests.

The finite element model developed for the pull out box is shown in Figure 4.4.7. Symmetry of the box was recognized such that one-half of the box could be modeled. Three views of the pull out box model are shown. The box top view shows the plan view of the box

looking down on the box, where the centerline of the box is shown. The centerline represents the plane of symmetry for the two box halves. The side of the box corresponding to the centerline had boundary conditions where displacement in the y direction was constrained. Displacement in the x and z directions was unconstrained. The remaining three sides of the box contained boundary conditions corresponding to constraining displacement perpendicular to the face of the box while allowing displacement in the plane of the face. This condition models the lubricated sides used in the pull out box. A uniform mesh size of 12 elements in the x direction and 5 elements in the y direction was created.

The box side view shows the height of the two halves of aggregate above and below the plane containing the geosynthetic. Three elements were contained in the height above the geosynthetic and 4 in the height below. The height of these elements became finer as the plane containing the geosynthetic was approached, as noted in Figure 4.4.7.

The geosynthetic was modeled using 4 noded membrane elements and used the material properties described in Section 4.3. The membrane was placed in a position corresponding to that used in the pull out test being modeled. The width (y dimension) of the geosynthetic was typically 0.3 m. The front edge of the geosynthetic was 0.4 m from the front face of the box. A uniform mesh was used for the geosynthetic. Six elements were contained across the width (y dimension) of the geosynthetic, with 6 to 14 elements contained along the length (x direction) and depending on the length of the geosynthetic. The edge of the geosynthetic along the centerline of the box was constrained from displacement in the y direction. No other boundary conditions were applied to the geosynthetic sheet. Contact interfaces were established above and below the geosynthetic to describe interaction between the geosynthetic and the aggregate.

The base aggregate material model corresponded to that described in Section 4.2. The aggregate was given a density and therefore exerted a self-weight normal pressure on the geosynthetic. Additional normal pressure was applied along the top surface of the upper aggregate layer to produce the desired normal stress (σ) on the surface of the geosynthetic. Displacement was applied to the leading edge of the geosynthetic at a rate of 1 mm per minute. Displacement in the y direction of the leading edge was constrained as this displacement rate was applied in the x direction.

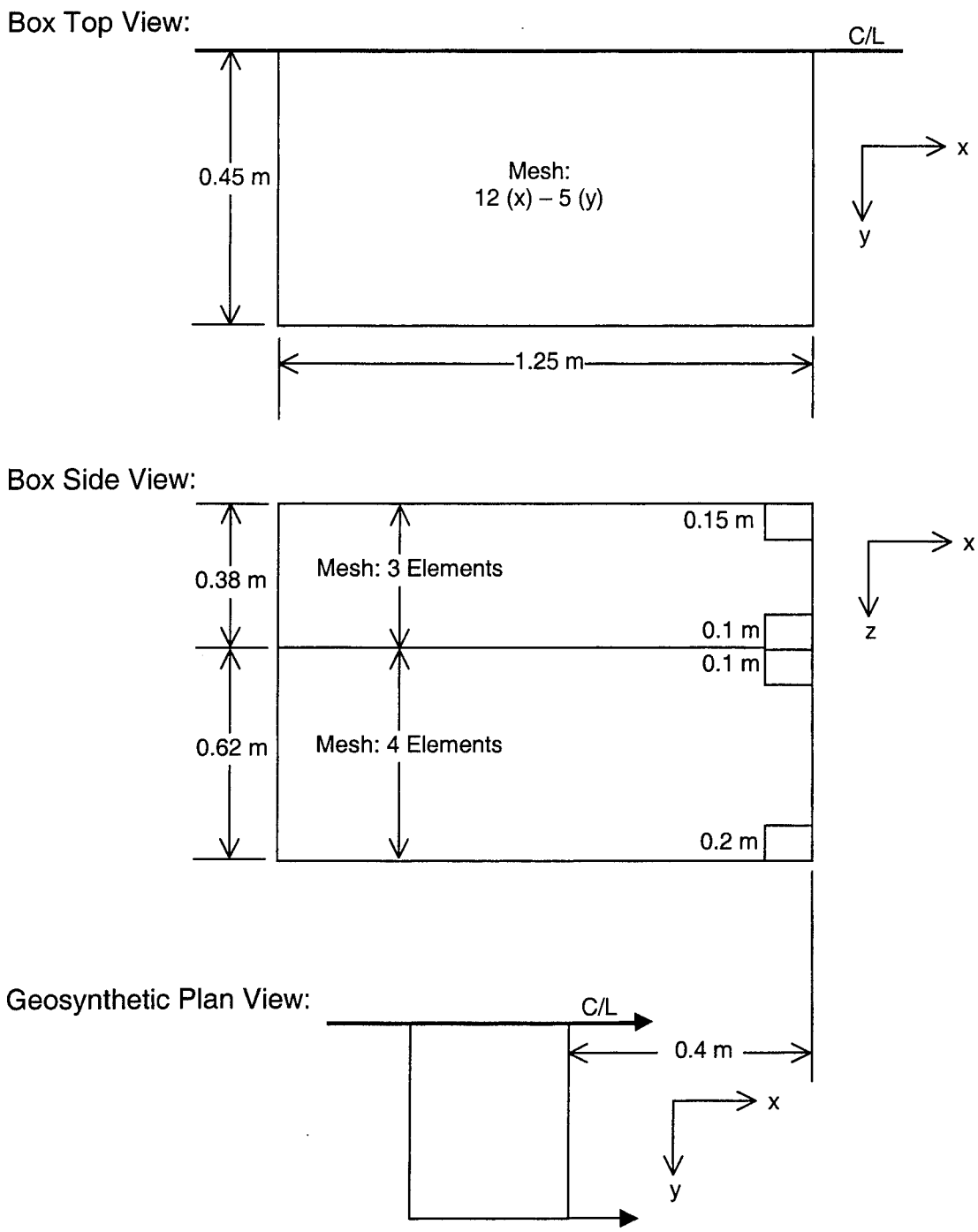

Figure 4.4.7 Finite element model of pull out box.

Reaction forces for the nodes along the leading edge where displacement was applied were summed for a range of displacement values. This allowed the pull out force to be plotted against the pull out displacement. The displacement along the length of the geosynthetic could also be

plotted at different pull out load levels. Adjustment of the GAIM parameters to provide a match between finite element model predictions and pull out test results yielded the parameters summarized in Table 4.4.1 for Geogrid A and the Geotextile. Direction dependency of the friction coefficient (μ) was used for both geosynthetics. Normal stress (σ) dependency on the friction coefficient was used for the geotextile.

Table 4.4.1 GAIM material parameters.

		μ		
	σ (kPa)	M	XM	Eslip (m)
Geogrid A	5	1.376	1.570	0.001
	15	1.376	1.570	
	35	1.376	1.570	
Geotextile	5	0.840	0.750	0.001
	15	1.050	1.020	
	35	1.270	1.150	

Results from the finite element model are compared to the pull out test results in Figures 4.4.8 – 4.4.19 where it is seen that generally good agreement is seen between predictions and test results. Figure 4.4.20 shows an example from one pull out test of the development of displacement at different load levels during the test. In this figure, displacement at various positions along the length of the geosynthetic is plotted for six different load levels.

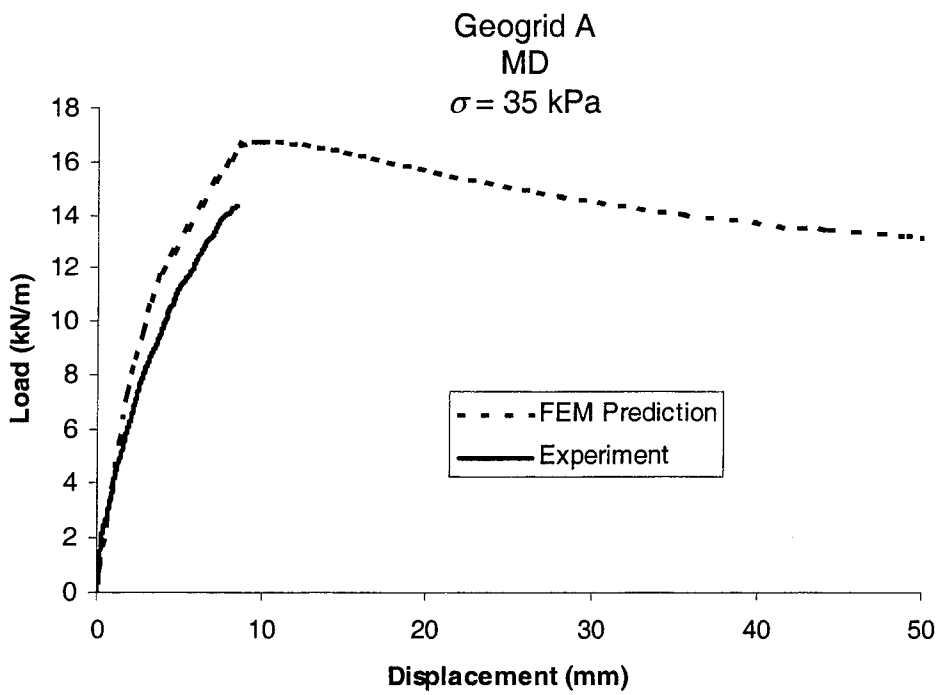

Figure 4.4.8 FEM and pull out test results for Geogrid A, MD, $\sigma = 35$ kPa.

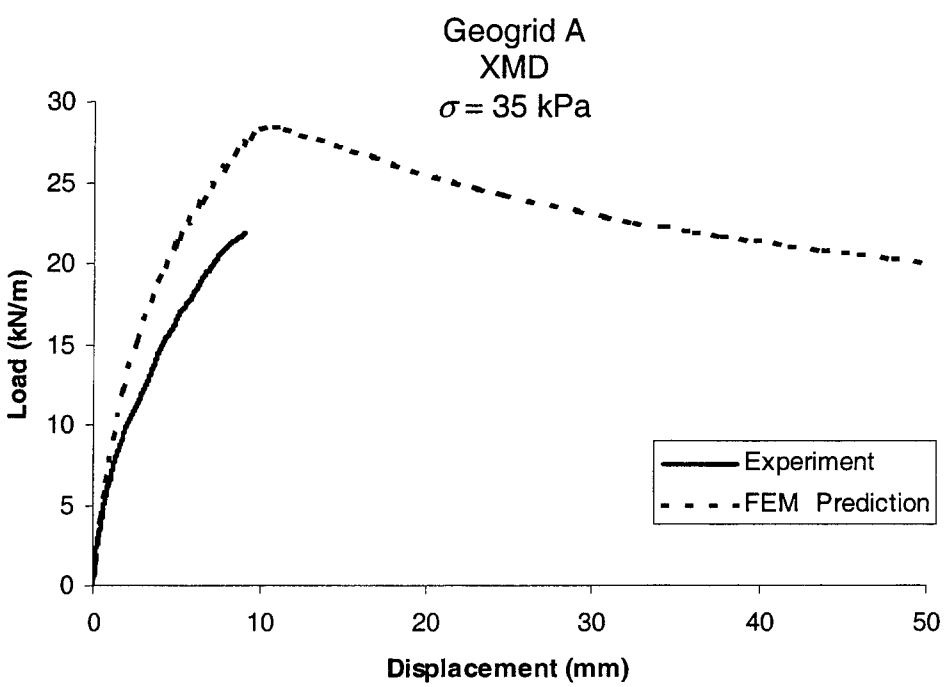

Figure 4.4.9 FEM and pull out test results for Geogrid A, XMD, $\sigma = 35$ kPa.

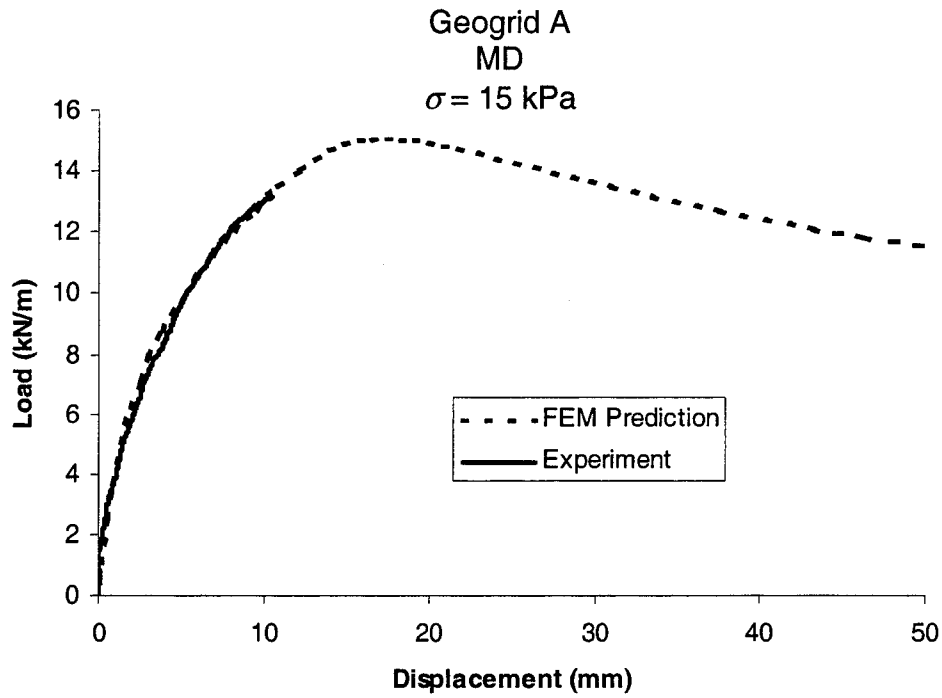

Figure 4.4.10 FEM and pull out test results for Geogrid A, MD, σ = 15 kPa.

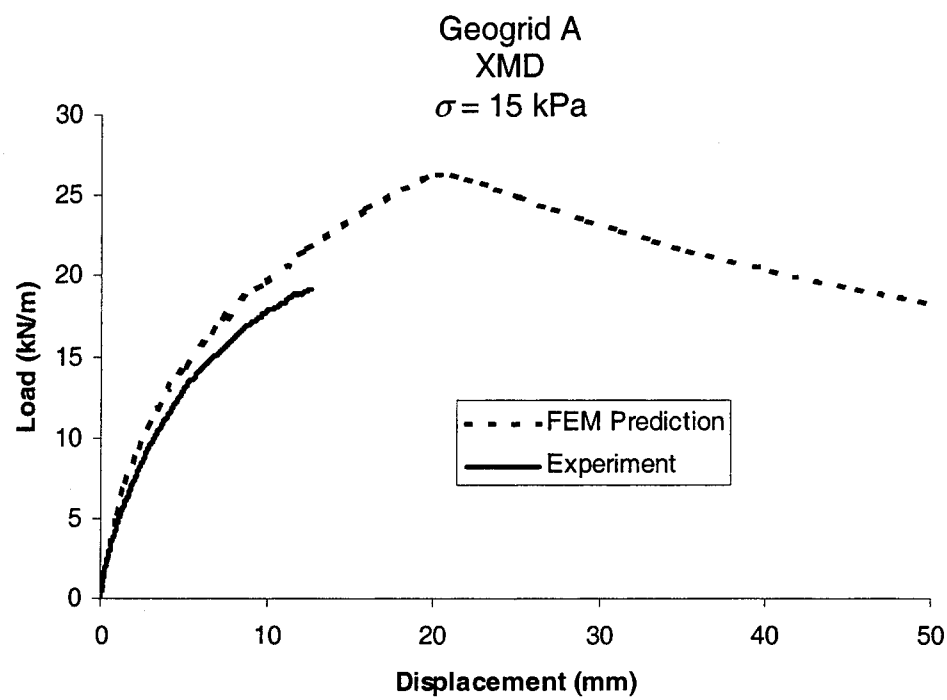

Figure 4.4.11 FEM and pull out test results for Geogrid A, XMD, σ = 15 kPa.

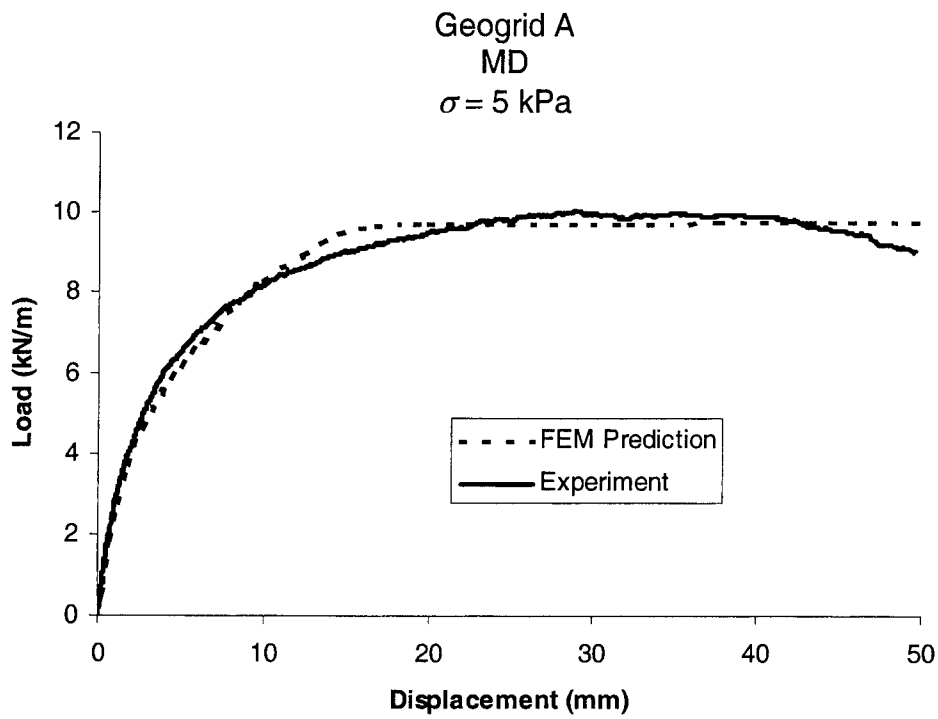

Figure 4.4.12 FEM and pull out test results for Geogrid A, MD, $\sigma = 5$ kPa.

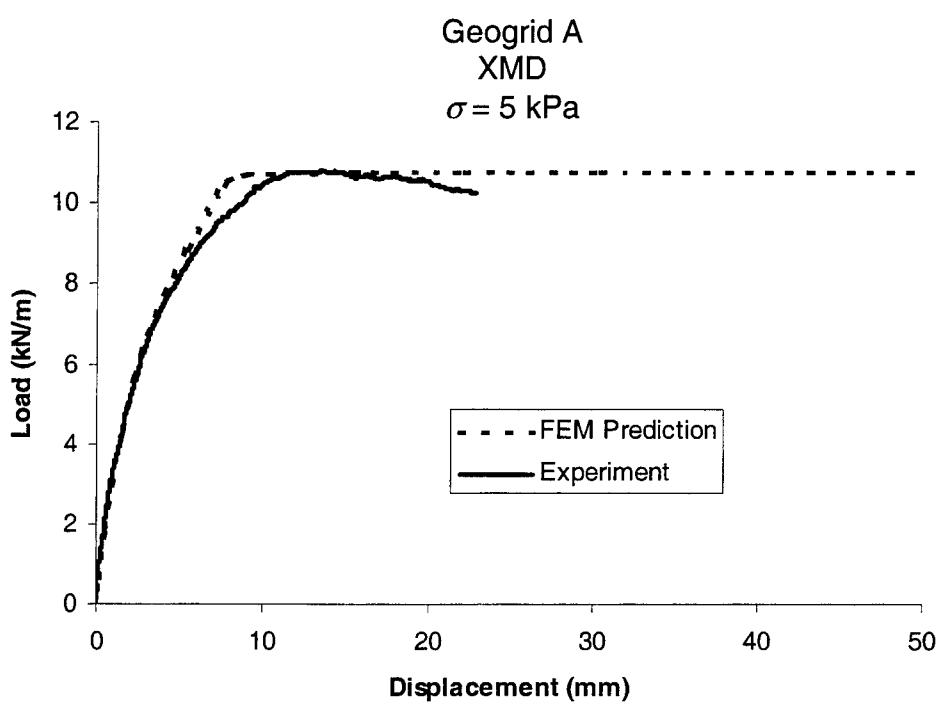

Figure 4.4.13 FEM and pull out test results for Geogrid A, XMD, $\sigma = 5$ kPa.

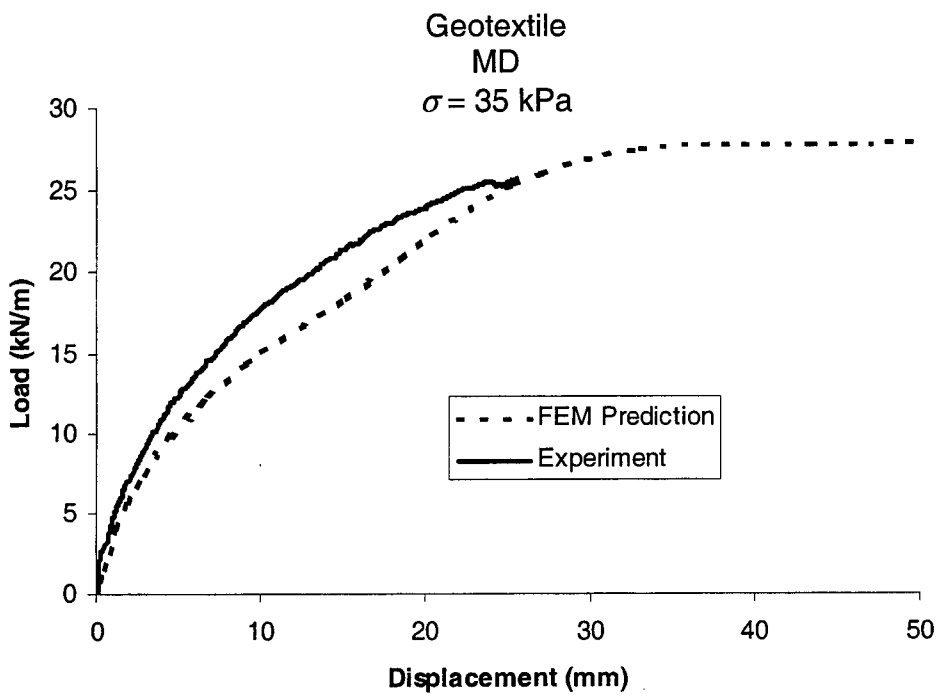

Figure 4.4.14 FEM and pull out test results for Geotextile, MD, $\sigma = 35$ kPa.

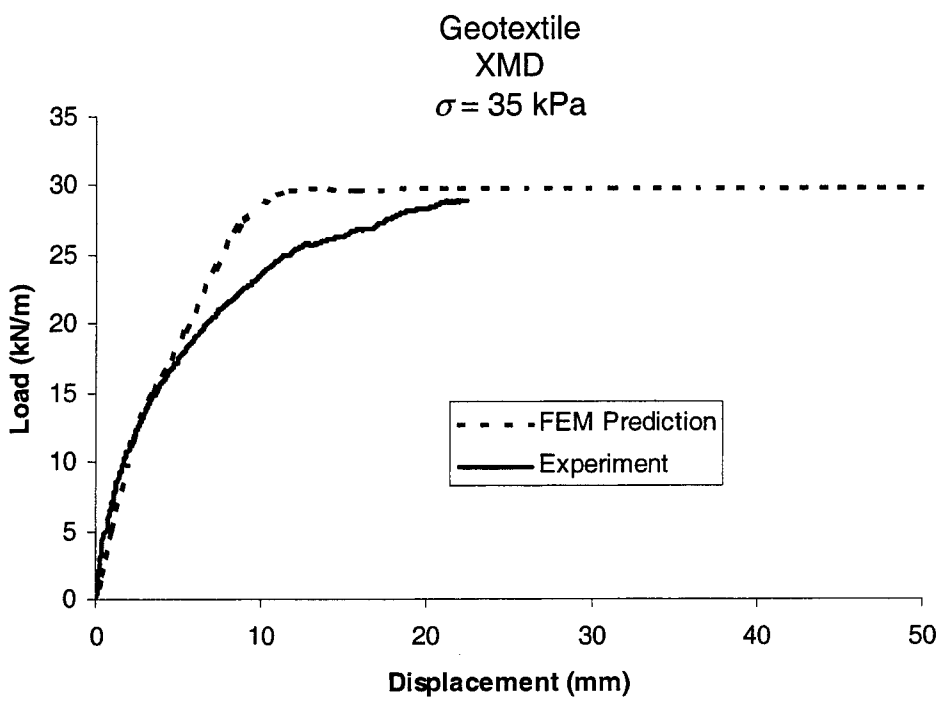

Figure 4.4.15 FEM and pull out test results for Geotextile, XMD, $\sigma = 35$ kPa.

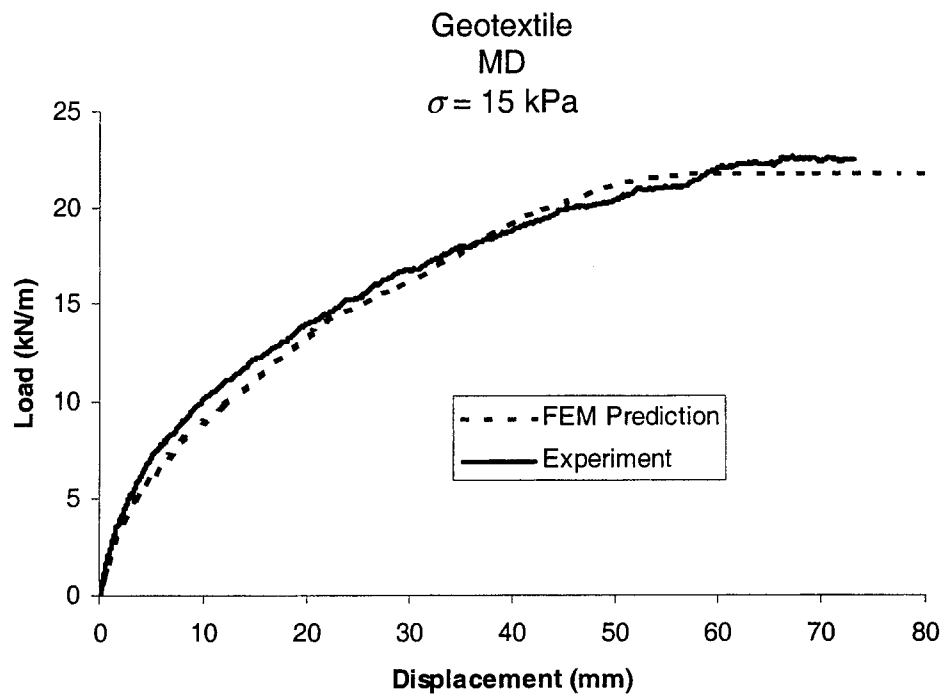

Figure 4.4.16 FEM and pull out test results for Geotextile, MD, $\sigma = 15$ kPa.

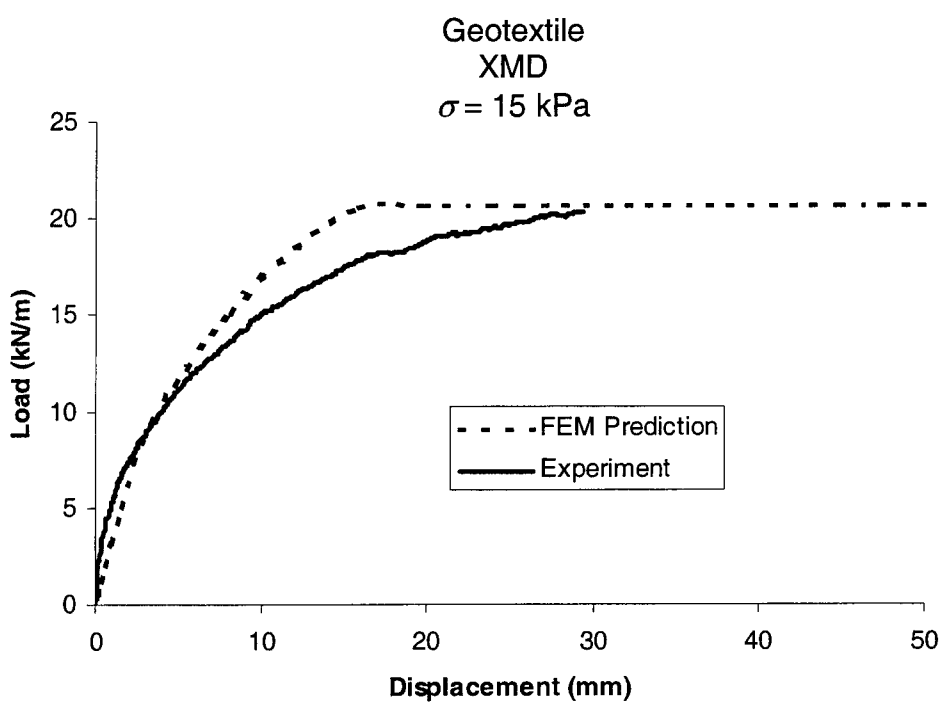

Figure 4.4.17 FEM and pull out test results for Geotextile, XMD, $\sigma = 15$ kPa.

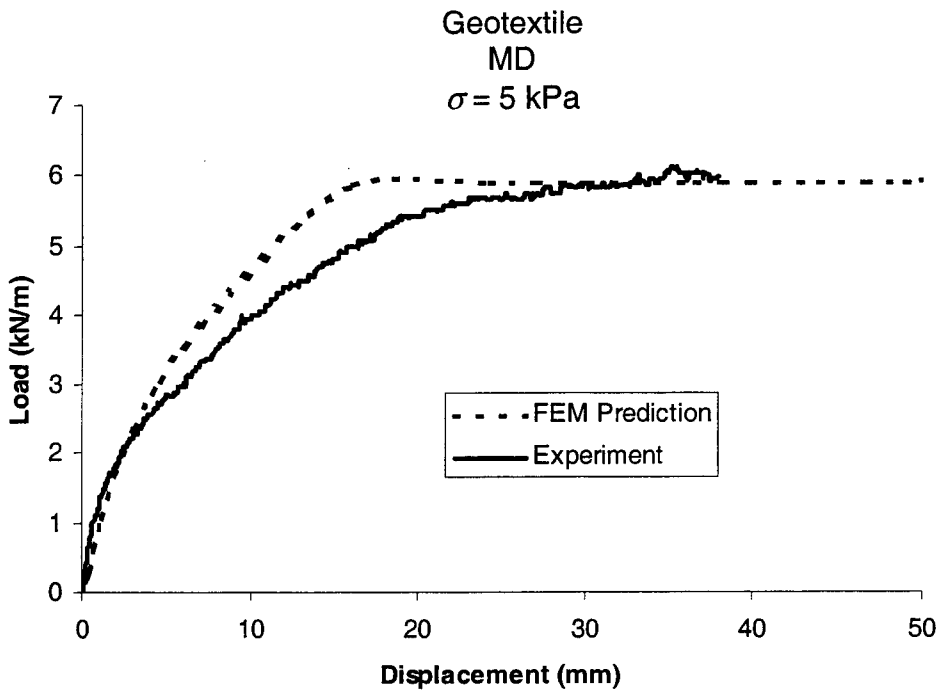

Figure 4.4.18 FEM and pull out test results for Geotextile, MD, $\sigma = 5$ kPa.

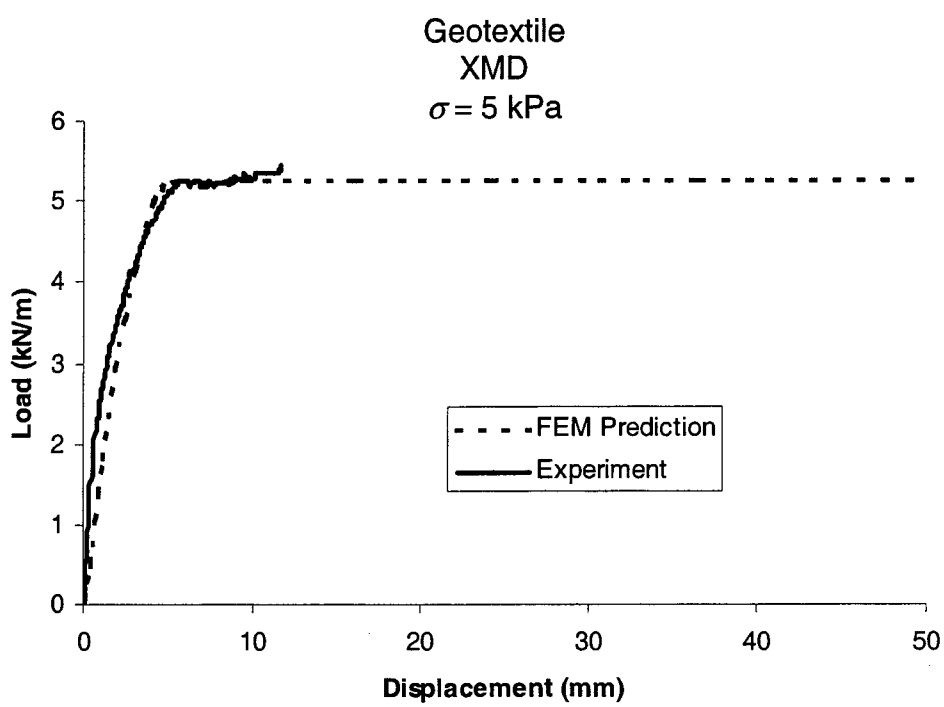

Figure 4.4.19 FEM and pull out test results for Geotextile, XMD, $\sigma = 5$ kPa.

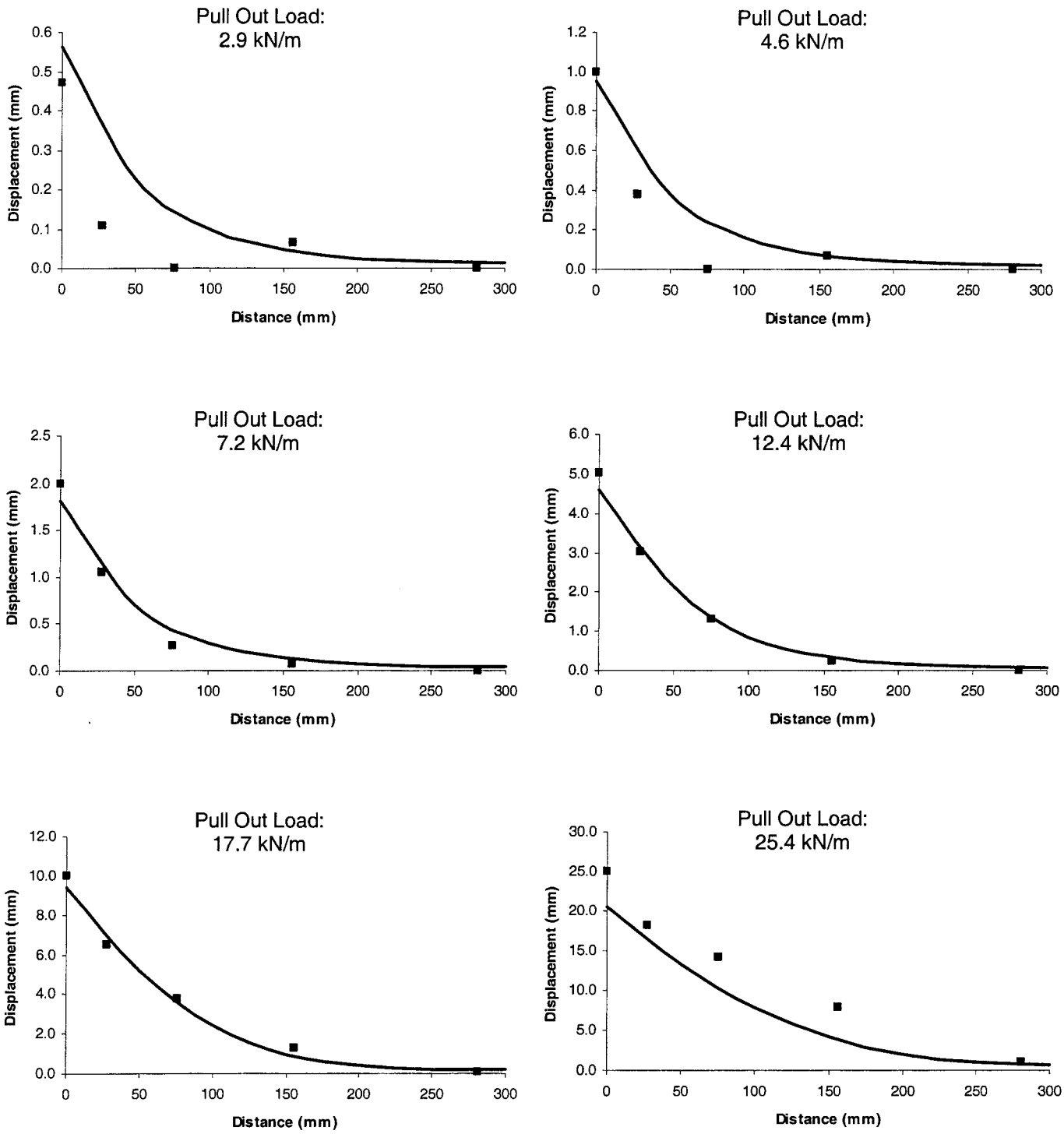

Figure 4.4.20 FEM and pull out test displacement results at various load levels for Geotextile, MD, $\sigma = 35$ kPa.

5.0 PAVEMENT TEST FACILITY FINITE ELEMENT MODEL

A finite element model was created to simulate the pavement layer thicknesses, boundary conditions and loading present in the pavement test sections described in Section 3. All modeling was done using the commercial program ABAQUS (Hibbitt et al. 1998). Three types of models were created. The first is a model of pavement test sections without reinforcement and is described in Section 5.1. The second is a model where reinforcement is described in such a way that it represents the maximum amount of reinforcement benefit that could be expected with a "perfect" reinforcement product. This model was created to provide a means of comparison to the 3rd type of model where the geosynthetic reinforcement layer was explicitly included. Since effects of the reinforcement are ultimately expressed in terms of prevention of lateral movement of the base aggregate at the level of the geosynthetic, perfect reinforcement is simulated by modifying the unreinforced model by preventing all in-plane or lateral motions of the base aggregate element nodes at the level of the geosynthetic. This in effect simulates reinforcement with an infinitely stiff geosynthetic and an infinitely stiff contact shear interface between the geosynthetic and the aggregate. This model is described in Section 5.2. The third type of model created is one where a separate material layer corresponding to the geosynthetic is added to the unreinforced model and is described in Section 5.3.

5.1 Unreinforced FE Model

The finite element model of unreinforced pavements is a 3-dimensional model created to match the conditions for the pavement test sections described in Section 3. A two-dimensional axi-symmetric model was not used because of the potential influence of the box's square corners and for the later inclusion of a layer of geosynthetic reinforcement that has direction dependent material properties. Symmetry of the box was recognized such that a model of one-quarter of the box was created. Figure 5.1.1 illustrates the geometry and boundary conditions used for the development of the model. Actual layer thicknesses for the AC and base aggregate correspond to the test section being modeled and were given in Tables 3.1.3-3.1.5.

The width in the x and y directions of the ¼ box modeled was 1 m. The pavement load was applied as a uniform pressure equal to the values given in Table 3.1.6 for each test section over one-quarter of a circular plate having a radius of 152 mm. The time history of the pavement load was applied to approximate the curve given in Figure 3.1.2. For several models, the load plate

and rubber pad were modeled using additional material elements. For these cases, the load plate and rubber pad were modeled by plates having a radius of 152 mm. The load plate had a thickness of 25 mm and was given isotropic elastic properties with a Young's modulus of 2×10^8 kPa and a Poisson's ratio of 0.33. The rubber pad had a thickness of 4 mm and was also given elastic properties with a Young's modulus of 400 kPa and a Poisson's ratio of 0.

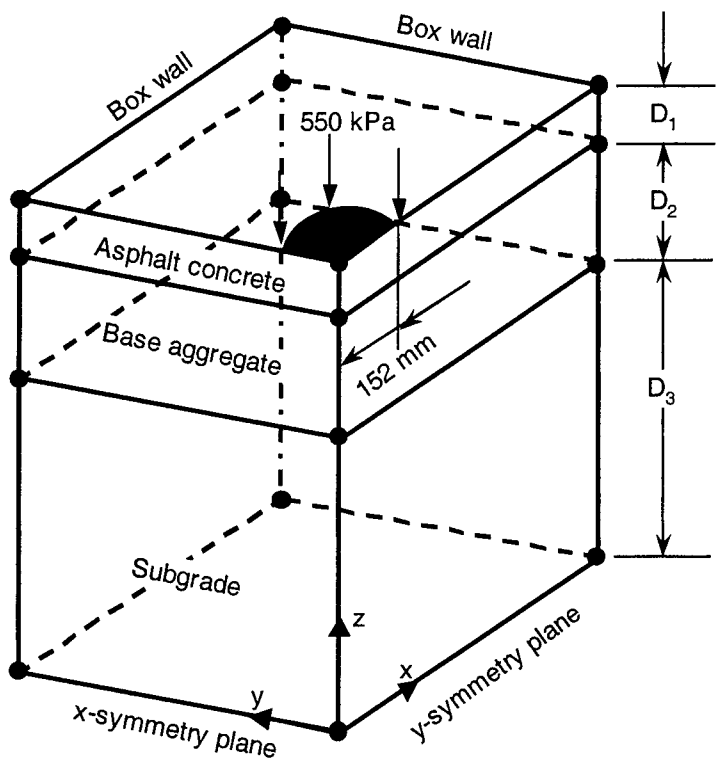

Figure 5.1.1 Finite element model of unreinforced pavement test sections.

The vertical edge directly beneath the load plate centerline was a symmetry line and was therefore constrained from motion in the *x* and *y* dimensions and free from constraints in the *z* direction. The four faces of the box were constrained in a direction perpendicular to the box face and in the second horizontal direction parallel to the box wall, and otherwise free of constraint in the *z* direction. The nodes along the perimeter of the asphalt concrete layer directly adjacent to the box walls were free of all constraints such that the nodes were free to move in from the box wall as pavement load was applied. This boundary condition removed an artificial attachment of the asphalt concrete to the walls of the box and thereby prevented tensile loads from developing in the asphalt concrete. The symmetry planes of the model were unconstrained in the z direction

and in the horizontal direction parallel to the plane. Motion in the horizontal direction perpendicular to the plane was constrained.

Eight-noded hexagonal solid elements were used for all material layers. Approximately 42 elements were used for each of the load plate and rubber pad while 230, 570 and 1710 elements were used for the asphalt concrete, base aggregate and subgrade layers, respectively. The nodes between the material layers were equivalenced and therefore connected.

5.2 Perfect Reinforced FE Model

A FE model was created where the reinforcement was modeled in such a way as to provide for the maximum effect on pavement performance. Within the context of the material and finite element models developed for this project, the principal effect of reinforcement on the performance of the pavement is the prevention of lateral strain or displacement of the base aggregate at the interface with the geosynthetic. Maximum effect of a reinforcement layer could thereby be simulated by preventing all lateral motion of the base course aggregate at the level where it would be in contact with the geosynthetic. This was accomplished by modifying the unreinforced model described in Section 5.1 by prescribing boundary conditions to the nodes at the bottom of the base aggregate, where these boundary conditions prevented all x and y motion of the nodes. For these models, the simulated reinforcement effectively has an infinite tensile stiffness and an infinitely stiff contact interface with the base aggregate.

5.3 Geosynthetic Reinforced FE Model

A third type of finite element model was created where a sheet of geosynthetic reinforcement was included as part of the pavement cross-section. The geosynthetic was modeled by 4 noded membrane elements that have the property of containing tensile load carrying capacity, but have no resistance in bending or compression. Membrane elements are two-dimensional elements that are commonly used for describing flexible sheets having tensile load carrying capacity. The material model described in Section 4.3 was used for the geosynthetic. In all cases, the geosynthetic was placed between the base aggregate and the subgrade. The contact interface model described in Section 4.4 was used between the base course aggregate and the geosynthetic.

6.0 FINITE ELEMENT MODELING RESULTS

6.1 Unreinforced Pavements

FE models were created to match conditions in unreinforced test sections described in Section 3. Layer thicknesses, density and void ratio for the materials used in test sections SSS1, SSS4, CS2, CS8 and CS9 were modeled. Table 6.1.1 provides a summary of the properties used for the AC layer for each test section. Material model parameters for the bounding surface plasticity model used for the clay and silty sand subgrade and the base aggregate were listed in Table 4.2.2.

Table 6.1.1 Material parameter values used for the AC of unreinforced test sections.

Parameter	SSS1	SSS4	CS2	CS8	CS9
E_x (MPa)	3150	3400	3920	2980	1710
E_y (MPa)	3150	3400	3920	2980	1710
E_z (MPa)	3150	3400	3920	2980	1710
G_{xy} (MPa)	1167	1259	1219	1103	633
G_{xz} (MPa)	1167	1259	1219	1103	633
G_{yz} (MPa)	1167	1259	1219	1103	633
ν_{xy}	0.35	0.35	0.35	0.35	0.35
ν_{xz}	0.35	0.35	0.35	0.35	0.35
ν_{yz}	0.35	0.35	0.35	0.35	0.35
σ^0_{AC} (kPa)	780	880	940	740	540
R_x	1.0	1.0	1.0	1.0	1.0
R_y	1.0	1.0	1.0	1.0	1.0
R_z	1.0	1.0	1.0	1.0	1.0
R_{xy}	0.7	0.7	0.7	0.7	0.7
R_{xz}	0.7	0.7	0.7	0.7	0.7
R_{yz}	0.7	0.7	0.7	0.7	0.7

Figures 6.1.1 and 6.1.2 show a comparison of the permanent surface deformation from the finite element models compared to data from the test sections for 1000 load applications. Figures 6.1.3 and 6.1.4 show a comparison of dynamic vertical stress along the load plate centerline for test sections SSS1 and CS2, respectively. Figure 6.1.5 shows the permanent vertical strain towards the bottom of the base at a depth of 160 mm below the pavement surface for test section SSS1 plotted against radius from the load plate centerline for load cycles 1, 10, 100 and 1000. A similar plot is shown in Figure 6.1.6 for permanent vertical strain in the top of the subgrade at a depth of 350 mm below the pavement surface for test section SSS1. Figure 6.1.7 shows the permanent vertical strain versus depth along the load plate centerline for test section CS2.

Figures 6.1.8 – 6.1.11 show the permanent horizontal strain in the bottom of the base and in the top of the subgrade for test sections SSS1 and CS2.

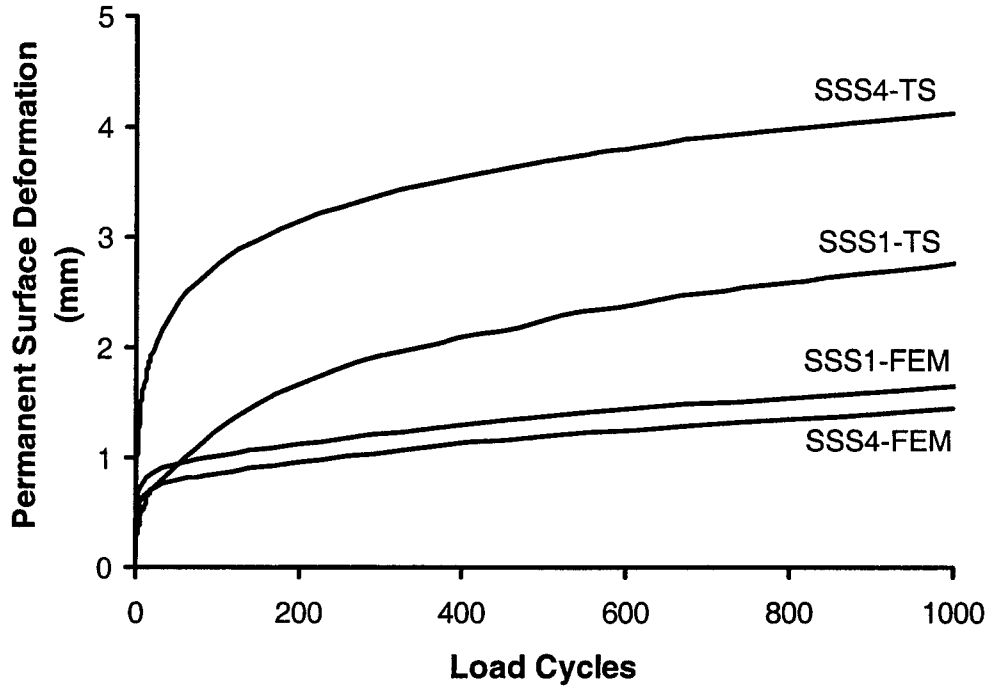

Figure 6.1.1 Permanent surface deformation from FEM and experiments for unreinforced SSS test sections.

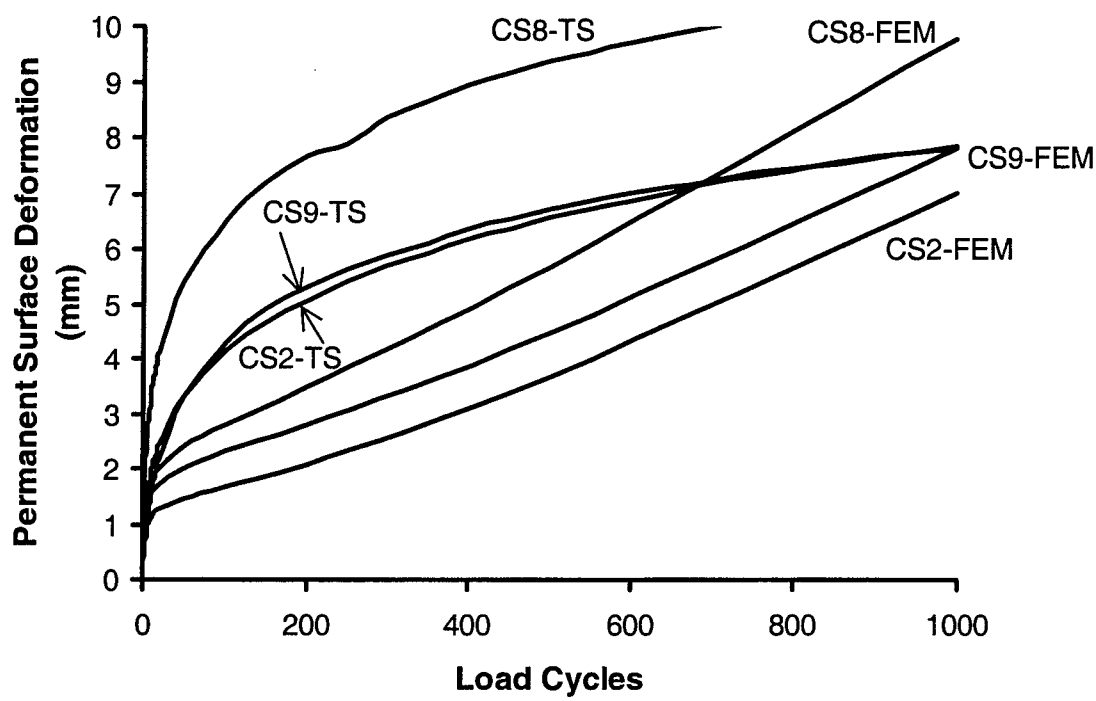

Figure 6.1.2 Permanent surface deformation from FEM and experiments for unreinforced CS test sections.

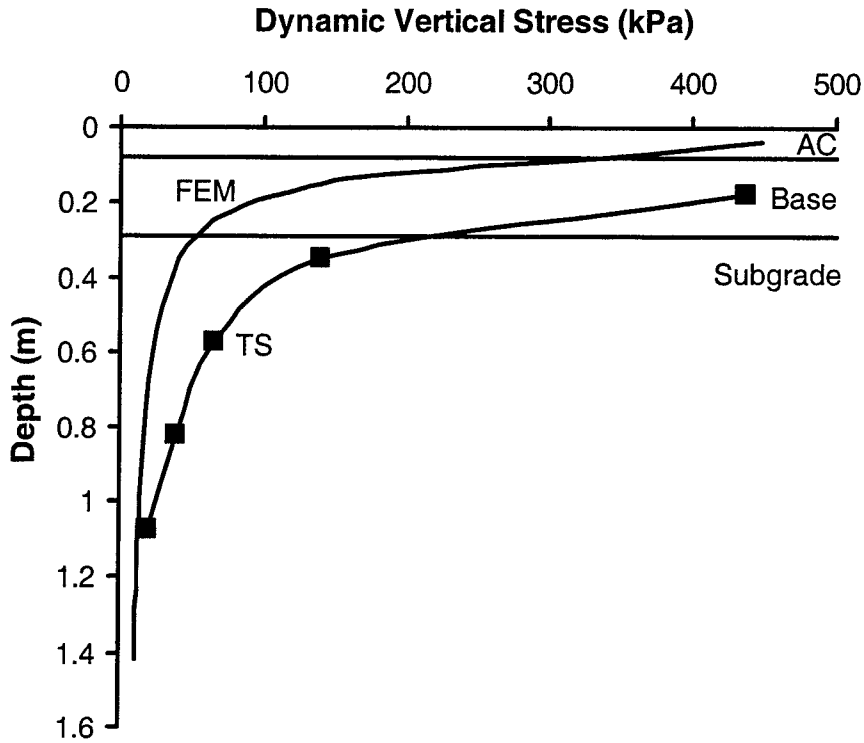

Figure 6.1.3 Dynamic vertical stress versus depth along the load plate centerline for test section SSS1.

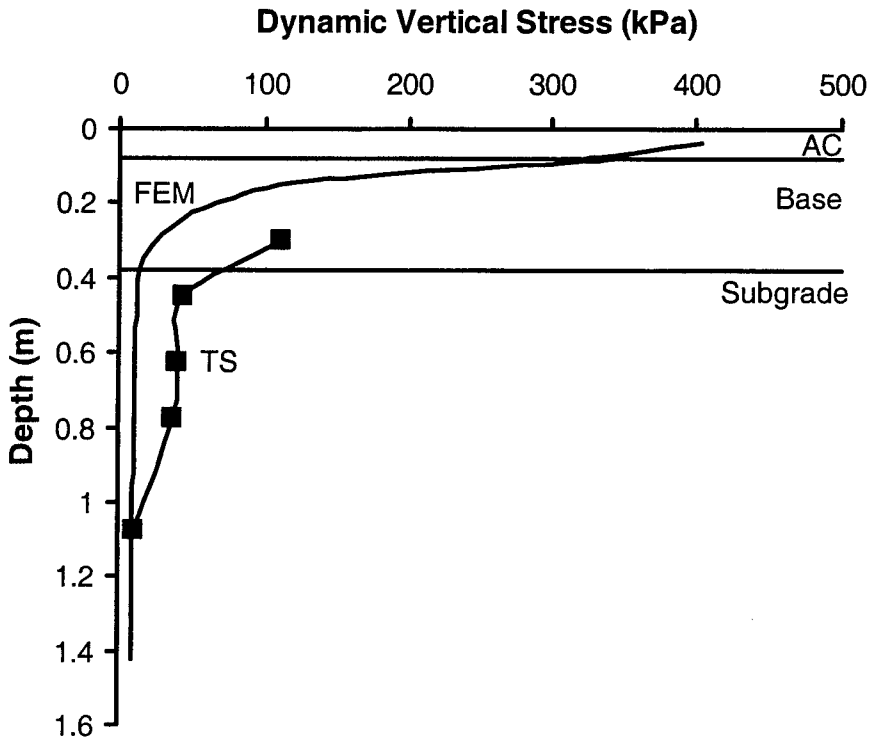

Figure 6.1.4 Dynamic vertical stress versus depth along the load plate centerline for test section CS2.

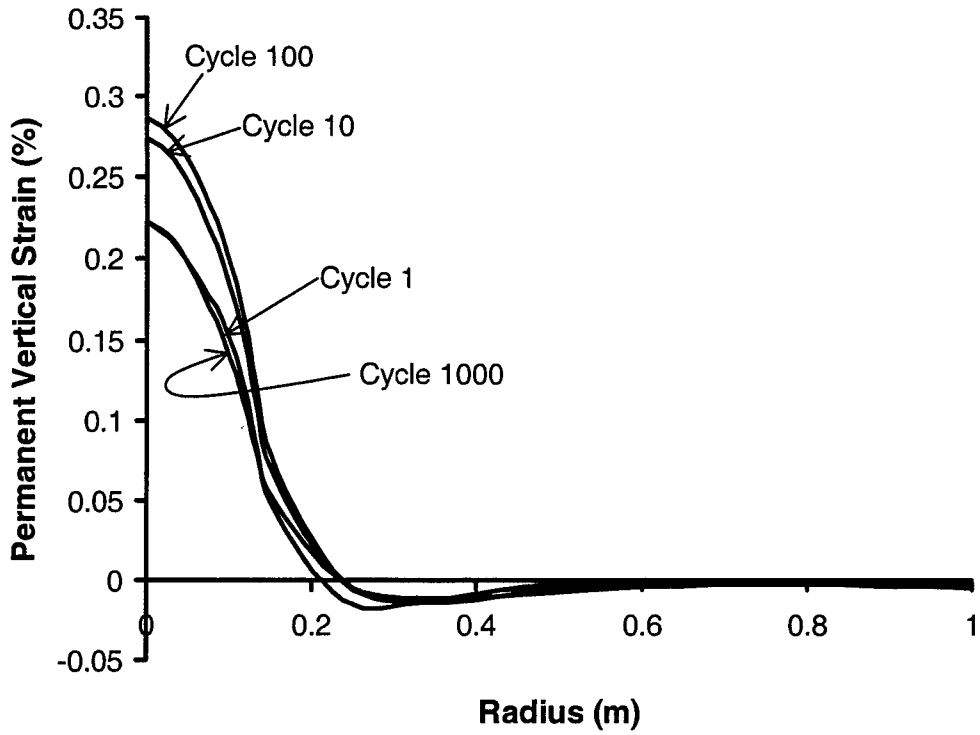

Figure 6.1.5 Permanent vertical strain versus radius in the bottom of the base (z = 160 mm) for test section SSS1.

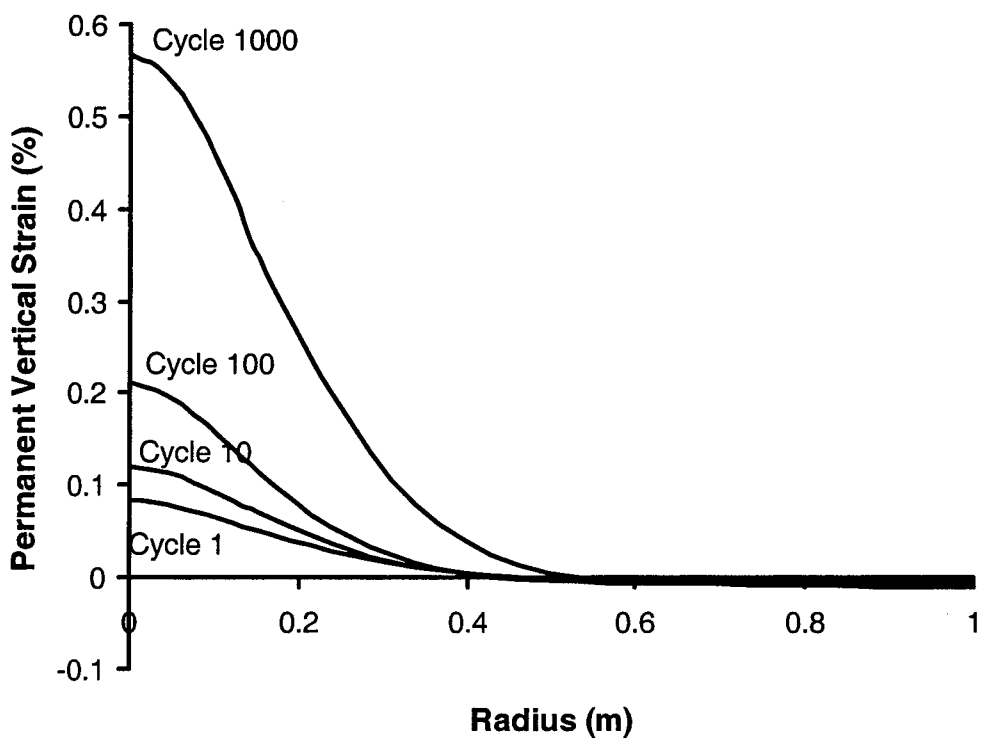

Figure 6.1.6 Permanent vertical strain versus radius in the top of the subgrade (z = 350 mm) for test section SSS1.

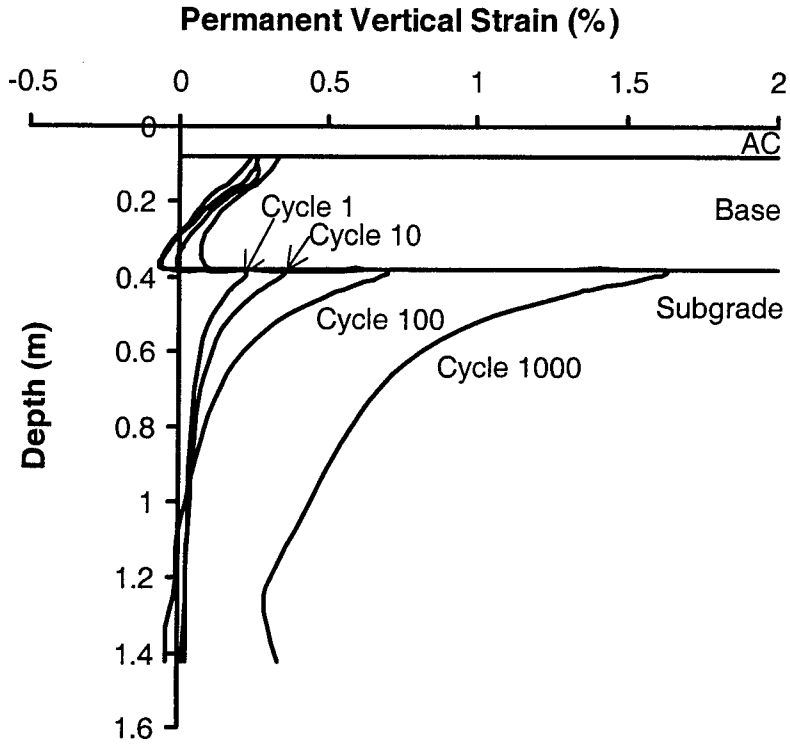

Figure 6.1.7 Permanent vertical strain versus depth along the load plate centerline for test section CS2.

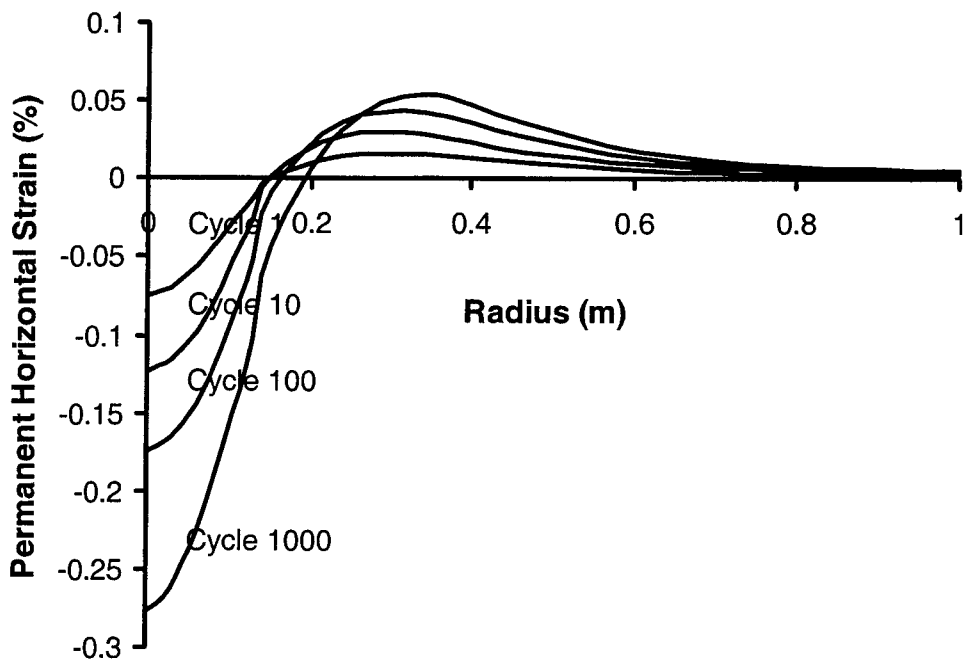

Figure 6.1.8 Permanent horizontal strain in the bottom of the base (z = 215 mm) versus radius for test section SSS1.

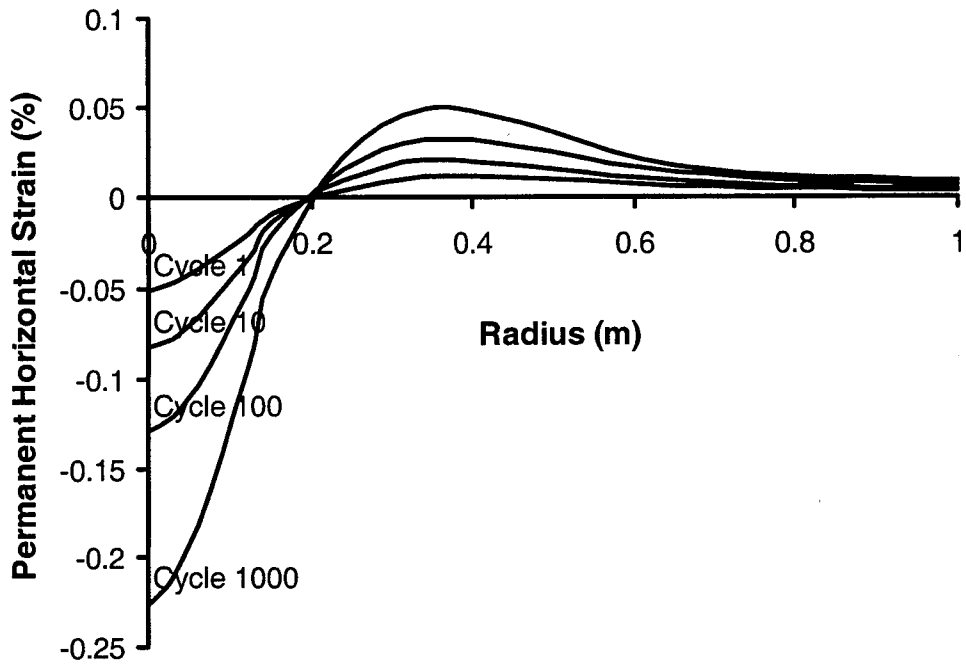

Figure 6.1.9 Permanent horizontal strain in the top of the subgrade (z = 310 mm) versus radius for test section SSS1.

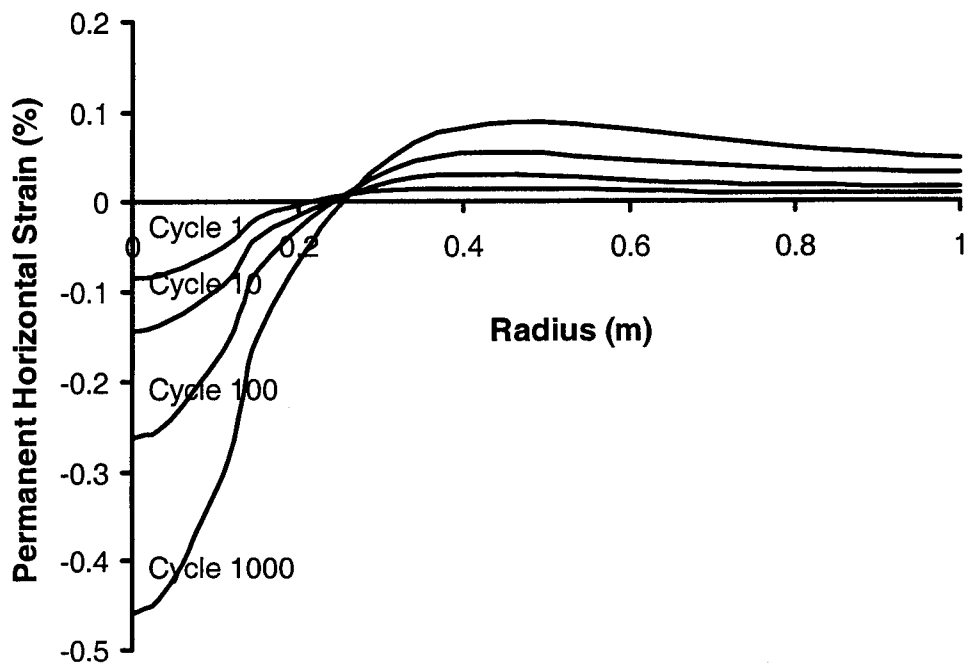

Figure 6.1.10 Permanent horizontal strain in the bottom of the base (z = 325 mm) versus radius for test section CS2.

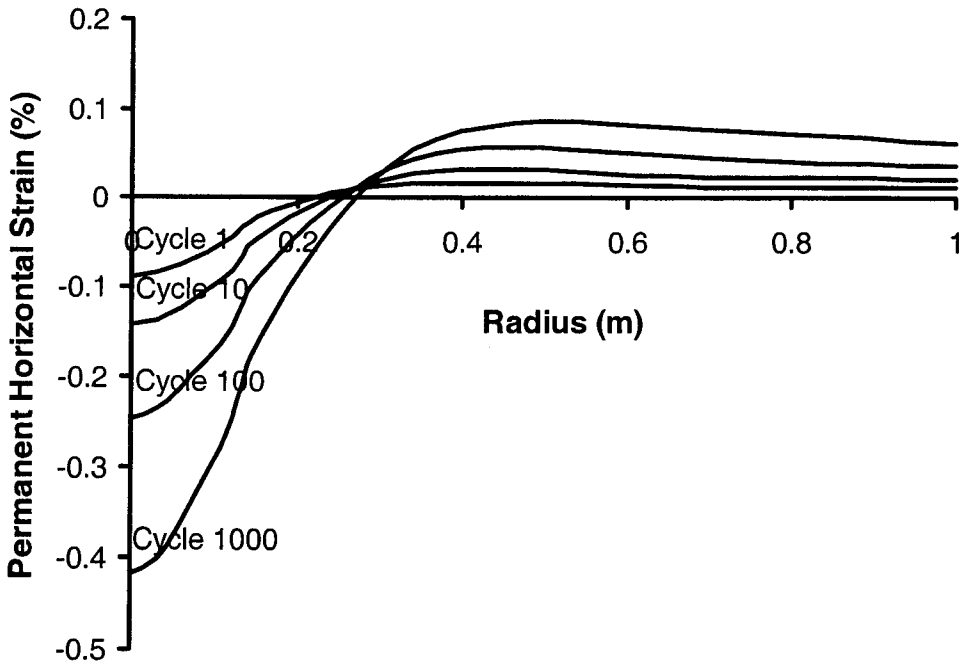

Figure 6.1.11 Permanent horizontal strain in the top of the subgrade (z = 415 mm) versus radius for test section CS2.

The above results show the general ability of the FE model to predict the accumulation of permanent strain in the pavement layer materials and the accumulation of permanent surface deformation under repeated load. The dynamic vertical stresses predicted by the model were generally less than those seen from the measurements made in the test sections. The under prediction of dynamic vertical stress by finite element response models appears to be a common weakness inherent to many programs using continuum-based material models (BRRC, 2000). Permanent vertical strains were generally under predicted in the base aggregate layer and over predicted in the subgrade layer. Permanent horizontal strain in the bottom of the base aggregate and top of the subgrade generally compared well to results from test sections. The observation of extension (negative horizontal strain) beneath the projection of the load plate and compression beyond a radius of 200 to 300 mm was also observed from test section measurements.

The poor agreement of dynamic vertical stress was improved by including additional elements for the stiff steel load plate and compressible rubber pad beneath the load plate and additional anisotropy for the AC layer. In particular, the in-plane elastic moduli and the out-of-plane shear moduli for the asphalt concrete were reduced from the values given in Table 6.1.1 while the other values were kept the same. This caused the asphalt concrete layer to behave less

like a continuous slab and allowed the load to be more localized. Figure 6.1.12 shows results from test section CS2 illustrating how the vertical stress distribution could be improved. The models described above were not rerun for multiple load cycles with these new parameters.

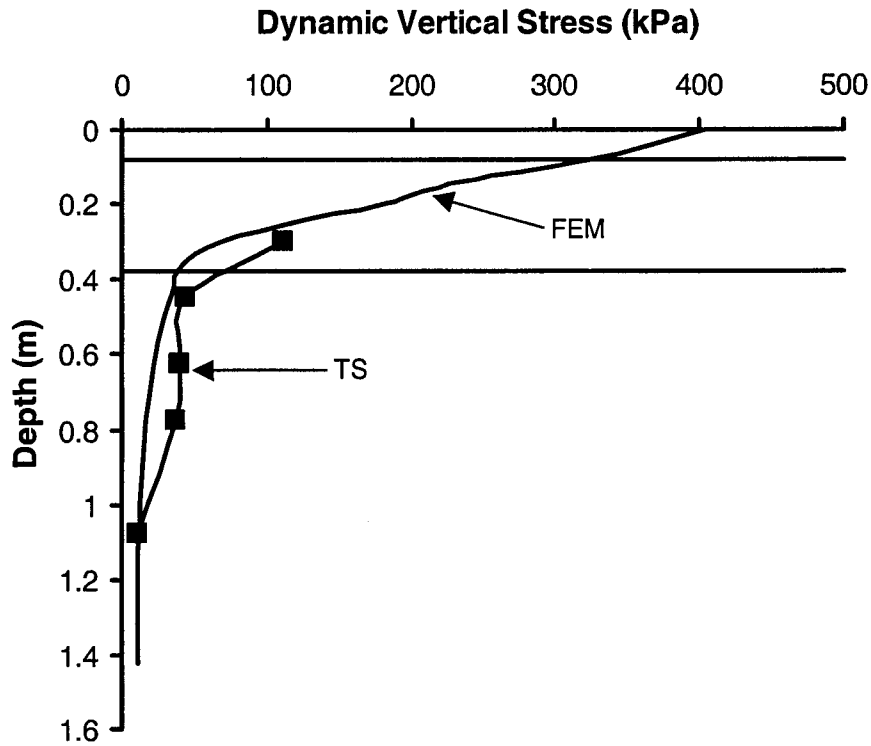

Figure 6.1.12 Dynamic vertical stress versus depth along the load plate centerline for test section CS2 using a revised model.

6.2 Reinforced Pavements

The finite element models described in Sections 5.2 and 5.3 were created to examine the effect of a simulated perfect reinforcement condition and the effect of a geosynthetic material having the properties described in Section 4.3 and 4.4. Three models corresponding to an unreinforced model, a model with perfect reinforcement (as described in Section 5.2) and a model containing geosynthetic reinforcement were created with layer properties similar to those from test section CS2. The models were run for 10 applications of load. The modulus of the geosynthetic was approximately 15 times greater than that which was reported for Geogrid A in Section 4.3.

Figure 6.2.1 illustrates the permanent horizontal strain along a line emerging from the load plate centerline and passing through the bottom of the base aggregate and along the symmetry plane after 10 cycles application of load. As expected, the fixed base case shows no lateral strain as the nodes along the bottom of the base are fixed from motion in the x and y directions. The

reinforcement considerably limits the amount of lateral strain at this depth in the base and corresponds qualitatively to behavior seen in experimental test sections described in Section 3.

Figure 6.2.2 shows the permanent horizontal strain along a vertical line extending through the load plate center and plotted against depth throughout the pavement section after 10 cycles of load. The results show that the effect of restricting lateral motion of the base aggregate at the geosynthetic interface is seen by a reduction of lateral strain further up in the base aggregate and well into the subgrade soil with this effect being most pronounced for the fixed base case.

Figure 6.2.3 shows the mean stress, defined as the average of the three principal stresses, along the same horizontal line in the bottom of the base as used in Figure 6.2.1 and at the point where the peak pavement load was applied for the first load cycle. The results show that a restriction of lateral motion of the base aggregate results in an increase in mean stress, with this effect being most significant for the fixed base case. For these analyses, the increase in modulus of the base for the reinforced case is approximately 1.5 to 3 times that of the unreinforced case at this location. This effect begins to diminish for points higher in the base, as illustrated in Figure 6.2.4 for a position 70 mm above the bottom of the base. In the companion report for this project, the increase in mean stress for a predefined volume of aggregate was as much as 2.5 for comparison unreinforced and fixed base cases.

Figure 6.2.5 shows the vertical stress along the top of the subgrade at peak load for the first load cycle. The effect of confinement and subsequent increase in modulus of the base is to reduce the maximum vertical stress occurring under the load plate. Figure 6.2.6 shows data similar to Figure 6.2.1 showing that the lateral strain in the top of the subgrade is reduced with reinforcement. The effect of these mechanisms is to reduce the permanent vertical strain beneath the load plate centerline and to reduce the amount of permanent surface deformation of the pavement, as illustrated in Figures 6.2.7 and 6.2.8.

Figures 6.2.9 and 6.2.10 show the relative displacement between the interface contact surfaces and the interface shear stress versus lateral distance along the x-axis extending through the contact surface between the base aggregate and the geosynthetic. Results are shown for load cycles 1 and 10 for the point at which the load is a maximum and a minimum for the cycle. Figure 6.2.9 indicates that for this analysis, the value of E_{slip}= 0.1 mm is not exceeded but is being approached for 10 cycles of load application. This figure also shows the ability of relative displacement to accumulate with applied load cycle even though E_{slip} is not exceeded.

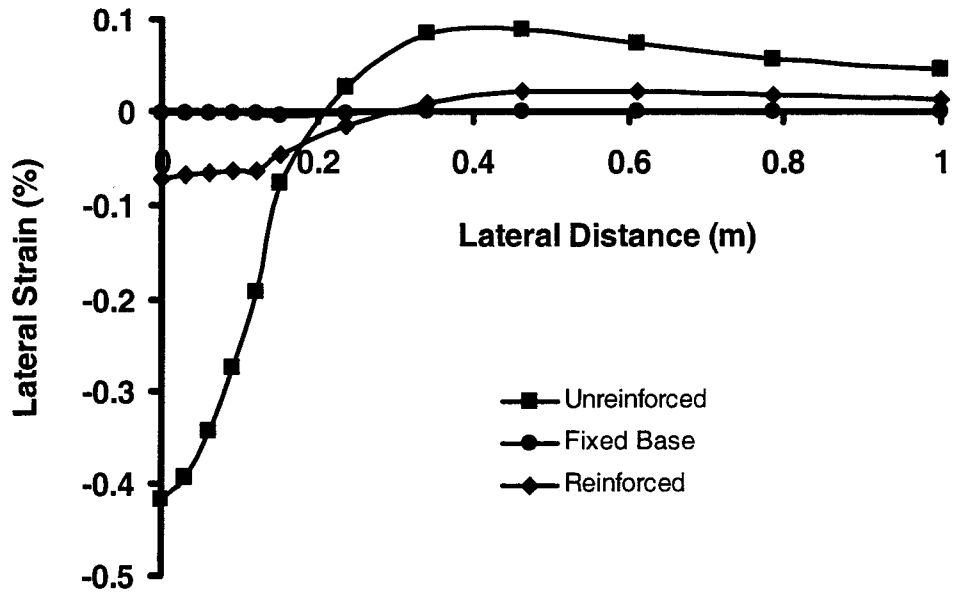

Figure 6.2.1 Lateral permanent strain in the bottom of the base versus lateral distance after 10 cycles of load.

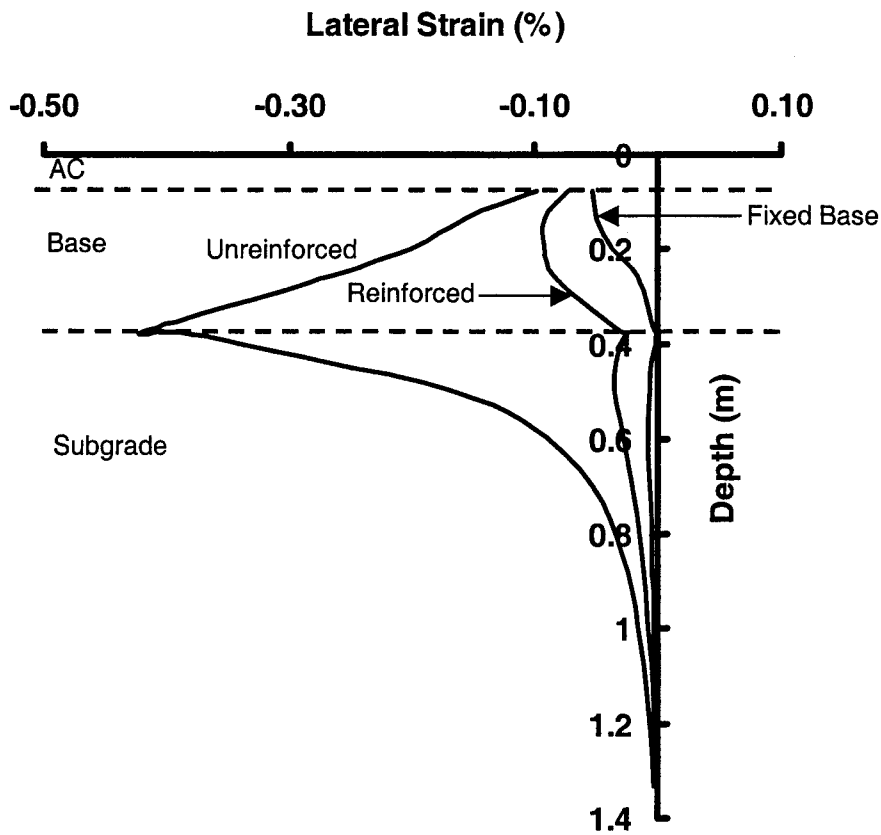

Figure 6.2.2 Lateral permanent strain along the load plate centerline versus depth after 10 cycles of load.

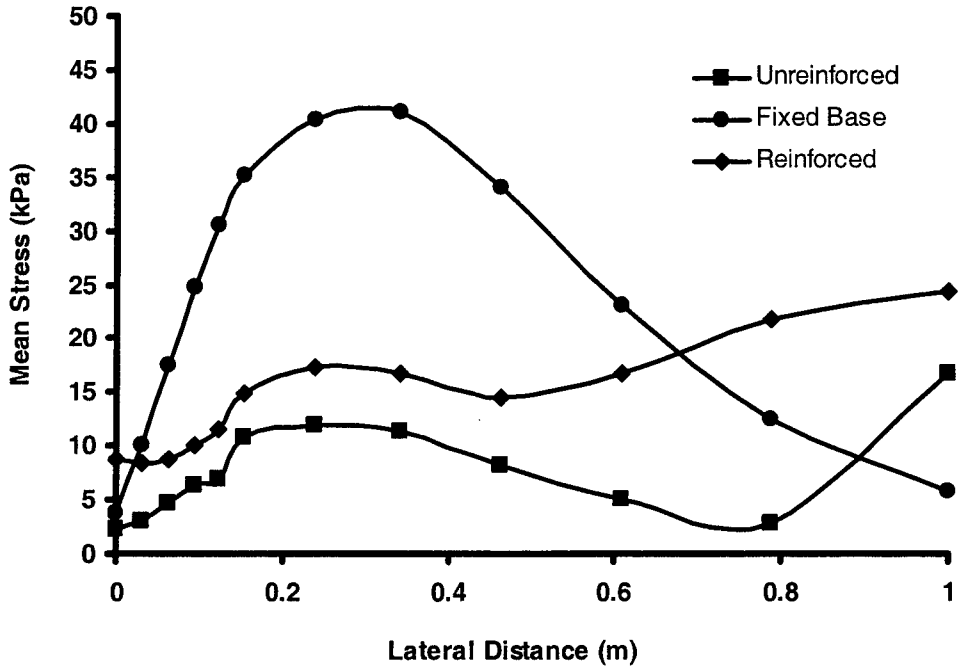

Figure 6.2.3 Mean stress at peak load along the bottom of the base.

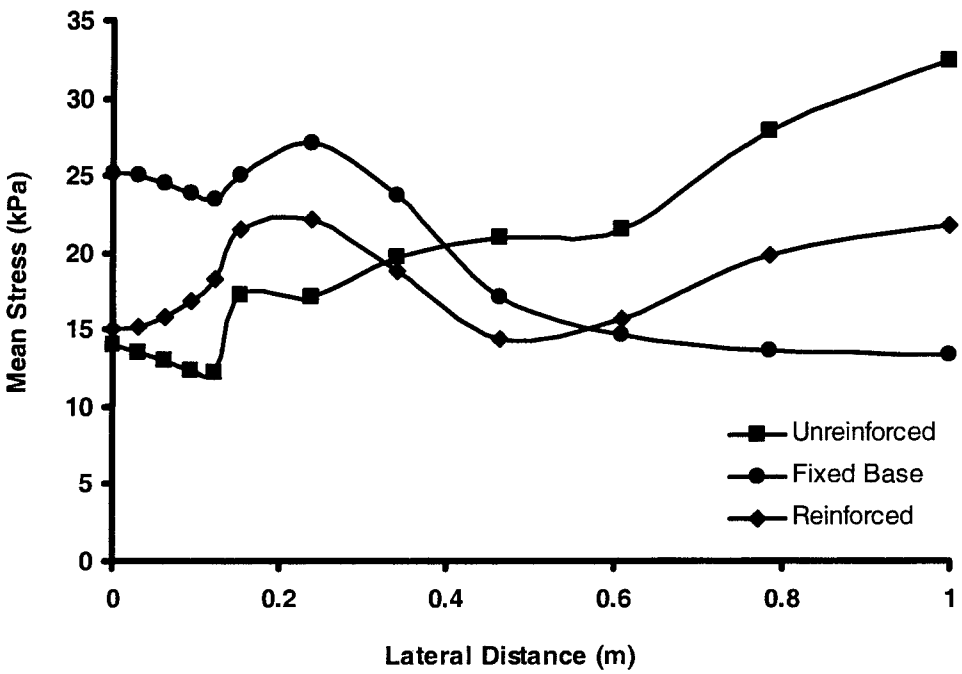

Figure 6.2.4 Mean stress at peak load along a line 70 mm above the bottom of the base.

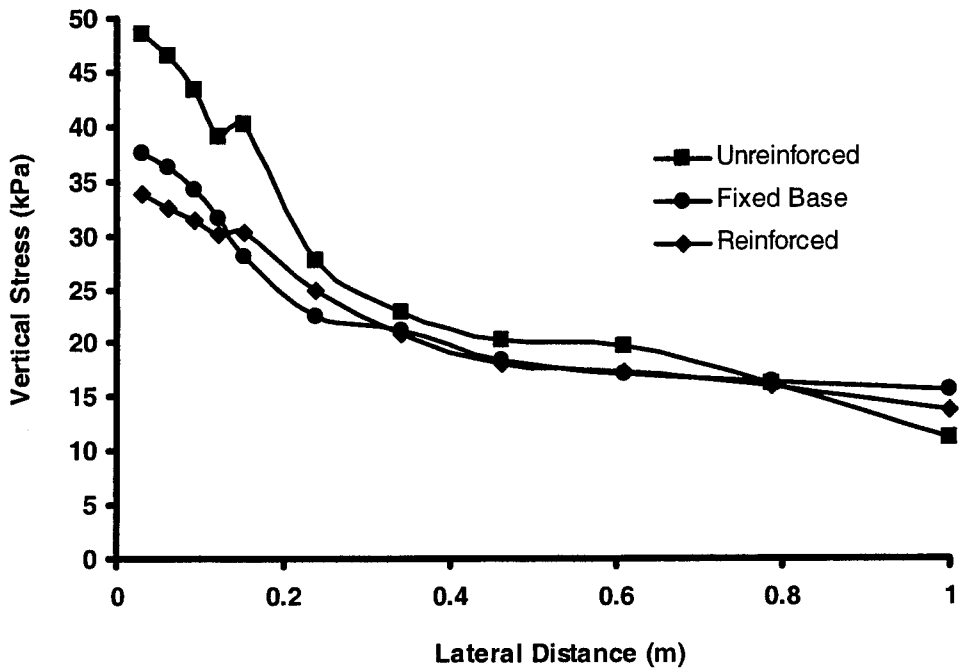

Figure 6.2.5 Vertical stress at peak load in the top of the subgrade.

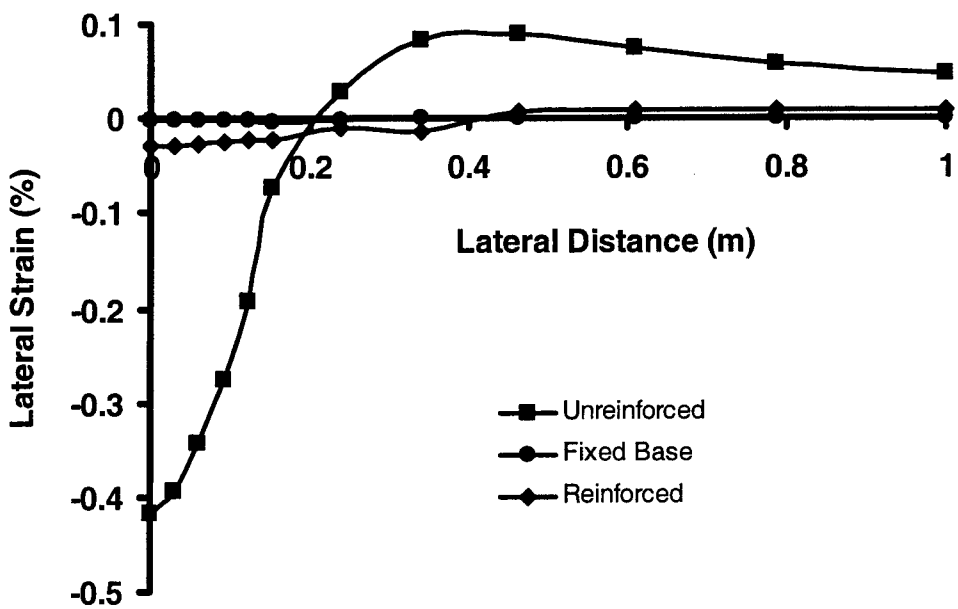

Figure 6.2.6 Lateral permanent strain in the top of the subgrade versus lateral distance after 10 cycles of load.

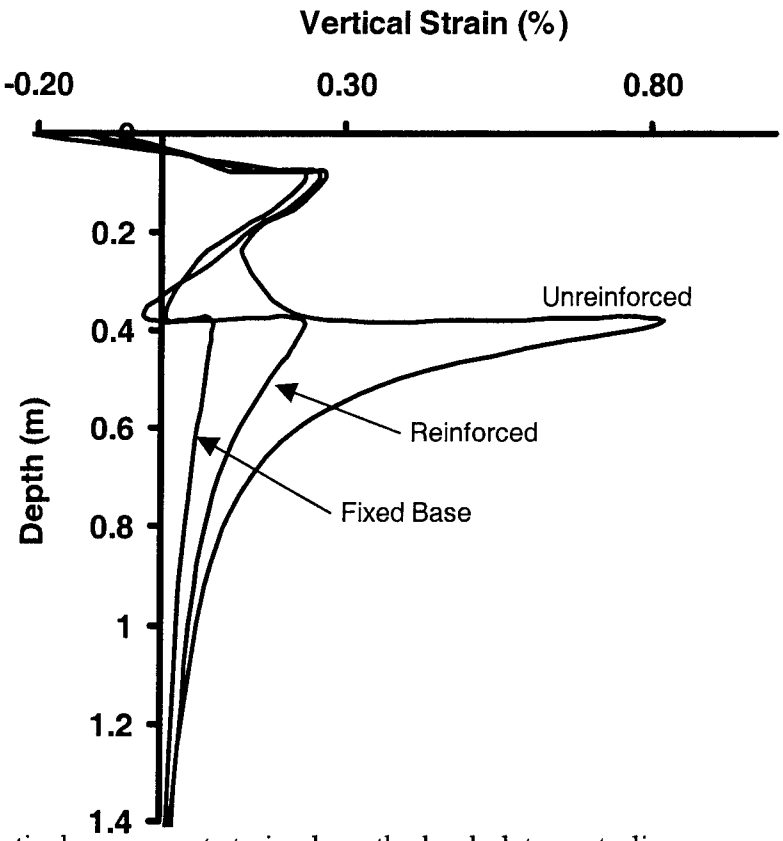

Figure 6.2.7 Vertical permanent strain along the load plate centerline versus depth after 10 cycles of load.

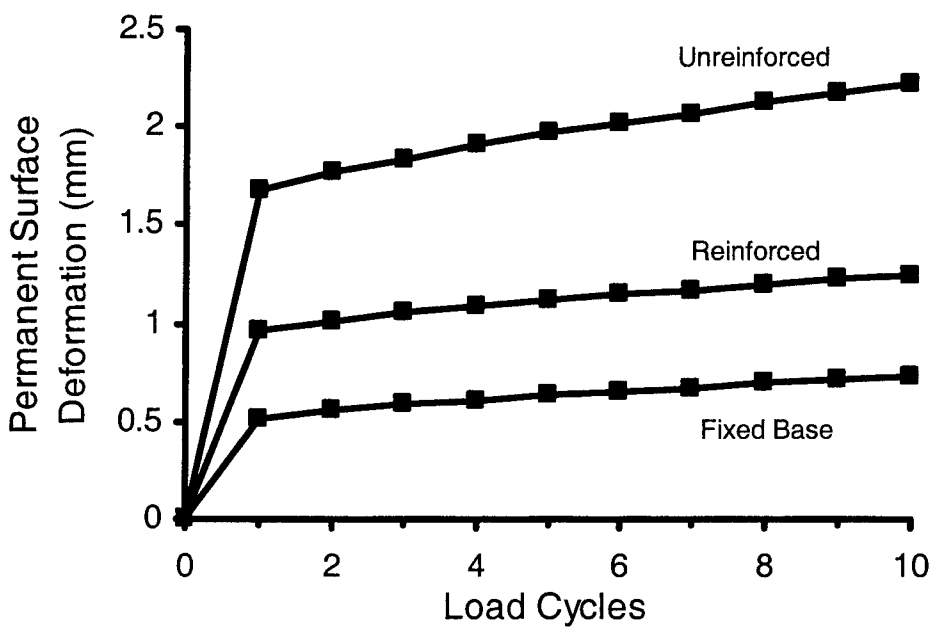

Figure 6.2.8 Permanent surface deformation versus applied load cycles for reinforced sections.

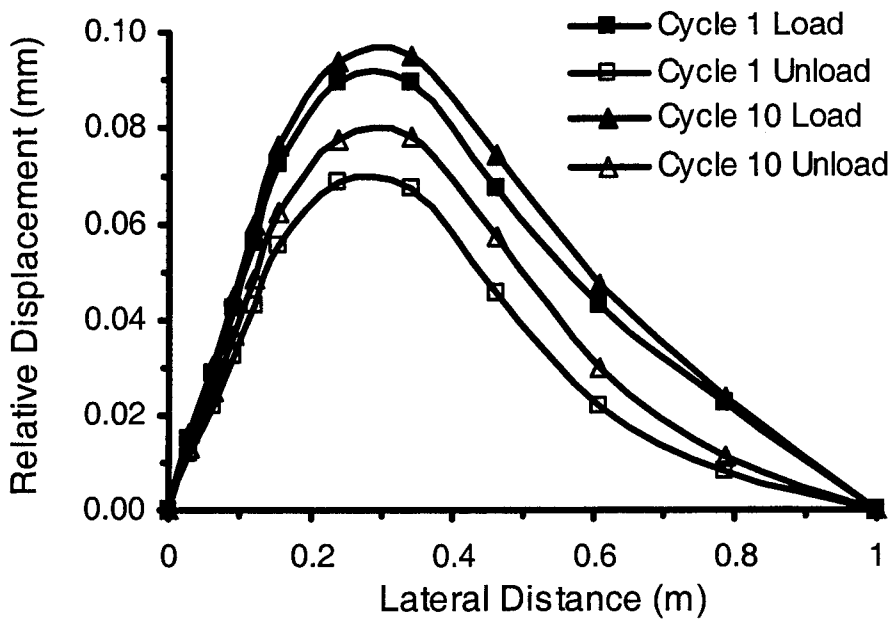

Figure 6.2.9 Relative displacement between the base aggregate and the geosynthetic interface.

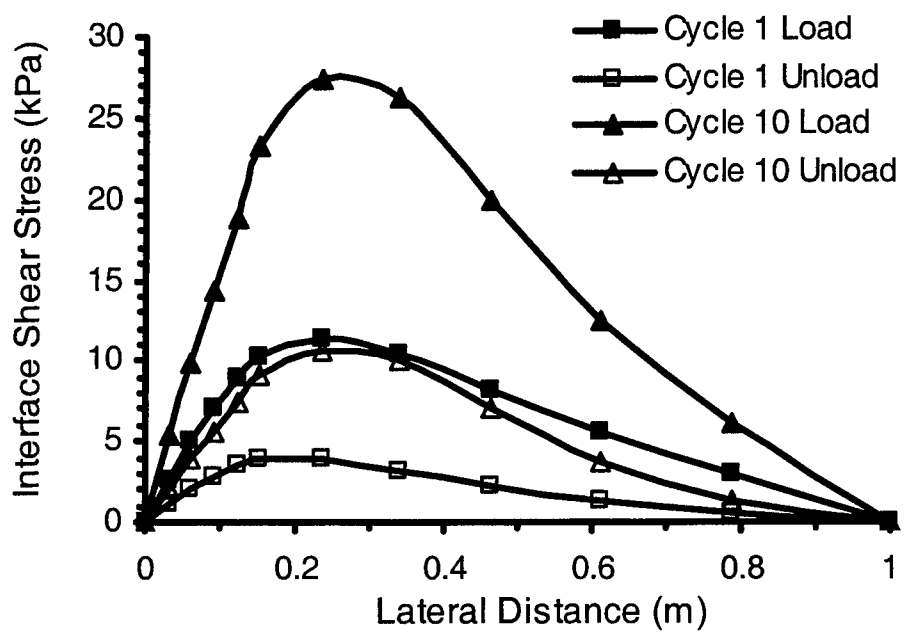

Figure 6.2.10 Interface shear stress between the base aggregate and the geosynthetic.

Several problems were noted with the contact model used to describe interaction between the geosynthetic and the surrounding base aggregate. It would generally be expected that as the value of E_{slip} reduced, the benefit provided by the geosynthetic would increase. This expected relationship was not always observed. Figures 6.2.11 and 6.2.12 show values of permanent vertical strain in the top of the subgrade after one cycle of load and average mean stress in the base aggregate when peak pavement load is applied for the first load cycle. These measures are an indicator of pavement performance. These results are plotted against a modulus multiplier, which is a number by which the calibrated elastic modulus described in Section 4.3 for the geosynthetic materials used was multiplied. Results are plotted for several different values of E_{slip}. The results in Figure 6.2.11 show that the vertical strain on the top of the subgrade increases as E_{slip} decreases, meaning that pavement performance, defined in terms of this response measure, decreases as E_{slip} decreases. The results in Figure 6.2.12 indicate more expected results, showing that mean stress generally increases as E_{slip} decreases, although the results are not completely consistent. Pavement surface deformation was generally seen to increase as E_{slip} decreased, indicating that the negative effect of decreasing E_{slip} on subgrade strain tended to control behavior of the pavement system.

The amount of vertical strain in the top of the subgrade is influenced by the level of shear in the top of the subgrade. As E_{slip} decreases, more tensile load is transferred to the geosynthetic through interface friction, thereby creating more tensile strain in the geosynthetic and hence more shear strain that acts upon the top of the subgrade. Only when the geosynthetic becomes very stiff in tension does this effect begin to diminish. On the other hand, decreasing E_{slip} provides more lateral constraint on the base aggregate and generally provides for increased confinement. These results indicate the complexity of interaction between the various components of the reinforced pavement system. The lack of overall expected benefit as a function of E_{slip} is believed to be due primarily to a material model for the base course aggregate which is not sufficiently sensitive to the effect of mean stress on layer stiffness.

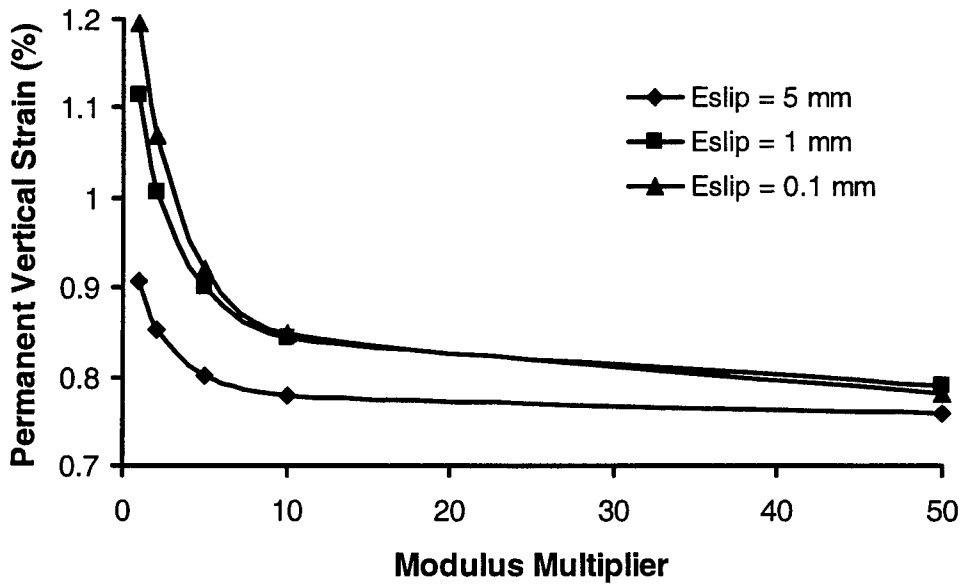

Figure 6.2.11 Permanent vertical strain in the top of the subgrade for various values of geosynthetic modulus and interface elastic slip (E_{slip}).

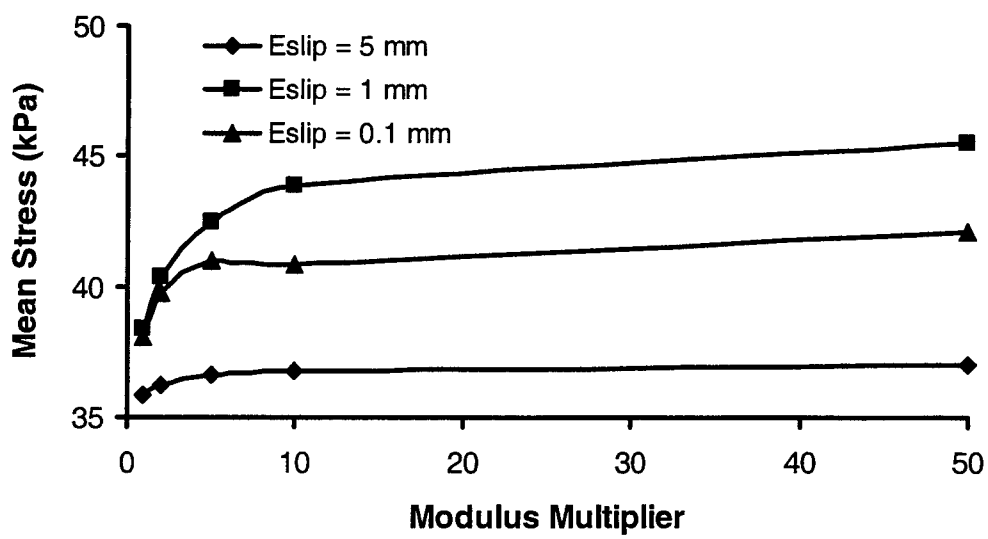

Figure 6.2.12 Average mean stress in the base aggregate for various values of geosynthetic modulus and interface elastic slip (E_{slip}).

The models described above all employed only one contact interface, namely that between the top of the geosynthetic and the bottom of the base aggregate. The nodes of the geosynthetic were equivalenced and therefore connected to the underlying subgrade material. The above results indicate the importance of shear transmitted to the subgrade and suggest that the contact interface between the geosynthetic and the underlying subgrade may need to be specified.

Several models were created where a second contact interface was added for the interface between the geosynthetic and the subgrade. Interface shear strength and stiffness were given relatively low values to model the contact that would be expected between a weak subgrade and the geosynthetic. From these models, anticipated results were not generally observed.

Similar difficulties were encountered for models where the geosynthetic was elevated into the base course aggregate layer. The effect of the geosynthetic on vertical strain throughout the section and on mean stress in the base was not always predictable for these cases. These cases point to improvements required for the base aggregate material model to account for the effects of the reinforcement and for further examination of the contact interface model on system performance.

The reinforcement functions and benefits illustrated in Figures 6.2.1 – 6.2.10 were seen when the geosynthetic modulus for Geogrid A was increased by a factor of 15. When the properties listed in Section 4.3 for Geogrid A were used directly in the model, negligible reinforcement benefit was observed. In the companion report (Perkins 2001) for this project, a factor of 4.4 was applied to the geosynthetic tensile modulus (as determined from ASTM D 4595 at 2 % strain) to match reinforcement benefit seen from comparison test sections. The general observation of the need to increase the measured geosynthetic modulus in order to derive expected benefits points to deficiencies in the numerical model used and may suggest that traditional measurement techniques for geosynthetic tensile properties may be inappropriate for this application. For instance, the rate of loading in a roadway application may be as great as 40 times that employed in the ASTM D 4595 test method, which may account for an effectively higher modulus in the application. Normal stress confinement by overlying roadway materials and vehicle loading may also cause an effectively higher modulus in some geosynthetic materials.

7.0 CONCLUSIONS

The material modeling and finite element modeling work described in this report allows the following conclusions to be made:

1. An elastic-perfectly plastic material model for the asphalt concrete layer was necessary to allow this pavement layer to permanently deform with the underlying base layer and to prevent artificial tensile loads from being applied to the base layer when pavement load

was returned to zero. The use of isotropic material properties for the AC layer resulted in an underprediction of vertical dynamic stress under the load plate centerline. The introduction of direction dependency of elastic and plastic properties (material anisotropy) allowed the pavement load to be more localized and produced improved predictions of vertical stress beneath the load plate centerline and an improved deflected shape of the AC surface.

2. A bounding surface plasticity model was used for the base aggregate and subgrade layers. The model showed elastic-plastic behavior with isotropic hardening. The bounding surface concept allowed for permanent strains to be predicted under repeated pavement loading. Comparison of permanent strain in the aggregate and subgrade layers from test section results to FEM predictions showed the general ability of the model to describe the accumulation of permanent strain under repeated load. The model was well suited for the subgrade material while improvements are needed for modeling the base aggregate layer. In particular, the small level of tensile strength predicted for the aggregate layer and the apparent lack of sensitivity of material stiffness on mean stress confinement created limitations in its use to describe the effects of geosynthetic reinforcement.
3. A material model for the geosynthetic was formulated to include components of elasticity, plasticity, creep and direction dependency. The model provides reasonable predictions of various types of in-air tensile tests.
4. A relatively simple Coulomb friction model was used to describe interaction between the geosynthetic and the base aggregate layer. The model provides reasonable predictions of pull out response as compared to test conducted using the base aggregate and geosynthetics used in the test sections available to the project.
5. Finite element models of reinforced pavements were capable of qualitatively showing mechanisms of reinforcement previously observed from instrumented test sections. In particular, the reinforced models showed a reduction of lateral strain at the bottom of the base, an increase in mean stress confinement for a zone of aggregate adjacent to the geosynthetic, an improved vertical stress distribution on the subgrade, and a reduction of shear in the top of the subgrade. In order to see appreciable effects from the reinforcement, the elastic modulus of the material needed to be increased by approximately an order of magnitude. This may be due to the manner in which elastic modulus is determined from

common tension tests but is more likely due to deficiencies in the material model used for the base course aggregate.

6. While providing reasonable predictions of pull out behavior, the interface contact model produced several unexpected results in the finite element models of reinforced pavements that require further examination. In particular, increasing the shear modulus of the interface appeared to increase the amount of shear transmitted to the subgrade and hence increased the vertical strain in the top of the subgrade. For the models examined, the strain in the subgrade tended to control the overall deformation behavior of the pavement. This result may also be due to a material model for the base aggregate that is not sufficiently sensitive to effects of confinement caused by the geosynthetic.
7. The complexity of the models and the necessity to run the models for many load cycles caused excessively long run times and limited the amount of cases that could be examined. Future work in this area will require more computationally efficient models and projection methods that can be used to project stress and strain measures forward over steps of load cycles prior to running a new load step.

8.0 REFERENCES

Abramento, M. and Whittle, A.J. (1995), "Analysis of Pullout Tests for Planar Reinforcements in Soil", *Journal of Geotechnical Engineering*, Vol. 121, No. 6, pp. 476-485.

Alobaidi, I.M., Hoare, D.J. and Ghataora, G.S. (1997), "Load Transfer Mechanism in Pullout Tests", *Geosynthetics International*, Vol. 4, No. 5, pp. 509-521.

AMOCO (1996). Personal Fax Communication, 6-12-1996.

AMOCO (2001). Personal Email Communication, 4-23-2001.

Ashmawy, A.K. & Bourdeau, P.L. (1996), "Response of a Woven and a Nonwoven Geotextile to Monotonic and Cyclic Simple Tension", *Geosynthetics International*, Vol. 3, No. 4, pp. 493-515.

ASTM (1995), *Proposed Standard Test Method for Measuring Geosynthetic Pull-out Resistance in Soil*, Draft No. 6, ASTM, Philadelphia, PA, USA.

Barksdale, R.D., Brown, S.F. and Chan, F. (1989), "*Potential Benefits of Geosynthetics in Flexible Pavement Systems*", National Cooperative Highway Research Program Report No. 315, Transportation Research Board, National Research Council, Washington DC.

Bathurst, R.J. and Cai, Z. (1994), "In-Isolation Cyclic Load-Extension Behavior of Two Geogrids", *Geosynthetics International*, Vol. 1, No. 1, pp. 1-19.

Berg R.R., Christopher, B.R. and Perkins, S.W. (2000), *Geosynthetic Reinforcement of the Aggregate Base Course of Flexible Pavement Structures, GMA White Paper II*, Geosynthetic Materials Association, 130p.

Bergado, D.T. and Chai, J.-C. (1994), "Pullout Force/Displacement Relationship of Extensible Grid Reinforcements", *Geotextiles and Geomembranes*, Vol. 13, No. 5, pp. 295-316.

Bonaquist, R. and Witczak, M.W. (1996), "Plasticity Modeling Applied to the Permanent Deformation Response of Granular Materials in Flexible Pavement Systems", In *Transportation Research Record 1540*, TRB, National Research Council, Washington, DC, USA, pp. 7-14.

Bonczkiewicz, C., Christopher, B.R. and Atmatzidis, D.K. (1988), "Evaluation of Soil-Reinforcement Interaction by Large-Scale Pull-Out Tests", *Transportation Research Record 1188*, TRB, National Research Council, Washington, DC, USA, pp. 1-18.

BRRC (2000), *AMADEUS, Advanced Models for Analytical Design of European Pavement Structures*, Report RO-97-SC.2137, Belgian Road Research Center.

Burd, H.J. and Brocklehurst, C.J. (1992), "Parametric Studies of a Soil Reinforcement Problem Using Finite Element Analysis", *Proceedings of the Conference on Computer Methods and Advances in Geomechanics*, Balkema, pp. 1783-1788.

Burd, H.J. and Brocklehurst, C.J. (1990), "Finite Element Studies of the Mechanics of Reinforced Unpaved Roads", *Proceedings of the 4th International Conference on Geotextiles, Geomembranes and Related Products*, The Hauge, Netherlands, pp. 217-221.

Burd, H.J. and Houlsby, G.T. (1986), "A Large Strain Finite Element Formulation for One Dimensional Membrane Elements", *Computers and Geotechnics*, Vol. 2, pp. 3-22.

Chen, D.-H., Zaman, M., Laguros, J. and Soltani, A. (1995), "Assessment of Computer Programs for Analysis of Flexible Pavement Structure", In *Transportation Research Record 1482*, TRB, National Research Council, Washington, DC, USA, pp. 123-133.

Dafalias, Y.F. and Hermann, L.R. (1986), "Bounding Surface Plasticity. II: Application to Isotropic Cohesive Soils", *Journal of Engineering Mechanics*, ASCE, Vol. 112, No. 12, pp. 1263-1291.

Dafalias, Y.F. and Hermann, L.R. (1982), "Bounding Surface Formulation of Soil Plasticity", *Soil Mechanics-Transient and Cyclic Loads*, Chapter 10, John Wiley and Sons, Ltd., pp. 253-282.

Dafalias, Y.F. (1975), *On Cyclic and Anisotropic Plasticity*, Ph.D. Thesis, University of California at Berkeley.

Desai, C.S., Rigby, D.B. and Samavedam, G. (1993), "Unified Constitutive Model for Airport Pavements", *Proceedings of the Conference Airport Pavement Innovations – Theory to Practice*, Vicksburg, MS, pp. 46-60.

Desai, C.S., Somasundaram, S. and Frantziskonis, G.N. (1986), "A Hierarchical Approach for Constitutive Modeling of Geologic Materials", *International Journal of Numerical Methods in Geomechanics*, Vol. 10, pp.25-257.

Dondi, G. (1994), "Three-Dimensional Finite Element Analysis of a Reinforced Paved Road", *Proceedings of the Fifth International Conference on Geotextiles, Geomembranes and Related Products*, Singapore, pp. 95-100.

Farrag, K. (1991), *Pull-Out Testing Facility For Geosynthetics*, Louisiana Transportation Research Center, Project No. 87-1GT, 225 p.

Giroud, J.P., Darrasse, J. and Bachus, R.C. (1993), "Hyperbolic Expression for Soil-Geosynthetic or Geosynthetic-Geosynthetic Interface Shear Strength", *Geotextiles and Geomembranes*, Vol. 12, No. 3, pp. 275-286.

Gourc, J.P., Delmas, P. and Giroud, J.P. (1980), "Experiments on Soil Reinforcement with Geotextiles", Presented at the *ASCE National Convention*, Portland, OR, USA.

Gurung, N. and Iwao, Y. (1999), "Comparative Model Study of Geosynthetic Pull-Out Response", *Geosynthetics International*, Vol. 6, No. 1, pp. 53-68.

Hibbitt, Karlson and Sorensen (1998), *ABAQUS Standard User's Manuals*, Version 5.8, Pawtucket, RI, USA.

IFAI (1994), *1995 Specifier's Guide*, Geotechnical Fabrics Report, Vol. 12, No. 9, pg. 169.

Ingold, T.S. (1983), "Laboratory Pull-Out Testing of Grid Reinforcements in Sand", *Geotechnical Testing Journal*, Vol. 6, No. 3, pp. 101-111.

Jewell, R.A. (1990), "Reinforcement Bond Capacity", *Géotechnique*, Vol. 40, No. 3, pp. 513-518.

Jewell, R.A., Milligan, G.W.F., Sarsby, R.W. and Dubois, D. (1984), "Interaction Between Soil and Geogrids", *Symposium on Polymer Grid Reinforcement*, Thomas Telford, London, UK, ppl. 18-30.

Juran, I. and Chen, C.L. (1988), "Soil-Geotextile Pull-Out Interaction Properties: Testing and Interpretation", *Transportation Research Record 1188*, TRB, National Research Council, Washington, D.C., USA, pp. 37-47.

Kaliakin, V.N., Dafalias, Y.F. and Hermann, L.R. (1987), *Time Dependent Bounding Surface Model for Isotropic Cohesive Soils*, notes for a short course held in conjunction with the Second International Conference on Constitutive Laws for Engineering Materials, Tucson, AZ, January.

Karpurapu, R. & Bathurst, R.J. (1995), "Behaviour of Geosynthetic Reinforced Soil Retaining Walls Using the Finite Element Method", *Computers and Geotechnics*, Vol. 17, No. 3, pp. 27-299.

Kirkner, D.J., Shen, W., Hammons, M.I. and Smith, D.M. (1996), "Numerical Simulation of Permanent Deformation in Flexible Pavement Systems Subjected to Moving Wheel Loads", *Proceedings of the 11th Conference on Engineering Mechanics*, ASCE, Ft. Lauderdale, FL, pp. 430-433.

Kirkner, D.J., Caulfield, P.N. and McCann, D.M. (1994), "Three-Dimensional, Finite Element Simulation of Permanent Deformations in Flexible Pavement Systems", In *Transportation Research Record 1448*, TRB, National Research Council, Washington, DC, USA, pp. 34-39.

Koerner, R.M., Wayne, M.H. and Carroll, R.G. (1989), "Analytic Behavior of Geogrid Anchorage", *Proceedings of the Conference Geosynthetics '89*, San Diego, CA, USA, pp. 525-536.

Leshchinsky, D., Dechasakulsom, M., Kaliakin, V.N. & Ling, H.I. (1997), "Creep and Stress Relaxation of Geogrids", *Geosynthetics International*, Vol. 4, No. 5, pp. 463-479.

Ling, H.I., Mohri, Y. & Kawabata, T. (1998), "Tensile Properties of Geogrids Under Cyclic Loadings", *Journal of Geotechnical and Geoenvironmental Engineering*, Vol. 124, No. 8, pp. 782-787.

Lubliner, J. (1990), *Plasticity Theory*, Macmillan Publishing Company, New York, 495 p.

Madhav, M.R., Gurung, N. and Iwao, Y. (1998), "A Theoretical Model for the Pull-Out Response of Geosynthetic Reinforcement", *Geosynthetics International*, Vol. 5, No. 4, pp. 399-424.

McGown, A., Andrawes, K.Z. & Kabir, M.H. (1982), "Load-Extension Testing of Geotextiles Confined In-Soil", *Proceedings of the Second International Conference on Geotextiles*, Las Vegas, NV, USA, Vol. 3, pp. 793-798.

McGown, A. (1978), "The Properties of Nonwoven Fabrics Presently Identified as Being Important in Public Works Applications", *Proceedings of the Congress INDEX 78*, European Disposables and Nonwovens Association, pp. 1.1.1-1.3.1.

McVay, M. and Taesiri, Y. (1985), "Cyclic Behavior of Pavement Base Materials", *Journal of Geotechnical Engineering*, ASCE, Vol. 111, No. 1, pp. 1-17.

Miura, N., Sakai, A., Taesiri, Y., Yamanouchi, T. and Yasuhara, K. (1990), "Polymer Grid Reinforced Pavement on Soft Clay Grounds", *Geotextiles and Geomembranes*, Vol. 9, pp. 99-123.

Moraci, N. and Montanelli, F. (1997), "Behavior of Geogrids Under Cyclic Loads", *Proceedings of the Conference Geosynthetics '97*, Long Beach, CA, USA, pp. 961-976.

Ochiai, H., Otani, J., Hayashic, S. and Hirai, T. (1996), "The Pull-Out Resistance of Geogrids in Reinforced Soil", *Geotextiles and Geomembranes*, Vol. 14, pp. 19-42.

Perkins, S.W. (2001), *Mechanistic-Empirical Modeling and Design Model Development of Geosynthetic Reinforced Flexible Pavements: Final Report*, Montana Department of Transportation, Helena, Montana, Report No. FHWA/MT-01/002/99160-1A, 156p.

Perkins, S.W. (1999a), *Geosynthetic Reinforcement of Flexible Pavements: Laboratory Based Pavement Test Sections*, Montana Department of Transportation, Helena, Montana, Report No. FHWA/MT-99/8106-1, 140 p.

Perkins, S.W. (1999b), "Mechanical Response of Geosynthetic-Reinforced Flexible Pavements", *Geosynthetics International*, Vol. 6, No. 5, pp. 347-382.

Perkins, S.W., Ismeik M. and Fogelsong, M.L (1999), "Influence of Geosynthetic Placement Position on the Performance of Reinforced Flexible Pavement Systems", *Proceedings of the Conference Geosynthetics'99*, Boston, MA, USA, V. 1, pp. 253-264.

Perkins, S.W. and Cuelho, E.V. (1999), "Soil-Geosynthetic Interface Strength and Stiffness Relationships From Pull Out Tests", *Geosynthetics International*, Vol. 6, No. 5, pp. 321-346.

Perkins, S.W., Ismeik, M., Fogelsong, M.L., Wang, Y. and Cuelho, E.V. (1998a), "Geosynthetic-Reinforced Pavements: Overview and Preliminary Results", *Proceedings of the Sixth International Conference on Geosynthetics*, Atlanta, GA, USA, Vol. 2, pp. 951-958.

Perkins, S.W., Ismeik, M. and Fogelsong, M.L. (1998b), "Mechanical Response of a Geosynthetic-Reinforced Pavement System to Cyclic Loading", *Fifth International Conference on the Bearing Capacity of Roads and Airfields*, Trondheim, Norway, Vol. 3, pp. 1503-1512.

Perkins, S.W. and Ismeik, M. (1997), "A Synthesis and Evaluation of Geosynthetic Reinforced Base Course Layers in Flexible Pavements: Part I", *Geosynthetics International*, Vol. 4, No. 6, pp. 549-604, 1997.

Prevost, J.H. (1978), "Plasticity Theory for Soil Stress-Strain Behavior" *ASCE Journal of the Engineering Mechanics Division*, Vol. 104, No. 5, pp. 1177-1194.

Ramsamooj, D.V. and Piper, R. (1992), "Theoretical Prediction of Rutting in Flexible Pavement Subgrades", *Canadian Geotechnical Journal*, Vol. 29, pp. 765-778.

Rollings, R., Smith, D.M. and Peters, J. (1998), "Advanced Analytical Modeling for Military Pavements", *Proceedings of the First National Symposium on 3D Finite Element Modeling for Pavement Analysis and Design*, Charleston, WVA, pp. 142-159.

Schofield, A.N. and Wroth, C.P. (1968), *Critical State Soil Mechanics*, McGraw-Hill, Inc., London.

Sobhi, S. and Wu, J.T.H. (1996), "An Interface Pullout Formula for Extensible Sheet Reinforcement", *Geosynthetics International*, Vol. 3, No. 5, pp. 565-582.

Tensar (2001), Personal fax communication, 4-23-2001, 37 p.

Wathugala, G.W., Huang, B. and Pal, S. (1996), "Numerical Simulation of Geosynthetic Reinforced Flexible Pavement", In *Transportation Research Record 1534*, TRB, National Research Council, Washington, DC, USA, pp. 58-65.

Wathugala, G.W. and Desai, C.S. (1993), "Constitutive Model for Cyclic Behavior of Clay I: Theory", *Journal of Geotechnical Engineering*, ASCE, Vol. 119, No. 4, pp.714-729.

White, T.D., Zaghloul, S.M., Anderton, G.L. and Smith, D.M. (1998), "Pavement Analysis for Moving Aircraft Load", *Journal of Transportation Engineering*, Vol. 123, No. 6, pp. 436-446.

Wilson-Fahmy, R.F. and Koerner, R.M. (1993), "Finite Element Modelling of Soil-Geogrid Interaction with Application to the Behavior of Geogrids in a Pullout Loading Condition", *Geotextiles and Geomembranes*, Vol. 12, No. 5, pp. 479-501.

Wu, J.T.H. and Helwany, M.B. (1987), *Numerical Simulation of Soil-Geotextile Interface in Pullout Test*, Geosynthetic Research Report 87-03, Department of Civil Engineering, University of Colorado-Denver, CO, USA, 120 p.

Yogarajah, I. And Yeo, K.C. (1994), "Finite Element Modeling of Pull-Out Tests with Load and Strain Measurements", *Geotextiles and Geomembranes*, Vol. 13, pp. 43-54.

Yogendrakumar, M. & Bathurst, R.J. (1992), "Numerical Simulation of Reinforced Soil Structures During Blast Loads", *Transportation Research Record 1336*, TRB, National Research Council, Washington, DC, USA pp. 1-8.

Yuan, Z. and Chua, K.M. (1991), "Analytical Model for Pullout of Soil Reinforcement", *Transportation Research Record 1330*, TRB, National Research Council, Washington, DC pp. 64-71.

Zaghloul, S. and White, T.D. (1993), "Use of a Three-Dimensional, Dynamic Finite Element Program for Analysis of Flexible Pavement", In *Transportation Research Record 1388*, TRB, National Research Council, Washington, DC, USA, pp. 60-69.

APPENDIX A: Notation

Provided below is a list of symbols and their definitions. Given the fact that certain symbols have been used more than once for different material definitions, the notation list below is broken down by various categories. Duplicate definitions for the same symbol was necessary to avoid confusion with symbols used in original references.

General

BCR	Base course reduction ratio (%)
CBR	California bearing ratio (%)
TBR	Traffic benefit ratio (unitless)

Asphalt Concrete Material Model

E_x	Elastic modulus in the x direction (MPa)
E_y	Elastic modulus in the y direction (MPa)
E_z	Elastic modulus in the z direction (MPa)
G_{xy}	Shear modulus in the x – y plane (MPa)
G_{xz}	Shear modulus in the x – z plane (MPa)
G_{yz}	Shear modulus in the y – z plane (MPa)
R_x	Yield stress ratio for the x direction (unit less)
R_y	Yield stress ratio for the y direction (unit less)
R_z	Yield stress ratio for the z direction (unit less)
R_{xy}	Yield stress ratio for the x – y plane (unit less)
R_{xz}	Yield stress ratio for the x – z plane (unit less)
R_{yz}	Yield stress ratio for the y – z plane (unit less)
ν_{xy}, ν_{yx}	Poisson's ratio in the x – y plane (unitless)
ν_{xz}, ν_{zx}	Poisson's ratio in the x – z plane (unitless)
ν_{yz}, ν_{zy}	Poisson's ratio in the y – z plane (unitless)
σ^0_{AC}	Ultimate yield stress (kPa)

Base Aggregate and Subgrade Bounding Surface Material Model

A	Shape parameter (unitless)
C	Projection center parameter (unitless)
C_c	Compression index (unitless)
C_s	Swelling/recompression index (unitless)
E	Elastic modulus (kPa)
e_{in}	Initial void ratio (unitless)
G	Shear modulus (kPa)
h	Hardening parameter (unitless)
I	First stress invariant (kPa)
I_L	Atmospheric pressure (kPa)
I_o	Size of ellipse 1 of the bounding surface (kPa)
J	Square root of the second deviatoric stress invariant (kPa)
m	Hardening parameter (unitless)
M	Slope of critical state line in p-q stress space (unitless)
N	Slope of critical state line in I-J stress space (unitless)
R	Shape parameter (unitless)
s_p	Elastic zone parameter (unitless)
T	Shape parameter (unitless)
α	Lode angle (degrees)
κ	Swell/recompression slope (unitless)
λ	Virgin compression slope (unitless)
ν	Poisson's ratio (unitless)
ϕ	Drained soil friction angle in triaxial compression (degrees)

Geosynthetic Material Model

A	Creep material parameter (unit less)
E_m	Elastic modulus in the machine direction (kPa)
E_n	Elastic modulus in the direction through the thickness of the material (kPa)
E_{xm}	Elastic modulus in the cross-machine direction (kPa)
$G_{m\text{-}n}$	Shear modulus in the machine – normal to the geosynthetic plane (kPa)
$G_{xm\text{-}m}$	Shear modulus in the cross-machine - machine plane (kPa)
$G_{xm\text{-}n}$	Shear modulus in the cross-machine – normal to the plane direction (kPa)
m	Creep material parameter (unit less)
n	Creep material parameter (unit less)
N	Number of geogrid ribs contained across the width of a sample
R_m	Yield and creep stress ratio for the machine direction (unit less)
R_n	Yield and creep stress ratio for the normal to the plane direction (unit less)
R_{xm}	Yield and creep stress ratio for the cross-machine direction (unit less)
$R_{m\text{-}n}$	Yield stress ratio for the machine – normal to the geosynthetic plane (unit less)
$R_{xm\text{-}m}$	Yield and creep stress ratio for the cross-machine – machine plane (unit less)
$R_{xm\text{-}n}$	Yield and creep stress ratio for the cross-machine – normal to the geosynthetic plane (unit less)
W_c	Current width of a geosynthetic sample loaded in uniaxial tension (m)
W_i	Initial width of a geosynthetic sample (m)
W_m	Physically measured width of a geogrid sample from rib to rib (m)
$\gamma_{m\text{-}n}$	Shear strain in the machine – normal to the geosynthetic plane
$\gamma_{xm\text{-}m}$	Shear strain in the cross-machine - machine plane
$\gamma_{xm\text{-}n}$	Shear strain in the cross-machine – normal to the plane direction
ε_l	Lateral strain across the width of a geosynthetic sample
ε_m	Normal strain in the machine direction
ε_n	Normal strain in the direction through the thickness of the material
ε_{xm}	Normal strain in the cross-machine direction
$\bar{\varepsilon}$	Uniaxial strain on a sample oriented 45° with respect to its principal directions
$\underline{\varepsilon}$	Lateral strain on a sample oriented 45° with respect to its principal directions

ε^{cr}	Creep strain
$\dot{\varepsilon}^{cr}$	Creep strain rate
$\nu_{m\text{-}n}$, $\nu_{n\text{-}m}$	Poisson's ratio in the machine – normal to the geosynthetic plane
$\nu_{m\text{-}xm}$, $\nu_{xm\text{-}m}$	Poisson's ratio in the machine – cross-machine plane
$\nu_{n\text{-}xm}$, $\nu_{xm\text{-}n}$	Poisson's ratio in the cross-machine – normal to the geosynthetic plane
σ_m	Normal stress in the machine direction (kPa)
σ_n	Normal stress in the direction through the thickness of the material (kPa)
σ_{xm}	Normal stress in the cross-machine direction (kPa)
$\bar{\sigma}$	Uniaxial stress on a sample oriented 45° with respect to its principal directions (kPa)
σ^o	Reference yield stress describing yield in the cross-machine direction (kPa)
$\tau_{m\text{-}n}$	Shear stress in the machine – normal to the geosynthetic planet (kPa)
$\tau_{xm\text{-}m}$	Shear stress in the cross-machine - machine plane (kPa)
$\tau_{xm\text{-}n}$	Shear stress in the cross-machine – normal to the plane direction (kPa)

Geosynthetic/Aggregate Interaction Simplified Numerical Model

G_i	Initial interface shear modulus (kN/m^3)
u	Interface shear displacement (m)
σ_n	Interface normal stress (kPa)
τ	Interface shear stress (kPa)
ψ_p	Peak interface friction angle (degrees)
ψ_r	Residual interface friction angle (degrees)

Geosynthetic/Aggregate Interaction Model (GAIM)

E_{slip}	Elastic slip (m)
Δ	Interface shear displacement (m)
σ	Interface normal stress (kPa)
τ	Interface shear stress (kPa)
μ	Interface friction coefficient (unitless)